IMAGE RECONSTRUCTION ALGORITHMS FOR OPTICAL TOMOGRAPHY

IMAGE RECONSTRUCTION ALGORITHMS FOR OPTICAL TOMOGRAPHY

Proefschrift

ter verkrijging van de graad van doctor
aan de Technische Universiteit Delft,
op gezag van de Rector Magnificus Prof. dr. ir. T. H. J. J. van der Hagen,
voorzitter van het College voor Promoties,
in het openbaar te verdedigen op
vrijdag 21 december 2018 om 10:00 uur

door

Anna Katharina TRULL

Master of Science in Computational Life Science

Universität zu Lübeck, Duitsland
geboren te Itzehoe, Duitsland.

Dit proefschrift is goedgekeurd door de promotoren.

Samenstelling promotiecommissie bestaat uit:

Rector Magnificus,   voorzitter
Prof. dr. ir. L. J. van Vliet   Technische Universiteit Delft, promotor
Dr. ir. J. Kalkman   Technische Universiteit Delft, copromotor

Onafhankelijke leden:
Prof. dr. ir. F. J. Verbeek   Universiteit Leiden
Dr. ir. M. C. Goorden   Technische Universiteit Delft
Prof. dr. K. J. Batenburg   Universiteit Leiden & CWI Amsterdam
Prof. dr. B. Rieger   Technische Universiteit Delft
Dr. N. Bhattacharya   Technische Universiteit Delft
Prof. dr. I. T. Young   Technische Universiteit Delft, reservelid

To my parents
Anja and Michael Trull

Contents

Chapter 1

Introduction

1.1. Looking inside biological objects

A detailed understanding of biological systems cannot only be obtained by visual inspection from the outside. In many cases a detailed image also has to be made from the inside. To look inside of biological objects, such as small animals, organs, or cells, various tomographic imaging techniques have been developed that are based on waves, either electromagnetic or acoustic, that interact with the tissue. The word tomography comes from the Greek words *tomos* which means slice or section and *graphō* to write or to draw and hence, tomography refers to the process of imaging slices of the object.

Common tomographic imaging techniques are magnetic resonance imaging (MRI), ultrasound (US), (micro) computed X-ray tomography (CT) and optical coherence tomography (OCT). MRI is an imaging technique that uses radio frequency waves to image protons in tissue based on their nuclear spin. Tomographic images are made by applying a spatially dependent gradient to the main magnetic field and applying a radio frequency pulse to excite a single slice. MRI images tissue with various types of contrast depending on the surrounding of the protons. Pre-clinical MRI, also called magnetic resonance microscopy (MRM), focuses on imaging of mice and other small animals [1]. However, to achieve sufficient resolution and signal-to-noise ratio in MRM, specimen fixation is required. MRM can achieve spatial resolution in the order of 100 μm. Another imaging modality is US, which uses ultrasonic waves and is based on the measurement of the acoustic echo time to obtain depth information. In US a slice of the sample is imaged by creating a sequence of pulses in a plane. In pre-clinical research US can provide anatomical information, such as tumor volume in cancer research, with a spatial resolution of 100 μm [2]. As an example, an US image of a mouse embryo is shown in Fig. 1.1 (a). In X-ray computed tomography the structure of the object is determined by measuring projections of the transmitted X-ray intensity through the object. X-ray CT is relatively fast and a commonly used method, because of its large contrast between bone (hard material) and tissue (soft material). In pre-clinical research X-ray CT is called micro CT and specially aimed at small animal imaging at a resolution of about 5 μm. Micro CT

bone anatomy and density or angiography by using contrast agents for studying vascular structures [6]. As an example, a micro CT image of a mouse embryo is shown in Fig. 1.1 (b). OPT is the optical equivalent of CT as it uses light transmission to image the object. Figure 1.1 (c) shows an optical projection tomography (OPT) image of a zebrafish. The typical resolution of OPT is 5 to 10 μm. More information about OPT is given in Section 1.3.
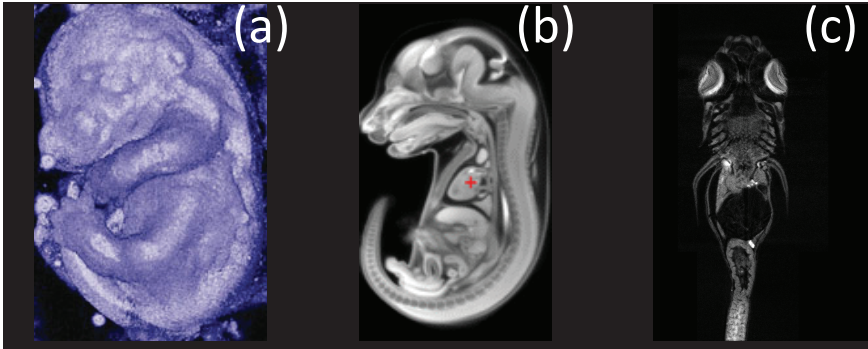
Figure 1.1: Tomographic images of (a) a mouse embryo with ultrasound [3], (b) a mouse embryo with micro CT [4] and (c) a zebrafish measured with (transmission) optical projection tomography [5].

Due to the absence of ionizing radiation, high tissue contrast, high resolution and its cost efficiency, optical tomographic imaging techniques are becoming more popular. In optical tomography, photons are launched onto and through tissue where they interact with the tissue components. From the transmitted or emitted photons an image of the object is constructed. A highly successful optical tomographic technique is OCT, which is an interferometric imaging technique that measures the optical reflection of tissue with an imaging depth of $1-3$ mm. Time gating and the use of a focusing lens are used to filter out non-scattered light. This technique is most commonly used for retinal imaging [7, 8], but has many other biomedical applications, such as in cardiovascular imaging [9]. Another optical imaging technique is optical projection tomography (OPT). OPT is a high resolution imaging technique in which the sample is optically cleared to reduce the scattering strength of the tissue. It has a resolution of 5 to 10 μm and an imaging depth of $2-3$ mm. OPT is mainly used in developmental biology [10]. Diffuse optical tomography (DOT) [11] is an imaging technique based on scattered light for the image construction with a resulting loss of spatial resolution. A common application is to monitor regional variations of the hemoglobin, but it can also be applied to deep-tissue applications such as breast cancer detection [12, 13].

1.2. Computed tomography

Techniques where the image of a slice is reconstructed from a set of projections of an object created from transmitted or emitted radiation are known as computed tomography. A schematic illustration of the principle of computed tomography for a parallel beam transmission geometry is shown in Fig. 1.2 (a). Transmission measurements are performed at multiple lateral locations that together comprise a projection of the transmission through the object at a single angle. These projections are acquired at multiple angles around the object. The value measured at every point in the projection is described mathematically by an integral over the object.

After the projections have been acquired, a reconstruction algorithm is ap-
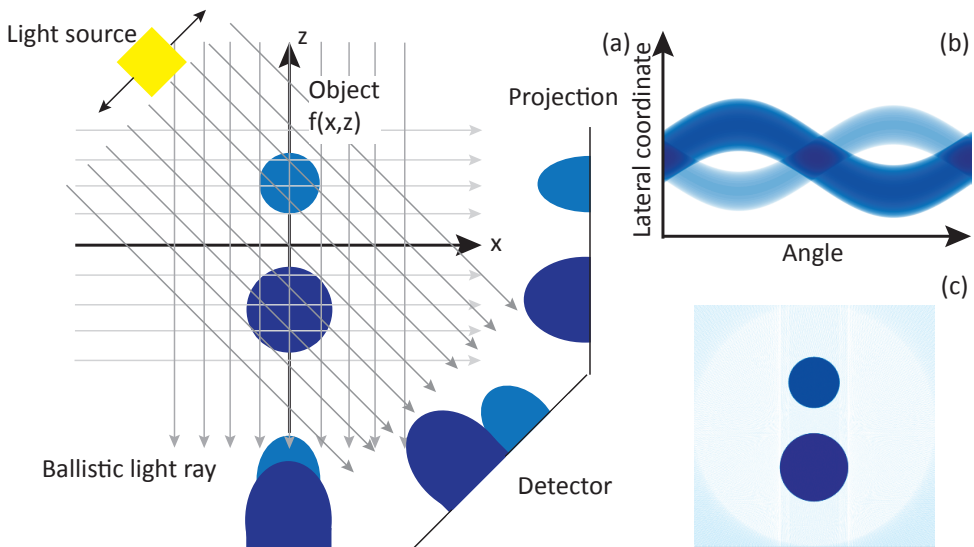
Figure 1.2: Schematic Illustration of the basic principle of computed tomography. (a) Parallel beam geometry for three different angles and the resulting projections at the detector. The unknown object is $f(x,z)$. (b) Visualization of the projections in a sinogram. (c) Reconstruction of the object from the projections using filtered back projection.

plied to compute a solution to the inverse problem, i.e., finding the object that is the best match with the measurements given the measurement geometry. Depending on the type of interaction of the radiation with the object different parameters, for example the intensity or phase of the transmitted or emitted radiation, can be reconstructed. In the most simple case of a straight ray beam going in parallel geometry through an object the forward projection (from the object to the measurement) is mathematically defined as the Radon transform of the

object [14] given by

$$p(s,\theta) = \iint\limits_{-\infty}^{\infty} f(x,z)\delta(x\cos\theta + z\sin\theta - s)\,\mathrm{d}x\,\mathrm{d}z, \qquad (1.1)$$

where f denotes the object, s the lateral shift, and θ the rotation angle. The result of the forward projection $p(s,\theta)$ is commonly visualized in a sinogram, which is an image with the lateral detector coordinate on the vertical axis, the projection angle on the horizontal axis, and with the intensity of the sinogram as a measure of the value of the line integral, see Fig. 1.2 (b). In the ideal case of infinitely many parallel narrow rays acquired over infinitely many angles the object can be perfectly reconstructed with filtered back projection, an example of which is shown in Fig. 1.2 (c). The filtered back projection reconstruction is defined as

$$f(x,z) = \int\limits_{0}^{\pi}\int\limits_{-\infty}^{\infty} P_\theta(f_s)\exp(i2\pi f_s s)|f_s|\,\mathrm{d}f_s\,\mathrm{d}\theta, \qquad (1.2)$$

where $P_\theta(f_s)$ is the 1D Fourier transform $p(s,\theta)$.

Computed tomography has only become possible since the advent of digital imaging and computer processing. Nowadays, projections are acquired using a pixelated digital camera at a discrete number of angles. Since the continuous signal is sampled and the system is discrete, the filtered back projection reconstruction of Eq. 1.2 can be approximated by a discrete sum where each ray in the projection has an influence on pixels in the image traversed by the ray. The entire inverse problem can be described as smearing back the information of every individual projection back onto the image of the object. A schematic illustration of the discrete description of the forward problem for this case is shown in Fig. 1.3 (left). The blue arrows indicate rays that cross different object pixels, labeled f_1 to f_4. The length of the crossing defines the amount in which every
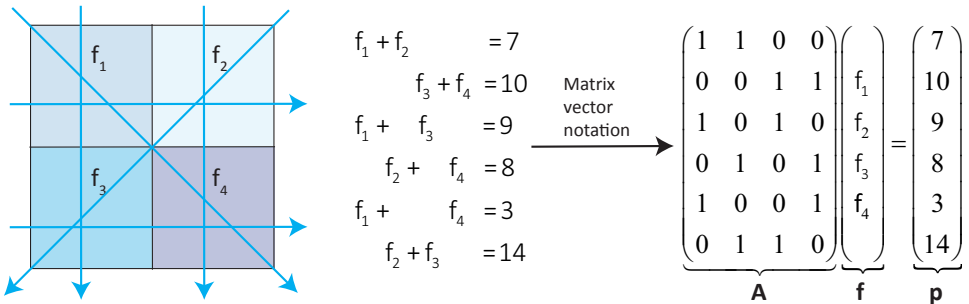

Figure 1.3: Schematic illustration of the forward projection in matrix vector notation.

pixel has influence on the projection **p**, Fig. 1.3. The relation between the object
f and the projection **p** can be written in the form of a set of linear equations as
shown in Fig. 1.3 (center), which can be written as a matrix equation, see Fig. 1.3
(right). The influence of the object **f** on all detector pixels **p** is determined by
the geometry of the system and described by the matrix, **A**. This set of equations
written as a vector-matrix-multiplication describes the discrete forward projec-
tion as **Af** = **p**. The backward projection is then given by direct matrix inversion
as **f** = **A**$^{-1}$**p**, where **A**$^{-1}$ is the inverse of the geometry matrix if **A** has the same
number of rows and columns. If the number or rows is larger than the number
of columns, the Moore-Penrose inverse, $(\mathbf{A}^T\mathbf{A})^{-1}\mathbf{A}^T$ is used to approximate the
inverse.

In general, an inverse problem can be formulated as was done by Hadamard
as [15]: Find for the projections **p** the image **f**, such that **Af** = **p**. The given math-
ematical problem is well-posed if and only if:

1. The system of equations **Af** = **p** has a solution for every **p**. This ensures the
   existence of the solution.

2. The solution is unique, i.e, there is only one solution for every set of mea-
   surements.

3. The inverse system geometry **A**$^{-1}$ is continuous, which means the solution
   f is continuously dependent on the data **p**.

If one of the criteria above is not valid for the inverse problem, it is called ill-
posed.

Besides a discrete form of filtered backprojection, various iterative image re-
construction techniques are available for tomographic image reconstruction. A
method to solve a large system of linear equations is known as the algebraic re-
construction technique (ART) also known as Kacmarz method). In ART the im-
age **f** is optimized iteratively with the relation

$$\mathbf{f}^n = \mathbf{f}^{n-1} - \frac{\mathrm{a}_i\mathbf{f}^{n-1} - \mathbf{p}_i}{\mathrm{a}_i(\mathrm{a}_i)^T}(\mathrm{a}_i)^T, \tag{1.3}$$

where $\mathbf{f}^n$ denotes the nth iteration of the image **f**, and a_i is the ith row of the
matrix **A**. Figure 1.4 shows an example of ART for two dimensions for the case
a unique solution is present and for the case no unique solution is present. The
initial image, the zero image, is projected perpendicular onto the first line that
represents the first ray with projection $\mathbf{p}_1$. When the two lines are perpendicular
to each other, it is in principle possible to reach the intersection point in two it-
erations.
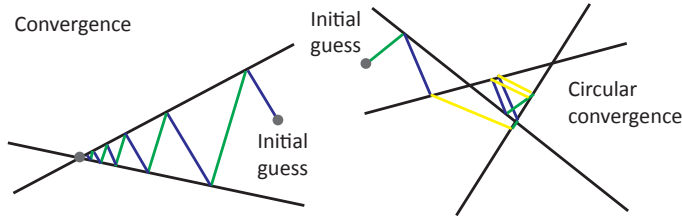
Figure 1.4: Schematic illustration of algebraic reconstruction convergence in case a unique solution is present (left) and circular convergence for the case a unique solution is absent (right)[16].

The uniqueness of the solution **f** is characterized by the rank of the matrix **A**, which is equal to the number of linearly independent columns. When the lines are close to parallel, i.e., the columns are close to linearly dependent; convergence is slow and may lead to finding a non-unique solution. If there is no unique solution, cyclic convergence may occur in which the found solution circles around the most optimal solution, see Fig. 1.4 (right).

In general, iterative methods have the advantage that they can include prior information about the possible solution and include physical mechanisms of the imaging process, such as the beam shape. In contrast to analytical reconstruction, iterative methods are computationally more expensive and require a longer computation time. Other tomographic reconstruction techniques based on algebraic reconstruction are simultaneous iterative reconstruction technique (SIRT) or simultaneous algebraic reconstruction technique (SART).

An alternative iterative reconstruction method is least squares (LSQR) optimization in which the image of the object is determined by finding the optimum of

$$\mathbf{f}_{LS} = \min_{\mathbf{f}} \frac{1}{2} ||\mathbf{Af} - \mathbf{p}||_2^2 \tag{1.4}$$

using, for example, conjugate gradient optimization methods.

1.3. Optical tomographic imaging

Optical tomographic imaging has the advantage of being based on non-ionizing radiation, having high tissue contrast, high spatial resolution, and being cost efficient. In this thesis we focus on two imaging techniques: optical projection tomography (OPT) and transmission optical coherence tomography (OCT).

In OPT, light intensity projections of samples are measured in transmission or emission (fluorescence) mode. From these projections, images of the object are reconstructed using tomographic reconstruction algorithms (see Section 1.2). A schematic illustration of an emission OPT system is given in Fig. 1.5, where the sample is illuminated by a light source to excite the fluorophores in

the object and the emitted light is detected orthogonal to the incoming light with a camera. OPT imaging of cells and small organisms can be performed in-vivo.
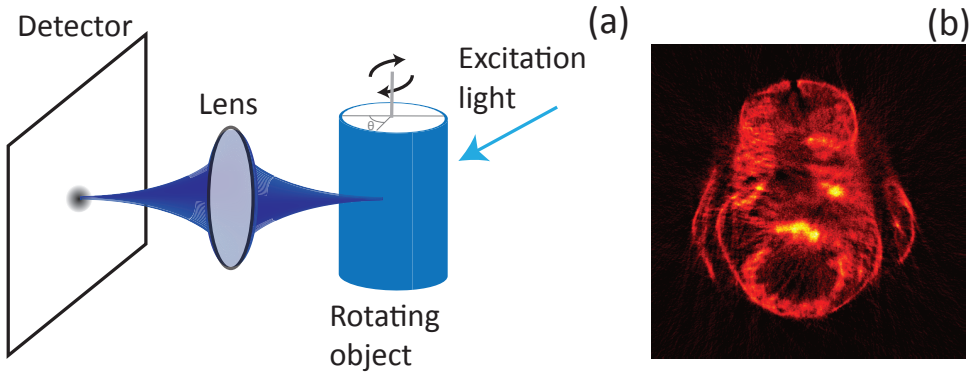
Figure 1.5: (a) Schematic overview of the optical projection tomography fluorescence imaging geometry. (b) Emission OPT reconstruction of a zebrafish using filtered back projection.

However, imaging of larger tissues requires optical clearing to suppress light scattering and is only possible ex-vivo.

Another non-invasive optical imaging technique is OCT [7], which can be described as the optical equivalent of ultrasound imaging where a high frequency sound pulse is send into the sample and the delay of this pulse is measured. In OCT, however, the delay of the reflected backscattered light is detected using the interference of low-coherence light in a Michelson interferometer, see Fig. 1.6 (a). OCT is able to perform high resolution ($2-10\,\mu$m) and cross-sectional imaging [7] up to an imaging depth of approximately $1-2$ mm.

OCT is not only used in reflection, but also imaging in transmission mode is possible. This was introduced by Hee et al. [18], where time gating was used to image objects buried in scattering media. They obtained en-face transmission OCT images, where only contrast (and not depth) information is given. Due to the time-gated rejection of multiple scattered light the contrast in the image is significantly enhanced. Parallel to Hee, Inaba et al. [19] imaged chicken tissue using optical computed tomography to obtain a cross-sectional image. Other transmission optical tomographic imaging techniques have been developed. Optical coherence computed tomography (OCCT) by Li and Wang [20] was used to measure the arrival times of diffuse photons using low-coherence interferometry. Projection index computed tomography by Zysk et al. [21], where OCT in transmission, but with a retro-reflector, is used to measure a projection of the refractive index of the object. Subsequently, the refractive index of the object is reconstructed from projections measured at various angles with filtered back projection.
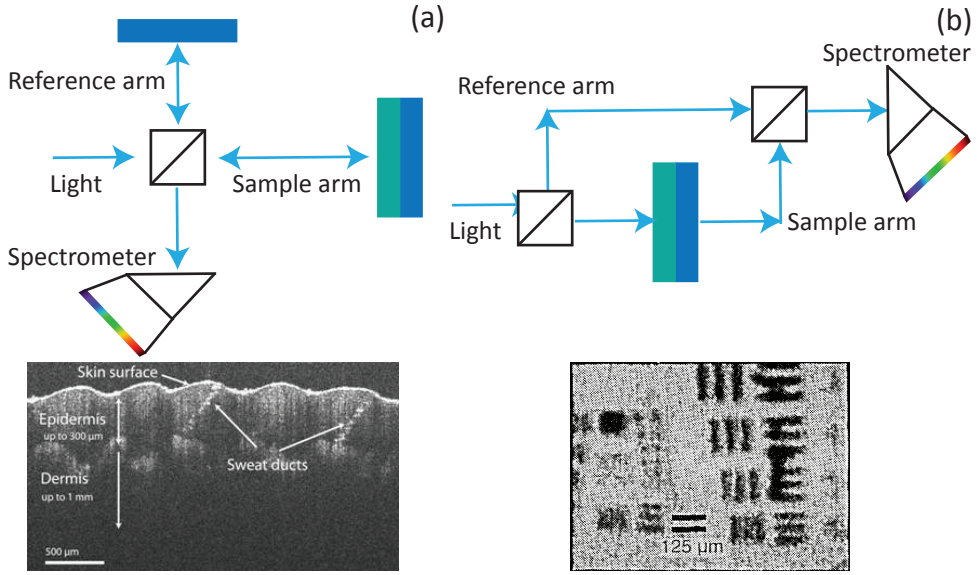
Figure 1.6: (a) Reflection-based spectral-domain OCT setup. (b) OCT cross-sectional image of the human skin [17]. (c) Transmission-based spectral-domain OCT setup. (d) Time-gated transmission image from bars embedded in a solution of silica particles [18].

1.4. Challenges in optical tomography

High resolution deep tissue optical imaging is challenging due to the effects of light absorption, scattering, and diffraction on the imaging process. Here these issues are discussed in more detail.

1.4.1. High contrast deep tissue imaging

Since tissue consists mainly of water, water absorption is of critical importance for imaging inside tissue. To obtain a large penetration depth a low absorption coefficient, denoted as μ_a, is favorable. Figure 1.7 shows the absorption coefficient of water as a function of wavelength. The spectrum shows low water absorption in the X-ray and radio frequency part of the spectrum and a low absorption window for optical wavelengths. Imaging in this optical window allows an imaging depth of up to a few centimeters [24]. However, in addition to absorption optical radiation also scatters in tissue and the combined effect is described as as $\mu_t = \mu_a + \mu_s$, with μ_s the scattering coefficient. The scattering coefficient of blood in the optical window is shown in Fig. 1.7. The scattering coefficient, denoted as μ_s, is much larger than the absorption coefficient. Hence, for optical wavelengths light scattering is more important for the imaging depth than light absorption. When scattering occurs, the light deviates from its straight ray path.
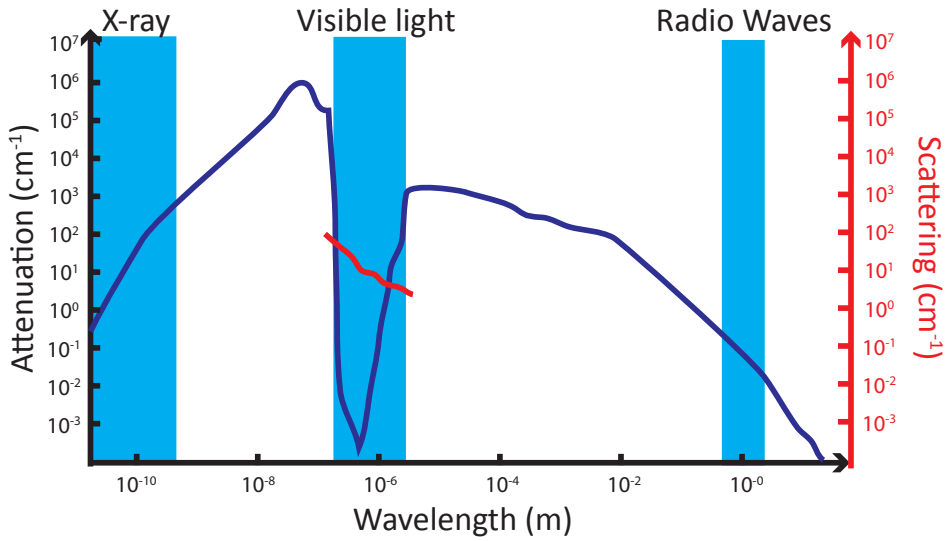
Figure 1.7: Absorption coefficient of water [22] and scattering coefficient of blood [23] as a function of wavelength.

If many of these scattering events take place, as is the case for tissue, it causes a strong reduction of signal and contrast in the image. Figure 1.8 demonstrates the effect of scattering on image formation. On the left an X-ray image is shown. For X-rays, scattering does not play a large role in the image formation resulting in a high absorption contrast between bone and tissue. On the right, a visible light transmission image of a human hand is shown. Even though light absorption at these wavelengths is quite low, light scattering results in a glow of transmitted light through all tissue. As a result, the contrast in the image is absent and no structures inside the fingers can be observed. Various methods have been developed to enable deep tissue imaging with light.

Optical clearing or multi-photon imaging are techniques that aim to reduce the amount of scattering. In optical clearing, the penetration of an optical clearing agent with a high refractive index into the tissue leads to refractive index matching between tissue components and thus to a reduction of light scattering [28]. In multi-photon imaging the combined absorption of multiple longer wavelength photons results in imaging with reduced scattering in tissue as the scattering strength decreases with longer wavelengths. Other techniques have focused on rejecting (multiple) scattered light from the detected signal. In confocal gating, a detection pinhole restricts the light reaching the detector to a confined spot [29]. The combination of confocal and time gating is used in time-domain OCT, in which the light reaching the detector has to be coherent with
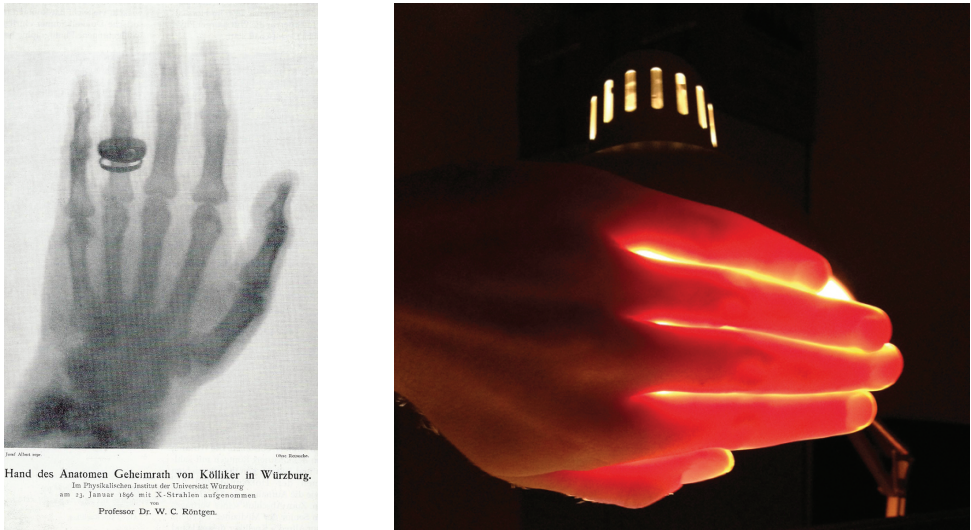
Figure 1.8: Left: X-ray image of the hand of Albert von Kölliker made by Wilhelm Röntgen [26]. Right: optical transmission image of the human hand. [27]as a function of wavelength.

light from the reference arm and have a travel time corresponding to the confocal gate position.

1.4.2. High resolution tomographic imaging

Diffraction is the change of direction of waves as they pass through an object or opening. In optical imaging systems, light is focused by a lens. However, due to diffraction the light does not converge into a single point but into a bigger sized spot. As a result light that is focused from an object onto a detector cannot be assumed to travel down a straight ray through the object. Hence, the, straight ray approximation, such as used in CT, cannot be assumed to be a valid description in optical projection tomography. Instead of sampling the object along a line, the volume of the object is sampled by the spatially varying light beam. Consequently, reconstruction with FBP, which is based on straight ray propagation, leads to blurred tomographic images with low spatial resolution.

1.4.3. Zebrafish imaging

A common model system for developmental research and pre-clinical research is the zebrafish *(Danio rerio)*, which is a tropical freshwater fish. The zebrafish belongs to the family of carp fish *(Cyprinidae)* and the first naming of the species was in 1822. The zebrafish is an important model system for scientific research since the early 60s [31]. It has been shown that 70 per cent of human genes and 84
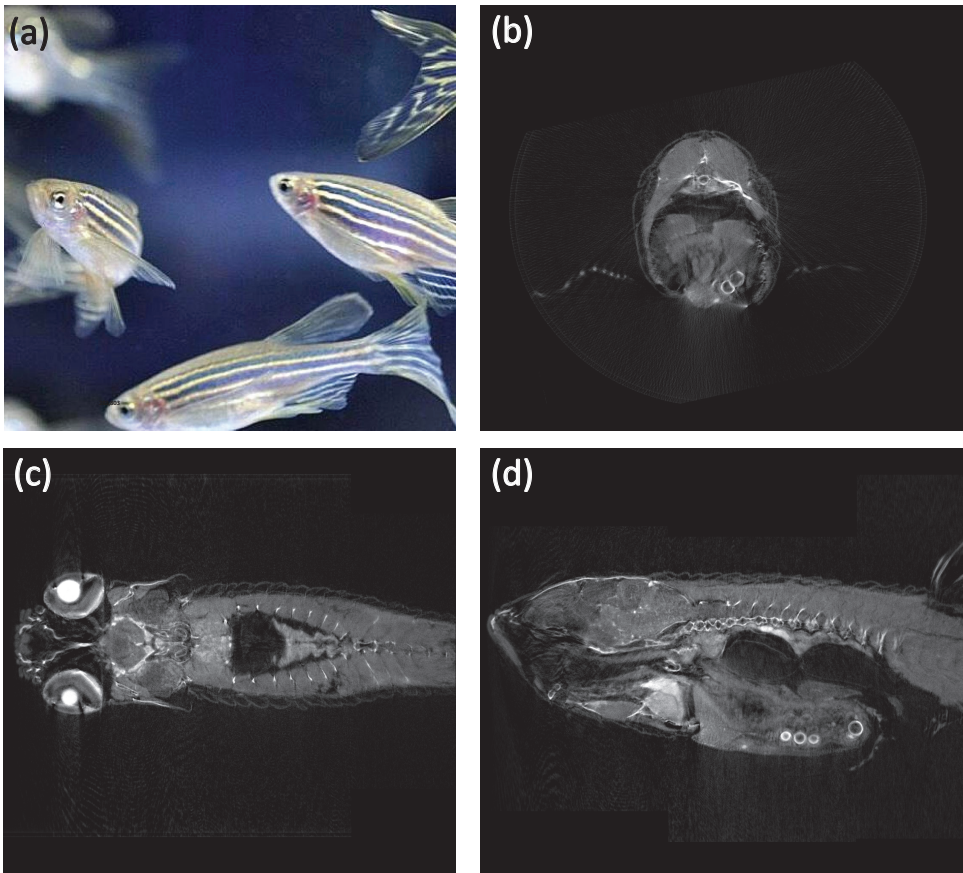
Figure 1.9: (a) Adult zebrafish (wild type) [30]; OPT image of an adult zebrafish [5]. (b) Transverse view, (c) coronal view, (d) sagittal view.

per cent of genes associated with human diseases are also found in the zebrafish [31, 32]. Various zebrafish model systems have been developed for diseases such as cancer, Duchenne muscular dystrophy, and diabetes [31, 33]. The adult zebrafish is available with a striped skin (wild type) and without stripes (nacre). An adult fish is about 2.5 cm to 4 cm long and about 5 mm thick. In zebrafish research, optical imaging is frequently used due to the transparent nature of the larvae. High resolution in-vivo imaging of adult zebrafish has been challenging due to light scattering and light diffraction. Figure 1.9(b-d) shows transmission OPT images of a cleared adult zebrafish in three orthogonal anatomical planes.

1.5. Thesis objectives
In the previous section we discussed the challenges in optical tomography, which lead to the following thesis objectives:

- to develop transmission OCT signal algorithms for quantitative tomographic imaging in turbid media and to quantify parameters in 3D tomographic images.

- to develop methods to mitigate the effects of diffraction in optical tomographic images.

1.6. Outline of this thesis
This thesis focuses on the modeling of the optical signal for transmission OCT and the development of reconstruction algorithms for optical tomography.

In Chapter 2, we present transmission optical coherence tomography (transmission OCT) as a versatile tool to measure optical material properties of turbid media. First, we model the transmission OCT signal and we demonstrate how the group refractive index (n_g), group velocity dispersion (GVD) and optical attenuation can be determined from this signal. The measured refractive index properties of glasses, liquids, and glucose water solutions are quantified in terms of n_g and GVD and compared to literature. In addition, measurements of scattering coefficients are determined using transmission OCT measurements of suspensions of silica particles.

In Chapter 3, we show a tomographic application of the in Chapter 2 presented transmission OCT technique. Optical coherence projection tomography is a novel interferometric imaging modality for non-diffuse 3D optical imaging of an adult zebrafish whereby quantitative images of refractive index and optical attenuation of millimeter-sized samples by time gating of scattered light are reconstructed. In this chapter we show how the images generated with this technique are analyzed by segmenting zebrafish organs and determining their median optical properties and volumes.

In Chapter 4, a point spread function (PSF) based optical tomographic image reconstruction technique is presented. As a result of the shallow depth of focus of the optical imaging system, standard filtered back projection causes space-variant tangential blurring that increases with the distance to the rotation axis. Our approach incorporates the optical imaging geometry in an iterative PSF-based reconstruction. The technique is demonstrated using numerical simulations, tested on experimental optical projection tomography data of single flu-

orescent beads, and applied to high-resolution emission optical projection tomography imaging of an entire zebrafish larva.

In Chapter 5, we present a comparison of image reconstruction techniques for optical projection tomography. We compare conventional filtered back projection, sinogram filtering using the frequency-distance relationship (FDR), image deconvolution, and 2D point spread function (PSF) based iterative reconstruction. The latter three methods aim to remove the spatial blurring in the reconstructed image originating from the limited depth of field caused by the PSF of the optical imaging system. The methods are compared based on simulated data, experimental optical projection tomography data of single fluorescent beads, and high-resolution optical projection tomography imaging of an entire zebrafish larva.

In Chapter 6, we extend the 2D PSF-based reconstruction algorithm, presented in Chapter 5, to three dimensions. With simulations we compare the filtered back projection, and the 2D/3D PSF-based reconstructions with each other. As a proof of principle the proposed algorithm is applied to high-resolution emission optical projection tomography imaging of a zebrafish larva. We show that the 3D PSF-based reconstruction, with the 2D PSF-based reconstruction as an input results in an improved signal-to-background ratio and a better image quality.

Chapter 7 presents the conclusion and outlook of this thesis.

References

[1] B. Driehuys, J. Nouls, A. Badea, E. Bucholz, K. Ghaghada, A. Petiet, and L. W. Hedlund, "Small animal imaging with magnetic resonance microscopy," *ILAR J.*, vol. 49, no. 1, pp. 35–53, (2009).

[2] A.-H. Liao and P.-C. Li, "The role of high frequency ultrasound in multi-modality small animal imaging for cancer research," *J. Med. Ultrasound*, vol. 17, no. 2, pp. 86–97, (2009).

[3] http://www.mouseimaging.ca/technologies/ubm.html, downloaded 2018.

[4] M. D. Wong, A. E. Dorr, J. R. Walls, J. P. Lerch, and R. M. Henkelman, "A novel 3D mouse embryo atlas based on micro-CT," *Development*, vol. 139, no. 17, pp. 3248–56, (2012).

[5] D. Salgado, C. Marcelle, P. D. Currie, and R. J. Bryson-Richardson, "The zebrafish anatomy portal: a novel integrated resource to facilitate zebrafish research," *Developmental Biology*, vol. 372, no. 1, pp. 1–4, (2012).

[6] S. J. Schambach, S. Bag, L. Schilling, C. Groden, and M. A. Brockmann, "Application of micro-CT in small animal imaging," *Methods*, vol. 50, no. 1, pp. 2–13, (2009).

[7] D. Huang, E. A. Swanson, C. P. Lin, J. S. Schuman, W. G. Stinson, W. Chang, M. R. Hee, T. Flotte, K. Gregory, C. A. Puliafito, J. G. Fujimoto, "Optical coherence tomography" *Science*, vol. 254, no. 5035, pp. 1178-1181, (1991).

[8] M. Hee, J. Izatt, and E. Swanson, "Optical coherence tomography of the human retina," *Archives of Ophthalmology*, vol. 113, no. 3, pp. 325–332, (1995).

[9] Z. Ding, C. Liang, and Y. Chen, "Technology developments and biomedical applications of polarization-sensitive optical coherence tomography," *Front. Optolelectron.*, vol. 8, no. 2, pp. 128–140, (2015).

[10] J. Sharpe, U. Ahlgren, P. Perry, B. Hill, A. Ross, J. Hecksher-Sørensen, R. Baldock, and D. Davidson, "Optical projection tomography as a tool for 3D microscopy and gene expression studies," *Science*, vol. 296, no. 5567, pp. 541–545, (2002).

[11] E. Wolf, "Three-dimensional structure determination of semi-transparent objects from holographic data," *Opt. Commun.*, vol. 1, no. 4, pp. 153–156, (1969).

[12] G. V. Babiera, R. J. Skoracki, and F. J. Esteva, *Advanced therapy of breast disease*. PMPH USA, (2012).

[13] O. Falou, H. Soliman, A. Sadeghi-Naini, S. Iradj, S. Lemon-Wong, J. Lemon-Wong, J. Lemon-Wong, R. Dent, M. Trudeau, J. F. Boileau, F. Wright, M. Yaffe, and G. J. Czarnota, "Diffuse optical spectroscopy evaluation of treatment response in women with locally advanced breast cancer receiving neoadjuvant chemotherapy," *Transl. Oncol.*, vol. 5, no. 4, pp. 238–246, (2012).

[14] J. Radon and P. Parks, "On the determination of functions from their integral values along certain manifolds," *IEEE Trans. Med. Imaging*, vol. 4, p. 170–176, (1986). Translation of the original paper by Johann Radon 1917.

[15] J. Hadamard, "Sur les problèmes aux dérivées partielles et leur signification physique," *Princeton University Bulletin*, (1902).

[16] P. C. Hansen, "Algebraic methods for computed tomography," *Technical University of Denmark,COST/HD-Tomo Training School*, pp. 1–17, download 2017.

[17] S. V. der Jeught, "Master thesis: High-speed digital signal processing in optical coherence tomography using a graphics processor unit," *University of Antwerpen, Belgium*, (2010).

[18] M. R. Hee, E. A. Swanson, J. A. Izatt, J. M. Jacobson, and J. G. Fujimoto, "Femtosecond transillumination optical coherence tomography," *Opt. Lett.*, vol. 18, no. 12, pp. 950–952, (1993).

[19] H. Inaba, "Coherent detection imaging for medical laser tomography medical optical tomography: Functional imaging and monitoring," *Proc. SPIE*, vol. 10311, pp. 317–47, (1993).

[20] L. Li and L. V. Wang, "Optical coherence computed tomography," *Appl. Phys. Lett.*, vol. 91, pp. 141107 1–3, (2007).

[21] A. M. Zysk, J. J. Reynolds, D. L. Marks, P. S. Carney, and S. A. Boppart, "Projected index computed tomography," *Opt. Lett.*, vol. 28, no. 9, pp. 701–3, (2003).

[22] B. W. Pogue, "Optics in the molecular imaging race," *Optics and photonics news*, vol. 26, no. 9, pp. 26–31, (2015).

[23] M. E. Vuylsteke, P. J. Vandekerckhove, T. Bo, and P. S. Mordon, "Use of a new endovenous laser device: Results of the 1500 nm laser," *Ann. Vasc. Surg.*, vol. 24, no. 2, pp. 205–11, (2010).

[24] D. A. Boas, D. H. Brooks, E. L. Miller, C. A. DiMarzio, M. Kilmer, R. J. Gaudette, and Q. Zhang, "Imaging the body with diffuse optical tomography," *IEEE Signal Processing Magazine*, vol. 18, no. 6, pp. 57–75, (2001).

[25] L. Shi, L. A. Sordillo, A. Rodríguez-Contreras, and R. R. Alfano, "An optical window for deep brain imaging," *J. Biophot.*, vol. 9, no. 1-2, pp. 38–43, (2016).

[26] *http://wilhelmconradroentgen.de/en/about-roentgen*, downloaded 2017.

[27] D. Psaltis and I. N. Papadopoulos, "Imaging: The fog clears," *Nature*, vol. 8, no. 491, p. 197–198, (2012).

[28] D. Zhu, K. V. Larin, Q. Luo, and V. V. Tuchin, "Recent progress in tissue optical clearing," *Laser Photon. Rev.*, vol. 7, no. 5, pp. 732–757, (2013).

[29] F. Mauch, W. Lyda, and W. Osten, "Object depending measurement uncertainty of confocal sensors," *Fringe*, pp. 465–470, (2013).

[30] *https://www.cnbc.com/2017/08/25/what-drug-addled-zebrafish-can-tell-us-about-addiction.html*, (2017).

[31] "Why use the zebrafish in research?," *https://www.yourgenome.org/facts/why-use-the-zebrafish-in-research* , downloaded 2016.

[32] K. Howe et al., "The zebrafish reference genome sequence and its relationship to the human genome," *Nature*, vol. 496, pp. 498–503, (2013).

[33] *https://irp.nih.gov/blog/post/2016/08/why-use-zebrafish-to-study-human-diseases*, downloaded 2016.

Chapter 2

Transmission optical coherence tomography based measurement of optical material properties

We present transmission optical coherence tomography (transmission OCT) as a versatile tool to measure optical material properties of turbid media. The transmission OCT signal is described in detail and it is demonstrated how the group refractive index (n_g), group velocity dispersion (GVD) and optical attenuation can be determined from this signal. We experimentally validate the refractive index properties of glasses, liquids and glucose water solutions in terms of n_g and GVD. Measurements of scattering coefficients are determined using transmission OCT for suspensions of silica particles. Quantitative agreement is obtained with a dependent scattering model, both for the average as well as the wavenumber resolved optical attenuation coefficient. Good agreement is observed between our measurements and literature values.

2.1. Introduction

Optical material properties are important in the field of optics where they are paramount to the production of high quality optical components. Also in other fields such as pharmaceuticals, medical imaging, photo-dynamic therapy and food production are optical material properties important for quality control and diagnostics. However, in contrast to optical materials such as glasses, the optical materials in these fields are turbid, i.e., they have both optical absorption and scattering. Consequently, the characterization of their optical properties such as refractive index (dispersion) and optical attenuation is a lot more challenging.

Collimated transmission measurements, for example, can be used to measure the total attenuation coefficient of turbid media [1]. However, the difficulty with this method is to avoid measuring scattered light on the detector, which is

done using pinholes and long path lengths, but nevertheless restricts the measurements to relatively thin samples. Diffuse reflectance spectroscopy has been used to measure the wavelength dependent absorption coefficient and the reduced scattering coefficient to identify the age of bloodstains, where the change of hemoglobin fractions can be observed over time [2]. Yet, diffuse reflectance spectroscopy requires the use of transport theory to calculate the optical properties. Consequently, this technique is limited to samples that are homogeneous or have a known structure. A combination of transmittance and diffuse reflectance measurements can also be used to determine the absorption coefficient, the scattering coefficient and the scattering anisotropy of turbid media [3], but also suffers from the above mentioned effects.

Some techniques are capable of measuring the spatial variation in optical properties, producing an image of the sample. Optical coherence tomography (OCT) has been used to measure light attenuation of tissue and is able to differentiate between normal and tumorous tissue [4]. Low-coherence spectroscopy has been used to image the wavelength dependent absorption and scattering coefficient in vivo in the human skin [5]. Imaging of the refractive index in turbid media has been shown using bifocal OCT [6]. By measuring the optical path length between two focal spots in a sample the refractive index can be obtained. It is also possible to measure the refractive index of turbid media using confocal microscopy [7]. In this case, a layer of immersion fluid of the same thickness as the sample is used in combination with a calibrated z-stage movement. Optical properties of tissue can provide functional information regarding its biological state. The use of optical techniques for biopsies has been shown for example by Wang et al. [8], who demonstrated quantitative phase imaging of breast and prostate biopsies to identify tumor calcifications.

All the techniques described above only provide measurement of either the refractive index or the attenuation coefficients. Part of these techniques rely only on diffuse light while others suffer from it, causing restrictions on the sample size and the type of sample.

Here, we present Fourier-domain transmission optical coherence tomography (transmission OCT) that is used to determine both the refractive index and optical attenuation coefficients. Transmission OCT was first used by Hee et al. [9] for imaging of objects embedded in turbid media. Recently, transmission OCT has been used to measure the scattering coefficient μ_s in turbid media [10]. We show that transmission OCT can provide an estimation of the group refractive index, n_g, the group velocity dispersion, GVD, as well as the (spectrally resolved) total attenuation coefficient of the material. The advantage of using transmission OCT is the combination of confocal gating and path-length selectivity (coherence gating). This allows for a strong rejection of scattered light, as well as the

possibility to further filter out multiple scattered light.

First, a theoretical framework is provided that describes the transmission OCT in the presence of attenuation and dispersion. Second, the experimental setup is described together with an algorithm to analyze the experimental data. Finally, experimental data is presented that demonstrates the proposed techniques.

2.2. Theory

2.2.1. The transmission Fourier domain OCT signal

Transmission OCT is based on the interaction of light in the sample arm of a Mach-Zehnder interferometer with light propagating in the reference arm. A schematic diagram of the Mach-Zehnder interferometer with spectral-domain detection as used for transmission OCT is given in Fig. 2.1. The experimental realization of the setup is described in more detail in Section 2.3.1.
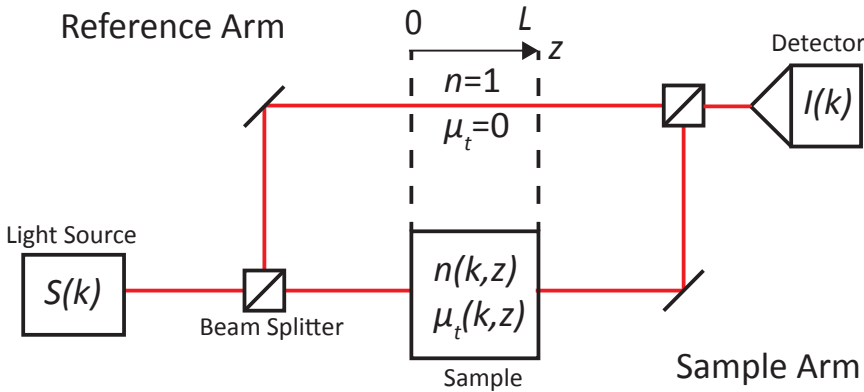
Figure 2.1: Schematic diagram of the Fourier-domain transmission OCT system. $I(k)$: detected intensity at the spectrometer, L: length of the sample, $n(k, z)$: refractive index of the sample, $\mu_t(k, z)$: total attenuation, $S(k)$: source intensity

Light from the light source is launched into the interferometer. The source intensity spectrum is given by $S(k) = E_s(k)^* E_s(k)$, with $*$ denoting complex conjugation, k is wavenumber in vacuum $k = 2\pi/\lambda$ and $E_s(k)$ are plane electromagnetic waves. In the following, we assume one-dimensional rectilinear propagation of scalar plane waves light field through the interferometer. Polarization and multiple scattering are neglected in our model. Due to averaging over many optical cycles, the time dependence of the signals is disregarded and all parameters are real numbers unless stated otherwise. We neglect any path lengths and phase factor that are equal for both interferometer arms. The incoming beam is

first split and later combined by an ideal beam splitter with an (intensity) reflection coefficient of α and transmission coefficient $1 - \alpha$.

For the light wave propagating in the reference arm we assume it to be filled with air, i.e. the refractive index is unity, $n(k, z) = 1$ and there is no attenuation, $\mu(k, z) = 0$. Assuming ideal mirrors in the interferometer with unity reflectivity, the reference arm field $E_{ref}(k)$ at the detector is given by

$$E_{ref}(k) = [\alpha(1 - \alpha)]^{\frac{1}{2}} E_s(k) \exp(ikL), \tag{2.1}$$

where $i = (-1)^{1/2}$, and where L is the physical length equal to the physical length in the sample arm in which interaction takes place. After interaction with a sample of length L in the sample arm the field from the sample arm falling on the detector is

$$E_{sam}(k) = [\alpha(1 - \alpha)]^{\frac{1}{2}} E_s(k) \exp\left(-\frac{1}{2} \int_0^L \mu_t(k, z) dz\right) \exp\left(ik \int_0^L n(k, z) dz\right), \tag{2.2}$$

where $\mu_t(k, z)$ is the total attenuation coefficient and L is the distance along the optical path in the sample arm where interaction takes place. In the following we consider only homogeneous media, i.e. $\mu(k, z) = \mu(k)$ and $n(z, k) = n(k)$, and the integrals are replaced by multiplications with L. The total intensity at the detector $I(k) = (E_{ref}(k) + E_{sam}(k))(E_{ref}(k) + E_{sam}(k))^*$ consists of the reference arm intensity, the sample arm intensity and the cross terms which contain the interference signal. Combining Eq. 2.1 and Eq. 2.2, and retaining only the interference term of the intensity on the detector we obtain

$$I_{int}(k) = 2\alpha(1 - \alpha) E_s^2(k) \exp\left(-\frac{1}{2} L \mu_t(k)\right) \cos[kL(n(k) - 1)]. \tag{2.3}$$

The measured interference signal is proportional to an exponential factor describing the optical attenuation and is proportional to a cosine with a phase that is modulated by the spectral variation of the refractive index (dispersion).

2.2.2. Material dispersion

The term $n(k) - 1$ in Eq. 2.3 represents the dispersive properties of the sample. Commonly, the dependence of the refractive index of a material with wavelength is expressed by the Sellmeier equation [11]. Here, we make a polynomial expansion of n around k_c, the center wavenumber of the source spectrum $S(k)$:

$$n(k) = \sum_{j=0}^{J} n_j \left(\frac{k - k_c}{k_c}\right)^j, \tag{2.4}$$

with a total number of coefficients $J \in \mathbb{N}$. Based on the literature values for the parameters of the Sellmeier equation or experimental data presenting $n(\lambda)$, the coefficients n_j of the polynomial expansion can be determined using a fit. Another common way to describe the dispersive properties of a material is in terms of the group refractive index and the GVD. At the center wavenumber, these are given by $n_g(k_c) = n(k) + k (\mathrm{d}n/\mathrm{d}k)|_{k=k_c}$ and $GVD(k_c) = 1/c^2 (\mathrm{d}n_g/\mathrm{d}k)|_{k=k_c}$, respectively. Here c is the speed of light.

The dependence of $n(k)$ on k, from Eq. 2.4, causes the oscillations of the cosine in Eq. 2.3 to be non-linear. For the attenuation analysis (Section 2.2.3) and for the dispersion estimation, the phase of the signal of Eq. 2.3 has to be extracted. Therefore the analytical signal of the interference signal is calculated [12, 13], which is given by

$$\widetilde{I_{int}}(k) = I_{int}(k) + i\mathcal{H}\{I_{int}(k)\}, \tag{2.5}$$

where $\mathcal{H}\{\cdot\}$ denotes the Hilbert transform operator. The phase of $\widetilde{I_{int}}(k)$ can then be determined by

$$\varphi(k) = \tan^{-1}\left(\frac{\mathcal{H}\{I_{int}(k)\}}{I_{int}(k)}\right), \tag{2.6}$$

which is equal to the argument of the cosine expression in Eq. 2.3 performing a Taylor expansion of $\varphi(k)$ around k_c and combining this with the polynomial expansion of $n(k)$ around k_c in Eq. 2.4 for $J = 2$, we obtain

$$\frac{\varphi(k)}{k_c L} = (n_0 - 1) + (n_0 - 1 + n_1)\left(\frac{k - k_c}{k_c}\right) + (n_1 + n_2)\left(\frac{k - k_c}{k_c}\right)^2. \tag{2.7}$$

The coefficients of Eq. 2.7 can be determined by fitting $\varphi(k)$ with a polynomial. From the fit parameters coefficients, n_0 and n_1, are determined and the group refractive index follows as $n_g(k_c) = n_0 + n_1$ and the group velocity dispersion $GVD(k_c) = 2(n_1 + n_2)/(k_c c^2)$.

In the z-domain, the dispersion leads to a broadening of the transmission peaks. Using the complex notation of the analytical signal it is easy to see that the phase can be linearized by multiplying the Hilbert transformed interference signal with $\exp[i\Delta\varphi(k)]$, where $\Delta\varphi(k) = \varphi(k) - \varphi_{\text{linear}}(k)$ [13]. The dispersion corrected signal in the z-domain is given by the inverse Fourier transform of the dispersion corrected analytic signal

$$I_c(z) = \mathcal{F}^{-1}\{|\widetilde{I_{int}}(k)| \exp[i\Delta\varphi(k)]\}, \tag{2.8}$$

where $\mathcal{F}^{-1}\{\cdot\}$ denotes the inverse Fourier transform of the given signal.

2.2.3. Attenuation coefficient

After dispersion correction, the attenuation coefficient can be determined both from the spectral or spatial domain signal. Taking the inverse Fourier transform of Eq. 2.3 and assuming the attenuation does not vary a lot over the spectral bandwidth of the system, i.e. $\mu_t(k) = \mu_t$, we obtain an equation for the spatial domain transmission OCT signal

$$
\begin{aligned}
a(z) = &\alpha(1-\alpha)\exp\left(-\frac{1}{2}L\mu_t\right)\mathscr{F}^{-1}\{E_s^2(k)\}(z) \\
&\otimes\left[\delta\left(z - L(n_g-1)\right) + \delta\left(z + L(n_g-1)\right)\right],
\end{aligned}
\tag{2.9}
$$

where $\otimes$ denotes a convolution. Performing a reference measurement with attenuation $\mu_t = 0$ and a measurement on the sample, one obtains two z-domain signals. The signal of the sample differs from that of the reference measurement by a possible shift of the delta functions and a change in height, caused by the optical attenuation. From Eq. 2.9 it can be deduced that the attenuation coefficient can be determined by measuring the height of the peak in the z-domain of the reference and sample measurements, a_{ref} and a_{sam}, respectively, and using

$$
\mu_t = \frac{2}{L}\ln\left(\frac{\max|a_{ref}|}{\max|a_{sam}|}\right).
\tag{2.10}
$$

The attenuation coefficient thus obtained is an average over the spectral bandwidth of the system. The spatial domain analysis offers the advantage of pathlength selectivity. In this way the ballistic light can be filtered from the scattered light, which can then be used to estimate the attenuation μ_t and the refractive index of the sample.

Alternatively, from Eq. 2.3 and Eq. 2.8 the absolute value of the analytical signal can be recognized as the complex magnitude of the interference signal

$$
|\widetilde{I_{int}}(k)| = \alpha(1-\alpha)E_s^2(k)\exp\left(-\frac{1}{2}L\mu_t(k)\right).
\tag{2.11}
$$

The wavenumber dependent attenuation coefficient $\mu_t(k)$ can be determined by performing a reference and a sample measurement of $|\widetilde{I_{int}}(k)|$. Similar to Eq. 2.10, the ratio of these two signals then results in $\mu_t(k)$.

2.3. Methods

2.3.1. Experimental setup

The Fourier domain transmission OCT setup is depicted in Fig. 2.2. It is based on a Mach-Zehnder interferometer with spectral domain detection of the interference signal. A fiber based super-luminescent diode (D-1300-HP, Superlum)

with a center wavelength of 1300 nm and a full width half maximum (FWHM) bandwidth of 110 nm is used as a light source. After collimation by an achromatic doublet lens (AC254-045-C-ML, Thorlabs), the light is split into the reference and sample arm by a 50/50 beamsplitter (BS015, Thorlabs). Optical power in the two arms is regulated by neutral density filters (NDC-100C-4M, Thorlabs) in each arm. The reference arm contains an optical delay line, that is tunable in length by means of a translation stage (PT1/M, Thorlabs). The sample arm contains two confocal 200 mm achromatic lenses (AC254-200-C-ML, Thorlabs). Samples are mounted in the focal point between the two lenses. After recombination by a second 50/50 beamsplitter the resulting beam is expanded by a 4-f lens system (AC254-060-C-ML and AC508-080-C-ML, Thorlabs) before being introduced to a spectrometer. A pinhole is placed at the focus position between the two lenses of the 4-f system to remove any stray light. Spectral domain detection is performed by a home build spectrometer, consisting of a holographic grating (1145 l/mm, Wasatch Photonics), an SWIR imaging lens (S5LPJ0037/360, Sill Optics), and a 76 kHz InGaAs linescan camera (GL2058L, Sensors Unlimited). Camera data is acquired using a framegrabber (PCIe-1433, National Instruments) and Labview software (National Instruments).
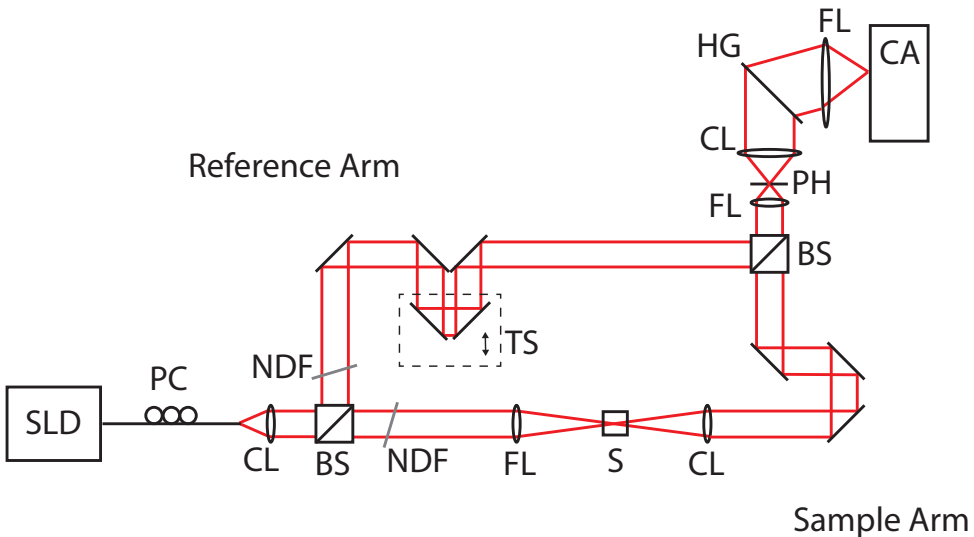

Figure 2.2: Schematic diagram of the experimental setup. BS: beam splitter, CA: camera, CL: collimation lens, FL: focusing lens, HG: holographic grating, NDF: Neutral density filter, PC: polarization controller, PH: pinhole, S: Sample, SLD: superluminescent diode, TS: translation stage

2.3.2. Setup calibration and performance

The spectrometer is calibrated using an Argon gas discharge lamp (AvaLight-CAL-AR, Avantes). The calibration lamp is placed on the free-side of the first beamsplitter of the interferometer. The emission spectrum of the lamp is recorded by the spectrometer and the measured emission lines are compared to reference values from literature. A third degree polynomial is fitted through the data to obtain a relation between pixel number and wavelength. The performance of the transmission OCT system is checked using the movable delay line in the reference arm. This yields a maximum path length difference of 11.6 ± 0.1 mm. The axial resolution of the system is determined by measuring the FWHM of the signal peak in the z-domain with no sample in the interferometer. The measured axial resolution of the system is 18 ± 1 μm, (bandwidth limited). The lateral point spread function, measured in air has an in-focus FWHM waist of 32.8 ± 0.7 μm Following the definition of Nassif et al. [14], the roll-off parameter of the system is $w = 2.1 \pm 0.1$. Measurements using neutral density filters show a signal sensitivity of -106 dB.

2.3.3. Sample preparation and measurement

Measurements of n_g and the GVD are performed on both liquid samples and glass plates. The glass plates provide a good validation as the optical material properties for glasses are well known. Four different glass plates are used in the experiments; N-BK7 (WG11050, Thorlabs), sapphire (WG31050, Thorlabs), UV-fused silica (WG41050, Thorlabs) and calcium fluorite (WG51050, Thorlabs). All glass plates are 5 mm thick and uncoated. Liquid samples used for the refractive index measurements are: ethanol (32221, Sigma-Aldrich), de-mineralised water and glucose solutions. These liquids were measured using a 10 mm path length, fused quartz cuvette (CV10Q3500F, Thorlabs) placed in the sample arm. Refractive index data is obtained after averaging of 5000 measurements per sample.

Measurements of attenuation are performed on monodisperse silica particle suspensions and on de-mineralised water. Two different particle sizes are considered; 0.5 μm and 1.5 μm diameter. Silica particles (KI-PSI-0.5P and KI-PSI-1.5P, Kisker Biotech) in powdered form are suspended in de-mineralised water containing 0.3 mM of sodium dodecyl sulphate to prevent aggregation [10]. Suspensions are vortexed for 60 minutes and sonicated for 30 minutes before measurements. All silica particle suspensions are measured in a 1 mm path length cuvette (Z802689-1EA, Sigma-Aldrich) mounted in the sample arm. Calculating the attenuation coefficient for the silica particle suspensions, water is used as a reference in Eq. 2.10. In this way the difference in attenuation between the suspension and water is obtained, removing the contribution of the water absorption to the total attenuation of the sample. Leaving only the scattering con-

tribution by the silica particles $\mu_t = \mu_s$. For all the measurements of silica particle suspensions, including the water reference, 100000 measurements are averaged. The wavelength dependent absorption coefficient of water is determined from 1000 spectra.

The particle-sizes are measured using a Malvern Zetasizer, obtaining a mean diameter of 1138 ± 48 nm for the KI-PSI-1.5P particles and 426.6 ± 61.5 nm for the KI-PSI-0.5P particles. These measured sizes are smaller than the factory values, but are consistent with electron microscopy measurements on the same products from the same manufacturer [10].

2.3.4. Data analysis algorithm

After acquisition the spectral data is stored in raw binary format. It is analyzed using software written in MATLAB (Mathworks, R2014b). An overview of the data processing flow is presented in Fig. 2.3. The data acquisition includes a measured spectrum $I(k)$, a spectrum of the reference arm only, $I_{ref}(k)$, and a spectrum for the sample arm only, $I_{sam}(k)$. Furthermore the calibrated wavenumber k is obtained from a combination of the spectrometer calibration and an optimization algorithm. The polynomial coefficients of the wavenumber calibration is optimized with respect to the group index of water using a trust-region algorithm (MATLAB function *fminunc*). The third order polynomial coefficients of the spectrometer calibration are used as the initial parameter estimate.

As spectrum containing only the interference contribution is generated by subtracting all other contributions, $I_{int}(k) = I(k) - I_{ref}(k) - I_{sam}(k)$. To obtain the average interference spectrum this signal is inverse Fourier transformed, averaged and transformed back. For determination of the analytic signal, Eq. 2.5, the built-in MATLAB function *hilbert* is used. Furthermore, the function *phase* is used to determine and unwrap the phase of the given signal. The phase of the signal is cropped in k by choosing the relative heights of the envelope signal with respect to the peak of the envelope to be larger than 0.25. The phase analysis uses the built-in MATLAB function *fit* to fit a cubic polynomial, Eq. 2.7 using the generalized least squares to the difference of the measured phase and a reference phase versus k.

2.3.5. Dependent scattering calculations

Calculations of the scattering coefficient are performed using a Mie theory [15] and a dependent scattering model. The effect of dependent scattering is taken into account using the structure factor for computation of the scattering efficiency ratio following the work of Nguyen et al. [10]. Although dependent scattering does not take the effects of multiple scattering into account, the model is appropriate for describing the reduction of power of the ballistic light. Only the
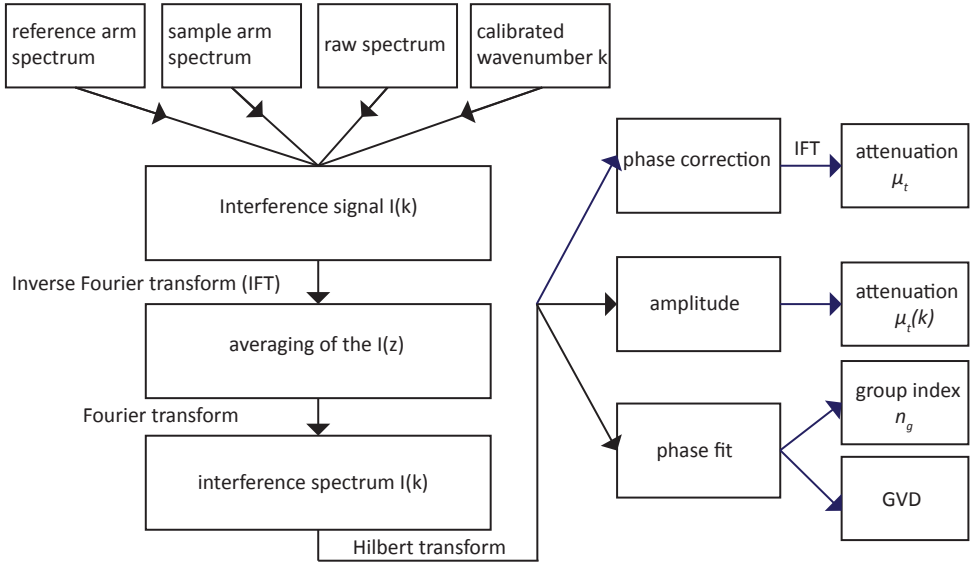
Figure 2.3: Schematic illustration of the analysis algorithm for the determination of the optical material properties.

ballistic photons that scatter for the first time reduce this power. Interactions between multiply scattered light will only affect our path-length distribution at path-lengths beyond that of the ballistic light.

The dependent scattering model uses the Percus-Yevick model to compute the radial distribution function, which accounts for interactions between particles. Furthermore, we assume the Rayleigh-Debye condition is valid, i.e. the scattering particles can be treated as point scatterers. Input to the dependent scattering calculation are the refractive indices of the medium and the suspended particles, the wavelength of the light, the experimentally determined particle radius and the concentration of the particles.

2.4. Results

A typical set of averaged transmission OCT measurements through a fused silica glass slide is shown in Fig. 2.4. Figure 2.4(a) shows the raw interferometric signal versus wavenumber. The instantaneous phase obtained through Hilbert transform of the interference spectrum is shown in Fig. 2.4(b). A linear relation between the start and end point is added to show the non-linearity of the phase. The non-linear behavior of the phase is caused by the cumulative effects of the material dispersion and by the spectrometer dispersion, both indicated. The phase difference between the linear phase and the phase signal from Fig. 2.4(b)
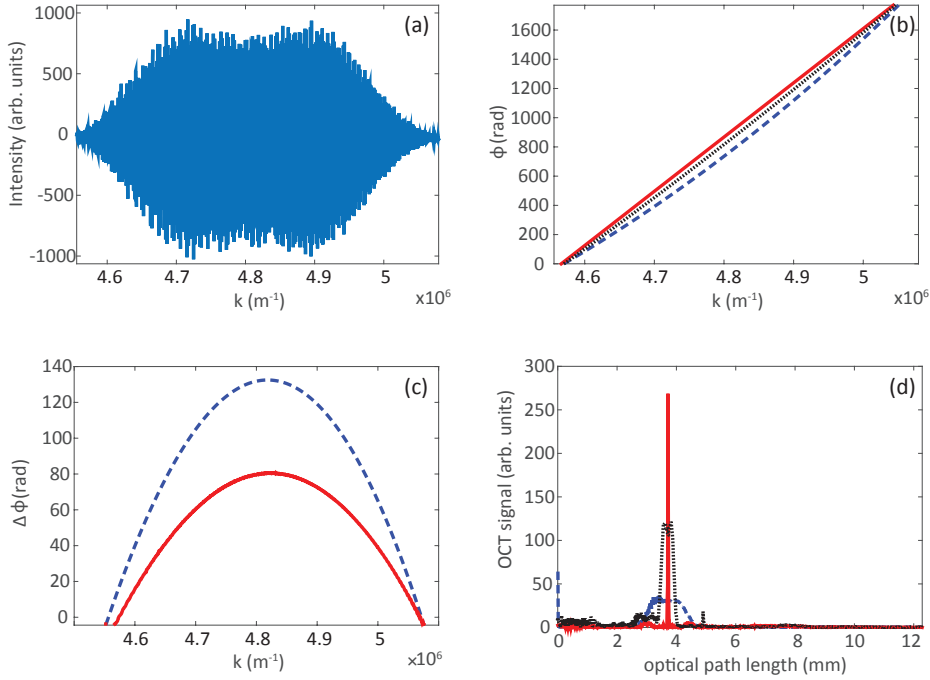
Figure 2.4: Overview of the data processing steps for the fused silica sample (a) Reference and sample arm subtracted interference spectrum. (b) Phase of the original Hilbert transformed signal (blue, dashed), the spectrometer corrected signal (black, points), and the linear phase relation (red). (c) Phase difference between the linear phase and the original signal (blue, dashed) and to the setup dispersion corrected signal (red, solid). (d) z-Domain transmission OCT signal after inverse Fourier transform without dispersion correction (blue, dashed), after setup dispersion correction (black, points) and after material dispersion correction (red, solid).

is depicted in Fig. 2.4(c).

The parabolic shape is clearly visible and caused by the large values of $n_1 + n_2$ for fused silica glass and by the non-linearity of the spectrometer. The phase after spectrometer correction (red) has a lower maximum compared to the raw phase signal and shows a more pure parabolic phase behavior. The measured and compensated signal after the Fourier transformation is shown in Fig. 2.4(d), where the peak position represents the path length of the ballistic light. Due to dispersion, the measured transmission OCT signal (blue, dashed) is decreased and broadened compared to the dispersion compensated signal (red).

2.4.1. Refractive index and group velocity dispersion quantification for glasses and liquids

Figure 2.5 shows the dispersion results of four different glasses: BK7, fused silica, sapphire and calcium fluoride (CaF_2), and two liquids: water and ethanol. Figure 2.5(a) shows the results for the group refractive index for the different materials. The red bars denote the measured values using transmission OCT. It can be seen that the group refractive indices are close to the values from literature. BK7, fused silica and CaF_2 are slightly underestimated compared to the literature values, whereas for sapphire a relatively large underestimation of 3.2 percent is observed. Water has a slight overestimation of 0.56 percent and for ethanol the underestimation is 2.5 percent. The group velocity dispersion is shown in Fig. 2.5(b). It can be seen that the group velocity dispersion of all materials, except fused silica, are somewhat overestimated compared to the literature values. For fused silica the group velocity dispersion values are spread between the literature values.
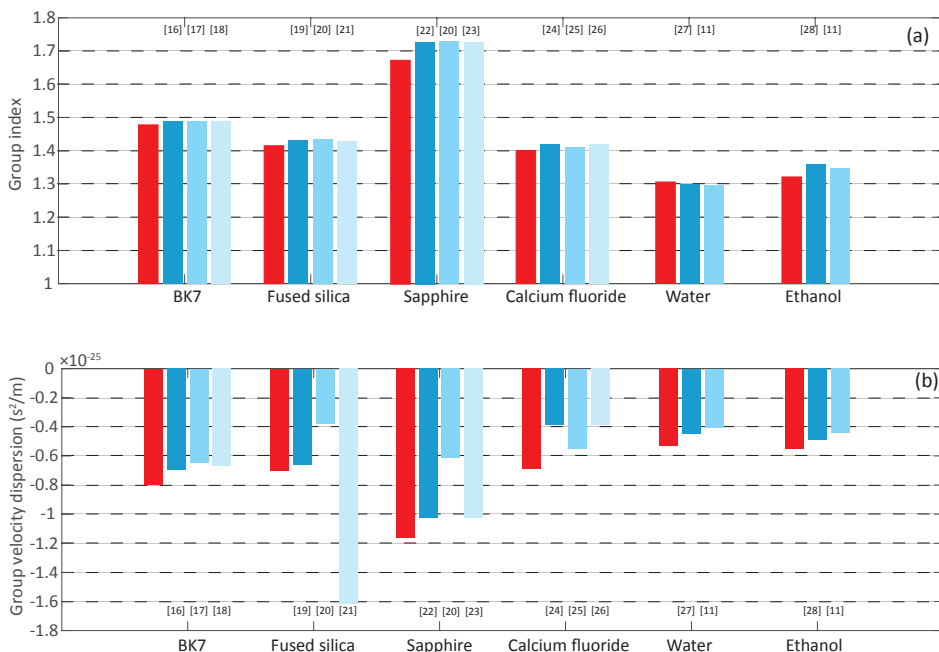

Figure 2.5: Measured group refractive index (a) and group velocity dispersion (b) compared with literature values. The measured values are denoted in red and the literature values are visualized in shades of blue with the reference indicated above and below their respective bar.

Aqueous solutions with different concentrations of glucose are measured to determine the optical properties of the constituent materials (as shown in Fig. 2.6). Both the group refractive index and the GVD follow a linear relation as would be expected from a volume-weighted average of the optical properties. The slope of $(1.21 \pm 0.02)10^{-3}$ group index change per volume percent results in a group refractive index of pure glucose of 1.465 ± 0.004, which agrees well with literature values [29, 30]. The slope of $(-2.05 \pm -0.04) \, 10^{-28} \, s^2/m$ GVD change per volume percent results in a GVD of pure glucose of $(-7.34 \pm 0.04) \, 10^{-26} \, s^2/m$.
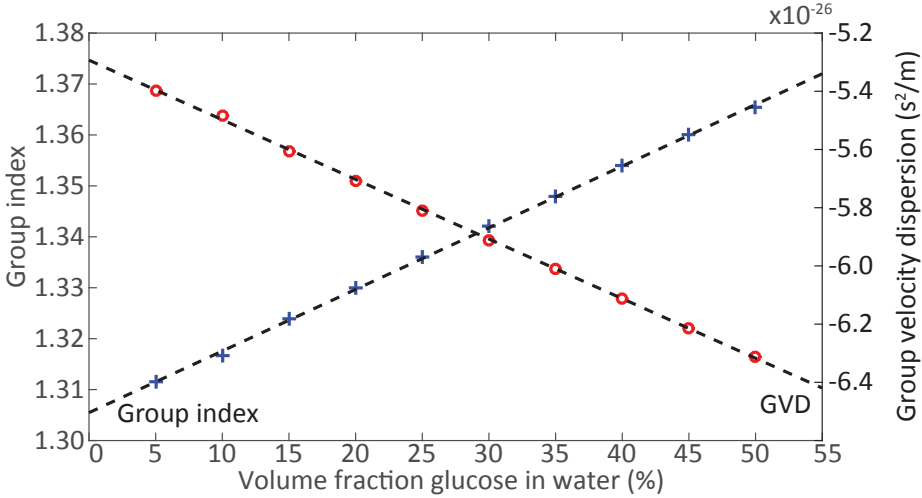
Figure 2.6: Group index and group velocity dispersion for solutions with varying glucose concentration as determined with transmission OCT. The measurements (indicated with open symbols, red and blue) are fitted with a linear regression (dashed black lines).

2.4.2. Attenuation and scattering measurements of silica particle suspensions

Transmission OCT measurements are performed for suspensions of silica particles in different concentrations. Two different particles sizes are considered; 0.5 μm and 1.5 μm diameter. Typical spatial domain data, averaged over 100000 measurements, for the 0.5 μm and 1.5 μm particles are shown in Fig. 2.7(a) and Fig. 2.7(b), respectively. For every concentration, peaks can be observed corresponding to ballistic light transmission. As the concentration of scatterers increases the peak amplitude decreases and the peak moves slightly to longer path lengths. In addition a decaying tail is observed behind the ballistic transmission peak of the 1.5 μm particle suspensions. This tail gradually becomes predominant as the concentration of scatterers increases and is caused by forward scat-

tered light transmitted through the sample. The 0.5 μm particles have a much lower scattering coefficient and scattering anisotropy and do not show the scattered light in the transmission OCT signal.
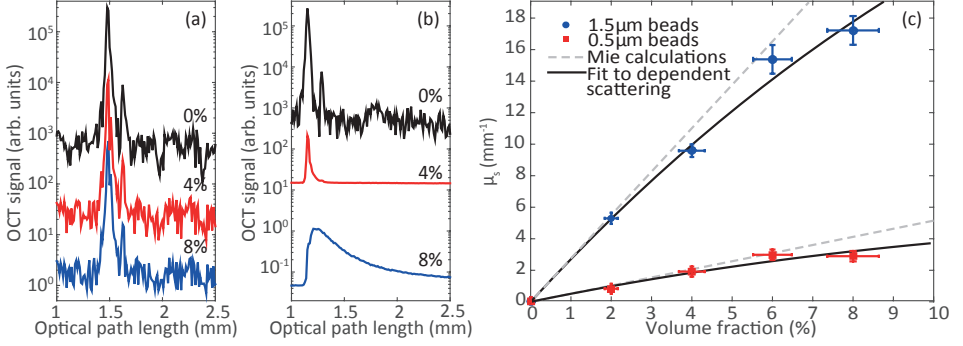
Figure 2.7: Spatial domain transmission OCT data for several concentrations of 0.5 μm (a) and 1.5 μm (b) silica particles in water. Data separated for plotting by multiplication with powers of 10. (c) Measured scattering coefficients for the silica suspensions. The data is fitted using a dependent scattering model (black, solid), which is based on Mie calculations (gray, dashed).

The measured scattering coefficient μ_s as function of the concentration for the 0.5 μm and 1.5 μm silica particle suspensions are shown in Fig. 2.7(c). For higher concentrations of particles in the suspension, more light is scattered resulting in an increase of the scattering coefficient. At very high concentrations the linear relation between scattering coefficient and particle concentration does not hold and the data is best described by a dependent scattering model. A fit of this model (Section 2.3.5) with the refractive index of the particles as the free parameter, results in $n_0 = 1.430 \pm 0.009$ for the 0.5 μm particles, and $n_0 = 1.444 \pm 0.005$ for the 1.5 μm particles. This value is close to the value of the phase refractive index of 1.447 for fused silica, reported by Malitson [19].The Hilbert transform method is used to determine the wavelength dependent attenuation coefficient for de-mineralised water and the 2 vol.% suspension of 1.5 μm particles. The measured absorption spectrum of water is shown in Fig. 2.8(a). The measured absorption coefficient agrees well with the data from Kedenburg et al. The wavelength dependent scattering coefficient for the silica particle suspension is shown in Fig. 2.8(b). Dependent scattering calculations are performed over the spectral range for comparison to the measured data. The measured data agree well with the calculated data. In both the water and the particle suspension data, deviations are observed at the edges of the measured attenuation spectra. At these wavelengths the source intensity is low resulting in small signals.
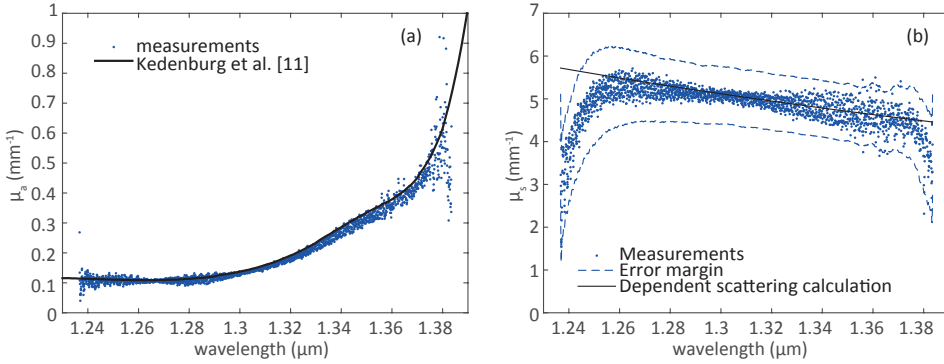
Figure 2.8: (a) Measured absorption coefficient of water versus wavelength (blue, dots) and its comparison to literature [11] (black, solid). (b) Measured scattering coefficient versus wavelength for 2 vol.% 1.5 μm silica particles (blue, dots). Error margin is denoted by the dashed lines. The data is compared to the scattering coefficient obtained from dependent scattering calculations (black, solid).

2.5. Discussion

We showed transmission OCT measurements of n_g, the GVD and the (wavelength resolved) attenuation coefficient. The measurements on glass plates, liquids and glass particle suspensions validated the proposed analysis technique.

The measurements of n_g showed good agreement with values found in literature. Some variation was present in the literature data, possibly caused by differences in the materials used. Our results are slightly less accurate compared to the refractive index measurement of Dirckx et al. [7] and Zvyagin et al. [6]. The GVD measurements, in general, agree well with literature values. Due to the large spread in values reported in literature, exact estimation of the accuracy of our method is difficult. For most measurements the obtained value for the GVD is within the variation represented in literature. We observed that the measured values of n_g and the GVD are very sensitive to variations in the spectrometer calibration. More accurate measurements can be obtained by improving the spectrometer calibration procedure. Increasing the bandwidth of the setup and the thickness of the samples could also provide more accurate results for n_g and GVD. We observed that the exact choice of the cropping factor affects our estimates of both n_g and GVD. The choice of 0.25 resulted in the most accurate estimation of both group velocity index and GVD. Measurement of n_g and the GVD for glucose solutions showed a clear linear behavior over the measured concentration range. By avoiding positioning errors and realignment of the cuvette, possible alignment errors are circumvented. Hence, the glucose measurements show that small differences in refractive index can be measured. The lowest glu-

cose concentration measurable is 0.39 vol. % and was estimated by a linear extrapolation of the slope and comparison to the error in the measurements. This concentration is still larger than typical blood glucose concentrations.

Determination of the attenuation coefficient is shown for both z-domain and spectral domain analysis. For both methods the main experimental difficulty proved to be the prevention of particle aggregation in the suspensions. The z-domain method works in principle up to 20 mean free paths (MFP) of attenuation. The technique is limited to scattering anisotropies up to approximately 0.9. Large anisotropy factors, as for example is the case for tissue, make the discrimination between ballistic and single scattered photons difficult. Increasing the spectral bandwidth results in a more narrow axial point spread function, which facilitates discrimination of ballistic light from scattered light. Additionally, information can be retrieved from the scattered light distribution, either by using a total attenuation coefficient or fitting a scattering model.

Wavelength resolved attenuation coefficients are computed from spectral domain data for water and 2 vol.% of the 1.5 μm particle suspension. The results show good agreement with literature and simulated data respectively. Deviations between measurements and literature are observed at the edges of the spectra. We attribute this to the low power of the light source at these wavelengths which makes it difficult to retrieve the envelope of the measured spectrum using the Hilbert transform. For a similar reason, measurements on samples with high attenuation coefficients (larger then approximately 10 MFP) fail to give accurate results. For highly attenuating samples short time Fourier transform techniques can be applied in combination with an analysis in the z-domain. This provides the benefit of path length discrimination, however, at the cost of reduced spectral resolution.

The measurements presented in this article demonstrate the potential of Fourier-domain transmission OCT as a powerful and versatile platform for measurements of optical properties. Transmission OCT does not rely on scattered light to perform a measurement, and therefore is not based on complicated light transport models or requires a homogeneous sample. In addition, coherence gating provides a means to filter or select scattered from the ballistic light from the measured signal. Application of the presented techniques can provide a way to optically characterize tissue in biopsies, aiding in the diagnostics of diseases. The multiple modes of contrast provided by our technique can provide a great advantage in this respect. In addition, transmission OCT can provide compact and cost effective measurements in microfluidics and lab-on-a-chip applications. With the onset of OCT on a chip technology this technique can provide a compact, versatile and relatively cheap way to measure optical properties. In addition, the proposed methods for determining n_g and the GVD also can be applied

in backscattering OCT, possibly providing additional (functional) tissue contrast. The measurements presented in this paper concern the characterization of the optical properties of a homogeneous bulk sample. The use of transmission OCT can be extended towards imaging spatially varying optical properties using computed tomography techniques.

2.6. Conclusion

In conclusion, we presented Fourier-domain transmission OCT as a method for measuring the group refractive index, the group velocity dispersion and the wavelength resolved attenuation coefficient of a wide range of samples. We validated the proposed methods using experimental data. The measurements are in good agreement with literature values and analytical theory. We showed that transmission OCT provides a powerful tool for measurements of various optical properties.

References

[1] G. Zaccanti, S. Del Bianco, and F. Martelli, "Measurements of optical properties of high-density media," Appl. Opt. vol. 42, no. 19, pp. 4023–4030 (2003).

[2] R. H. Bremmer, S. C. Kanick, N. Laan, A. Amelink, T. G. van Leeuwen, and M. C. Aalders, "Non-contact spectroscopic determination of large blood volume fractions in turbid media," Biomed. Opt. Express, vol. 2, no. 2, pp. 396–407 (2011).

[3] B. Aernouts, E. Zamora-Rojas, R. Van Beers, R. Watté, L. Wang, M. Tsuta, J. Lammertyn, and W. Saeys, "Supercontinuum laser based optical characterization of Intralipid® phantoms in the 500-2250 nm range," Opt. Express, vol. 21, no. 26, pp. 32450–32467 (2013).

[4] K. Barwari, D. M. de Bruin, E. C. Cauberg, D. J. Faber, T. G. van Leeuwen, H. Wijkstra, J. de la Rosette, and M. P. Laguna, "Advanced diagnostics in renal mass using optical coherence tomography: a preliminary report," J. Endourol., vol. 25, no. 2, pp. 311–315 (2011).

[5] N. Bosschaart, D. J. Faber, T. G. van Leeuwen, and M. C. Aalders, "In vivo low-coherence spectroscopic measurements of local hemoglobin absorption spectra in human skin," J. Biomed. Opt., vol. 16, no. 10, pp. 100504–100504 (2011).

[6] A. V. Zvyagin, K. K. Silva, S. A. Alexandrov, T. R. Hillman, J. J. Armstrong, T. Tsuzuki, and D. Sampson, "Refractive index tomography of turbid media by bifocal optical coherence refractometry," Opt. Express, vol. 11, no. 25, pp. 3503–3517 (2003).

[7] J. J. J. Dirckx, L. C. Kuypers, and W. F. Decraemer, "Refractive index of tissue measured with confocal microscopy," J. Biomed. Opt., vol. 10, no. 4, pp. 044014–044022 (2005).

[8] Z. Wang, K. Tangella, A. Balla, G. Popescu, "Tissue refractive index as marker of disease," J. Biomed. Opt., vol. 16, no. 11, pp. 116017-1160177 (2011).

[9] M. R. Hee, E. A. Swanson, J. A. Izatt, J. M. Jacobson, and J. G. Fujimoto, "Femtosecond transillumination optical coherence tomography," Opt. Lett., vol. 18, no. 12, pp. 950–952 (1993).

[10] V. D. Nguyen, D. J. Faber, E. van der Pol, T. G. van Leeuwen, and J. Kalkman, "Dependent and multiple scattering in transmission and backscattering optical coherence tomography," Opt. Express, vol. 21, no. 24, pp. 29145–29156 (2013).

[11] S. Kedenburg, M. Vieweg, T. Gissibl, and H. Giessen, "Linear refractive index and absorption measurements of nonlinear optical liquids in the visible and near-infrared spectral region," Opt. Mater. Express, vol. 2, no. 11, pp. 1588–1611 (2012).

[12] Y. Verma, P. Nandi, K. D. Rao, M. Sharma, and P. K. Gupta, "Use of common path phase sensitive spectral domain optical coherence tomography for refractive index measurements," Appl. Opt., vol. 50, no. 25, pp. E7–E12 (2011).

[13] A. F. Fercher, C. K. Hitzenberger, M. Sticker, R. Zawadzki, B. Karamata, and T. Lasser, "Numerical dispersion compensation for partial coherence interferometry and optical coherence tomography," Opt. Express, vol. 9, no. 12, pp. 610–615 (2001).

[14] N. Nassif, B. Cense, B. Park, M. Pierce, S. Yun, B. Bouma, G. J. Tearney, T. C. Chen, and J. F. de Boer, "In vivo high-resolution video-rate spectral-domain optical coherence tomography of the human retina and optic nerve," Opt. Express, vol. 12, no. 3, pp. 367–376 (2004).

[15] C. Mätzler, "MATLAB functions for Mie scattering and absorption, version 2," IAP Res. Rep., vol. 8 (2002).

[16] Schott, "Optical glass data sheets," (2012).

[17] Hikari, "Optical catalogue," (2015).

[18] Sumita, "Optical glass," (2015).

[19] I. H. Malitson, "Interspecimen comparison of the refractive index of fused silica," J. Opt. Soc. Am., vol. 55, no. 12 pp. 1205–1208 (1965).

[20] B. Tatian, "Fitting refractive-index data with the Sellmeier dispersion formula," Appl. Optics, vol. 23, no. 24, pp. 4477–4485 (1984).

[21] Heraeus, *Quartz Glass for Optics Data and Properties*(2015).

[22] I. H. Malitson, "Refraction and dispersion of synthetic sapphire," J. Opt. Soc. Am., vol. 52, no. 12, pp. 1377–1379 (1962).

[23] W. C. Tan, K. Koughia, J. Singh, and S. O. Kasap, "Fundamental optical properties of materials I," in *Optical Properties of Condensed Matter and Applications,* Jai Singh John Wiley and Sons, Ltd., Chichester, UK, (2006)

[24] H. H. Li, "Refractive index of alkaline earth halides and its wavelength and temperature derivatives," J. Phys. and Chem. Ref. Data, vol. 9, pp. 161–290 (1980).

[25] M. Daimon and A. Masumura, "High-accuracy measurements of the refractive index and its temperature coefficient of calcium fluoride in a wide wavelength range from 138 to 2326 nm," Appl. Opt., vol. 41, no. 25, pp. 5275–5281 (2002).

[26] I. H. Malitson, "A redetermination of some optical properties of calcium fluoride," Appl. Opt., vol. 2, no. 11, pp. 1103–1107 (1963).

[27] M. Daimon and A. Masumura, "Measurement of the refractive index of distilled water from the near-infrared region to the ultraviolet region," Appl. Opt., vol. 46, no. 18, pp. 3811–3820 (2007).

[28] J. Rheims, J. Köser, and T. Wriedt, "Refractive-index measurements in the near-IR using an Abbe refractometer," Meas. Sci. Technol., vol. 8, no. 6, pp. 601-606 (1997).

[29] W. M. Yunus and A. B. Rahman, "Refractive index of solutions at high concentrations," Appl. Opt., vol. 27, no. 16, pp. 3341–3343 (1988).

[30] S. R. Kachiraju and D. A. Gregory, "Determining the refractive index of liquids using a modified Michelson interferometer," Opt. Laser Technol., vol. 44, no. 8, pp. 2361–2365 (2012).

Chapter 3

Quantification of volume and optical parameters of zebrafish organs in optical coherence projection tomography images

Optical coherence projection tomography (OCPT) is a novel interferometric imaging modality for non-diffuse 3D optical imaging of millimeter-sized samples. OCPT allows quantitative reconstruction of refractive index and optical attenuation by coherence gating of scattered light. We demonstrate, on OCPT images, the segmentation of various organs of the zebrafish with manual, region growing, and k-means segmentation algorithms. For the segmented organs, the volume and the median optical properties of the zebrafish organs are determined. The optical properties are in good agreement with values from literature for similar tissue types.

3.1. Introduction

Optical coherence computed tomography (OCPT) is a novel imaging modality for non- diffusive 3D optical imaging of small animals [1]. OCPT imaging is based on transmission optical coherence tomography, where light from the sample arm of a Mach-Zehnder interferometer interferes with light propagating in the reference arm, as is presented in Chapter 2. The advantage of using tomographic transmission OCT is the combination of confocal gating and path-length selectivity (coherence gating), which allows a strong rejection of (multiple) scattered light. The imaging in transmission geometry and the fact that image formation is based on non-scattered light leads to a much greater imaging depth compared to conventional OCT. Upon interaction with the sample, the light in the sample arm can be delayed and attenuated due to scattering and absorption in the sample. From the attenuation and delay, the refractive index and optical attenuation coefficients can be determined quantitatively [2]. OCPT is applied to imaging of

an adult $3 - 4$ mm thick zebrafish from which both attenuation coefficient and refractive index contrast are reconstructed. We present the segmentation of various zebrafish organs from the refractive index and optical attenuation measurements and quantify their structural and optical parameters.

Various studies have demonstrated that the optical properties of different organs can indicate the health of the organ. Wang et al. [3] showed that cancer alters the refractive index, which can be used as a maker for cancer diagnostics. Xu et al. [4] differentiate different plaque components of coronary arteries using OCT. They distinguish three plaque types as fibrous, lipid and calcified based on their optical attenuation coefficient. Real time grading of bladder urothelial carcinoma using quantification of the OCT attenuation coefficient has been shown by Cauberg et al. [5] to verify the assessment of morphological changes. Segmentation of tissue structures in OCPT images of zebrafish can aid in visualizing these changes as well as quantifying them. This can potentially aid in the study of disease onset, progression, and treatment monitoring in zebrafish disease models.

Image segmentation is an image processing technique that highlights certain important parts of the image, such as objects or boundaries [6, 7]. There are many practical applications for image segmentation, such as locating tumors, surgery planning, and fingerprint recognition. Various methods have been developed for image segmentation ranging from simple thresholding, k-means clustering [8], and region-growing techniques [9] to more advanced techniques as graph cuts [10] and level sets [11]. Here, we apply image segmentation to analyze the anatomical structures of a zebrafish in OCPT images. We apply manual, region growing, and k-means segmentation to identify various individual structures. The segmentation of the organs is used to estimate their volume, median attenuation coefficient, and median refractive index.

3.2. Methods

3.2.1. Segmentation

The segmentation of the zebrafish organs is based on the assumption that neighboring pixels have similar attenuation coefficients or refractive index values. Since some structures are better visible in the attenuation coefficient image compared to the refractive image, or vice versa, all organs are segmented using the image modality with the best contrast. Moreover, a segmentation approach is used that gives the best result for the specific organ.

Region growing segmentation

For the lens of the zebrafish, imaged in refractive index contrast, we use a region growing algorithm, where one pixel is compared with its neighboring pixels. If

the pixel value of the refractive index is similar to that of its neighbors, this neigh-
boring pixel belongs to the region, otherwise not. The region growing algorithm
is initialized by a seed that is used as a starting position and image value. Fig-
ure 3.1 (a) shows a close up region that is segmented with a seed indicated in
blue. In Fig. 3.1 (b) a first iterations and expansion of the seed is shown. The
region grows iteratively by comparing all unallocated neighboring pixels and de-
termining whether they do or do not belong to the region based on whether their
value matches the mean value of the region. The application of the region grow-
ing on the zebrafish data is illustrated in Fig. 3.1 (c) and (d). Figure 3.1 (c) shows
a slice of the refractive index data of the zebrafish and Fig. 3.1 (d) is the segmen-
tation result, with the seed is placed in the center of the image.
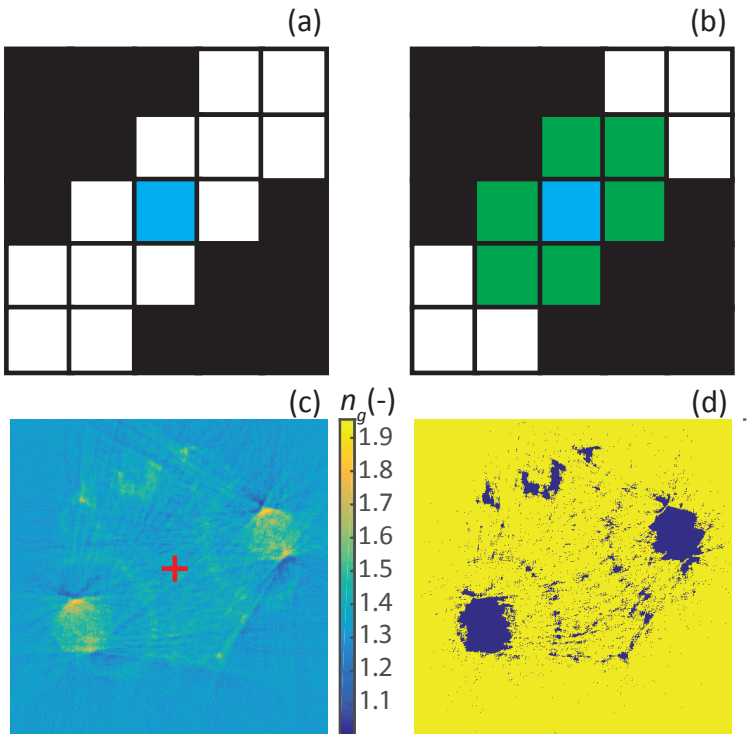

Figure 3.1: Illustration of the region growing algorithm. (a) Image in black and white, with the
seed point indicated in blue. (b) First step of the region growing (green) and starting seed (blue).
(c) Image of the refractive index data for a single slice of the zebrafish with seed point indicated.
(d) Segmented image using region growing. Yellow indicates the grown region.

k-means segmentation

For the spine segmentation, we implemented the *k*-means algorithm on the attenuation coefficient and refractive index images. The *k*-means algorithm originates from the field of machine learning and cluster analysis. Clustering methods, like *k*-means, are unsupervised and based on features in the image, such as the RGB colors or, for multi-model images, the various image parameters. Clustering methods group sets of objects which are more similar to each other compared to the other objects. Each cluster center is represented by a mean vector in feature space, which means that if the number of clusters are set to *k*, the task is to find the *k* cluster centers and the points are assigned to the nearest center. For finding the position of the cluster centers and the cluster boundaries, the distance between the each point in feature space and its assigned cluster center is calculated by the l_2 norm. An illustration of the *k*-means segmentation is shown in Fig. 3.2. Figure 3.2 (a) shows one slice of the refractive index data of the ze-

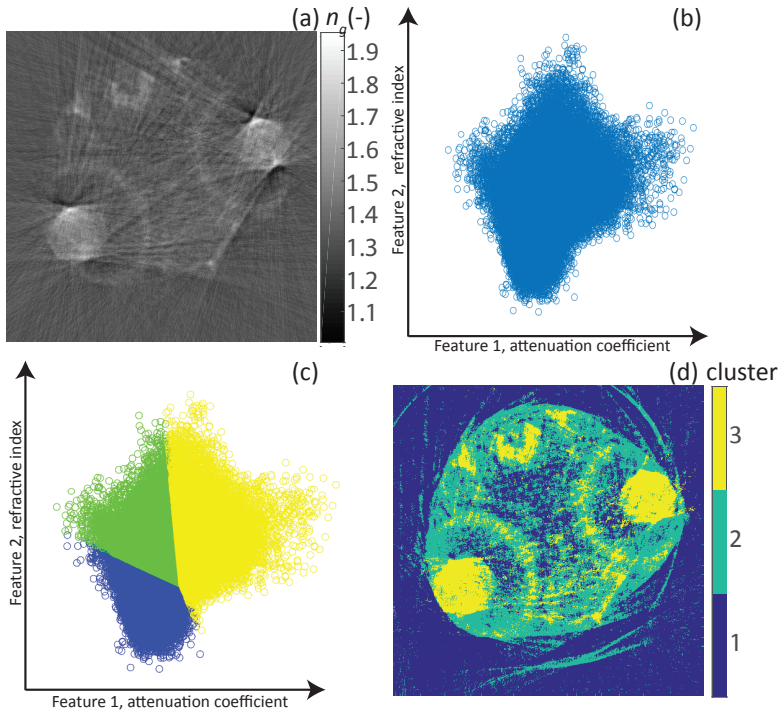Figure 3.2: K-means segmentation on one slice of the zebrafish. (a) Original gray scale image of the refractive index, (b) unclustered pixels of the zebrafish image in the feature space, where feature 1 denotes the attenuation coefficient, and feature 2 the refractive index. (c) Clustering result with three clusters is shown in blue, green and yellow and (d) segmentation of the zebrafish based on the three clusters indicated in (c).

brafish. All pixels in this slice of the refractive index and attenuation coefficient images are transformed into feature space, shown in Fig. 3.2 (b), where the value of every pixel is plotted on two scales: the value of its refractive index and attenuation coefficient. The corresponding clustering result is shown in Fig. 3.2 (c), where the number of k clusters is set to three and the different clusters are illustrated in different colors. After clustering, the pixels are back transformed to image space and the segmentation result of the k-means clustering with three different clusters is presented in Fig. 3.2 (d).

3.2.2. Data acquisition and tomographic reconstruction

Optical coherence computed tomography is used to image an adult zebrafish. A schematic representation of the OCPT data analysis and image reconstruction process is shown in Fig. 3.3. The experimental set-up and the pre-processing of the data are described in more detail in [1]. The wavelength used for the measurement is 1300 nm.

In brief, the signal processing is performed as follows. First, the interference
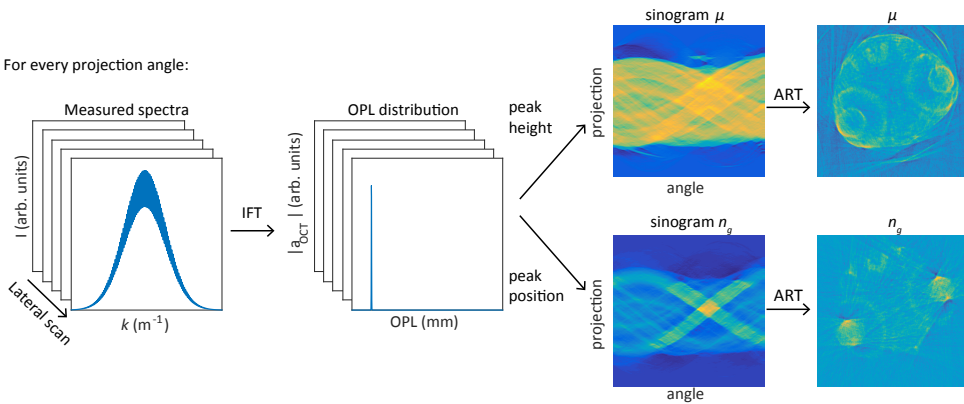
Figure 3.3: Schematic illustration of the OCPT data analysis and the image reconstruction process. Figure adjusted from [1].

spectrum at a single point of a projection is measured. Second, this spectrum is inverse Fourier transformed to obtain the optical path-length distribution. The signal from the ballistic light in the optical path-length distribution is extracted using a fitting procedure. The attenuation and the refractive index along the light path are estimated from the position and the height of the ballistic peak, respectively. The position of the ballistic peak is a measure for the integrated refractive index along the optical path through the sample and the height of the peak is a measure for the integrated attenuation value along the optical path through the sample. These two parameters are placed for each projection and each angle into

two separate sinograms. In this case, the zebrafish is measured over 180 angular projections with a sampling distance of 1°. The sinograms are corrected for center of rotation offsets. Afterwards, these two sinograms are reconstructed using an algebraic reconstruction technique using the ASTRA toolbox [12].

The refractive index and attenuation slices have a size of 501 × 501 pixels in the lateral direction, with 140 slices in the axial direction. The slices are recorded, uniformly spaced over a 2 mm axial range. Segmentation algorithms are applied to individual slices. Two slices of the zebrafish are shown in Fig. 3.4 for the attenuation coefficient and the refractive index. It can be noted, that different structures are visible in the two types of images.

Figure 3.4: Two OCPT transverse slices of the zebrafish head (top) and tail (bottom). (left) Attenuation coefficient image. (right) Group refractive index image.

3.2.3. Data processing

All tomographic reconstructions are performed on a computer with Intel(R) Xeon(R) CPU Processor (E5-1620 v3@3.50 GHz), 32 GB installed memory and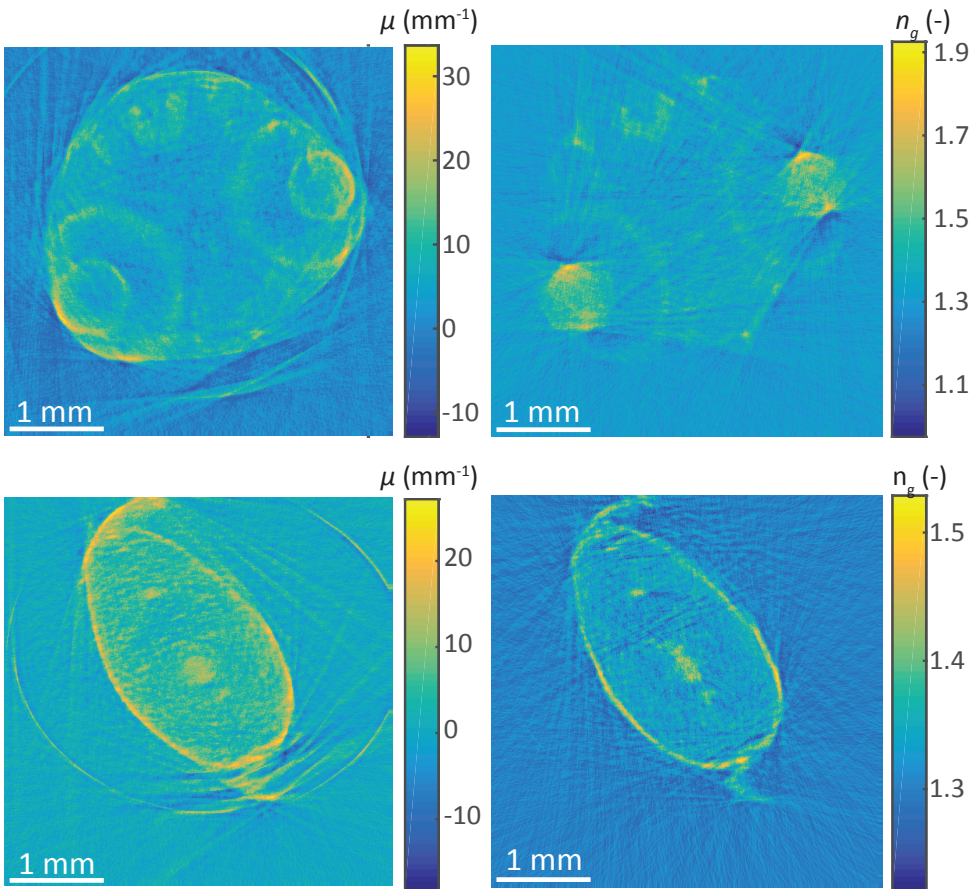 a 64-bit operating system. The data are processed using software written in the commercial software package MATLAB (Mathworks, R2016a). A region growing algorithm is used written by Dirk-Jan Kroon (University of Twente) and is publicly available at MathWorks file exchange [13]. For the k-means clustering the build-in MATLAB function *kmeans* is used, which has as input parameter the number of clusters. For the estimation of the median intensity values of the clusters, the MATLAB build-in function *median* was used. For the volume estimation, the areas are determined by the function *regionprops* with the additional property *Area*. All the areas, estimated in number of pixel, are summed for all slices and then multiplied by the voxel volume of 8908.8 μm^3 to calculate the segmented volume. The manual segmentation is performed using the MATLAB function *imfreehand*.

3.3. Results

We investigate the segmentation and optical properties of the zebrafish measured with optical coherence computed tomography. Various organs are segmented using basic thresholding, automated segmentation, and manual segmentation.

The zebrafish spine, although being quite inhomogeneous, is best visualized in the attenuation coefficient image. The segmentation of the spine is performed in multiple steps on a slice by slice basis. First, the noise in the image is reduced using an averaging filter with a size of 11×11 pixels. Second, the k-means clustering algorithm is applied to the combined refractive index and attenuation coefficient images. The number of clusters is set to 3 and the distance measure is set to *Euclidean*. Third, the number of clusters is reduced to two, whereby a binary image is generated, by combining two clusters. Fourth, a morphological opening, an erosion operation is followed by a dilation operation using disks of 10 pixels, is applied to the binary image to erase the segmentation of very small objects, which are caused by noise or other artifacts. Since the initial application of the k-means algorithm leads to the segmentation of multiple objects, the circularly shaped spine is selected by further processing the image using a Hough transform, whereby the MATLAB function *circle_hough* is used. The Hough transform estimates the radius and center position of all objects, from which the spine is subsequently selected. For those slices in which the Hough transform is not able to detect the spine or no spline is visible, the spine is estimated using linear interpolation between the detected spine in neighboring slices. A visualization of the spine segmentation is shown in Fig. 3.5.
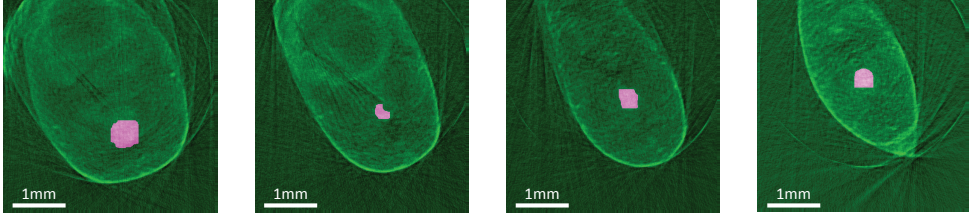
Figure 3.5: Segmentation (magenta) of the zebrafish spine in four transverse OCPT slices overlaid on the scaled attenuation image(green) of an adult zebrafish.

It can be observed that the zebrafish eye lens is well visualized in the refractive index OCPT image, see Fig. 3.4, on which we perform the segmentation. The seed-point for the region growing algorithm is positioned in the center of the image, where no lens is located. The maximum intensity distance is chosen by hand and set to 0.1, which segments everything except the lens of the zebrafish eye. To obtain the lens segmentation shown in Fig. 3.6, the complement of the image is calculated, using the in-build MATLAB function *imcomplement*.
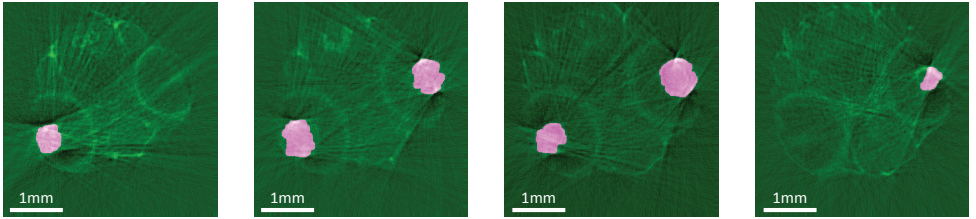
Figure 3.6: Overlay of the scaled refractive index data (green) and the segmentation (magenta) of the lens of an adult zebrafish eye at four different transverse OCPT slices.

Due to the noise in the attenuation and refractive index OCPT reconstructions and the low contrast with the surrounding tissue, the brain matter is segmented by hand on the refractive index data. The manual segmentation is aided by comparison to annotated zebrafish anatomy [14].

The swim bladder is most optimally segmented using thresholding on refractive index data with a threshold value of $n = 1.3$, which is between the refractive index of air (n=1) and that of tissue $n > 1.35$.

The skin is segmented on attenuation data and for the segmentation a threshold of 5 is used. Afterwards, a morphological opening is applied to remove noise and holes in the segmentation. The segmentation result for all segmented organs on both the attenuation and refractive index are illustrated in one 3D figure and shown in Fig. 3.7.
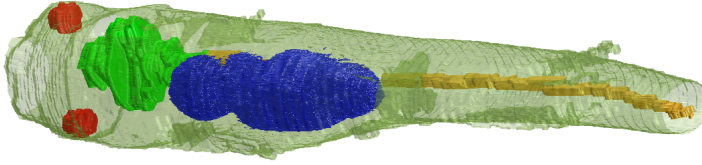
Figure 3.7: Segmentation of multiple organs in an OCPT image of an adult zebrafish. Red: lenses, green: brain, blue: gas bladder, yellow: spine and transparent green: skin.

3.3.1. Optical properties of segmented zebrafish organs

As shown in Chapter 2, the attenuation and refractive index can be obtained quantitatively from the transmission OCT signal. In the tomographic OCPT reconstruction these properties are imaged quantitatively and spatially resolved. With the image segmentation described here, it is possible to estimate the volume and median values for the optical properties of the segemented organs inside the zebrafish. We expect that the organs have homogeneous tissue values, however due to diffraction and refractive index differences between the fish and the agarose, organs such the lenses are not entirely homogeneously.

In Table 3.1 the volume, median attenuation coefficient, and median refractive index values of the different segmented organs are shown. The attenuation and refractive index values are, if available, compared with literature values of similar tissue types.

The segmented brain is a mixture of gray and white matter and other structures in the brain, hence, the average attenuation coefficient is expected to be the weighted average of literature values of gray matter, white matter, and thalamus. Although, the literature values of the attenuation coefficient for the brain tissue where given for a wavelength of 1100 nm, however, the variation in attenuation

Table 3.1: Volume (V), attenuation (μ_t) and refractive index (n) values of various adult zebrafish organs. Gray matter is denoted as gm, white matter as wm and thalamus as thala.

Organ	V (µl)	μ_t (mm^{-1})	Lit. value μ_t	n_g	Lit. value n_g
Brain	1.95	6.48	gm: 5 ± 3 [15] wm: 10 ± 2 [15] thala: 8 ± 3 [15]	1.39	1.41 ± 0.02 [16]
Lenses	0.24	7.84	7 to 9 [17]	1.64	1.55 ± 0.02 [18]
Spine	1.48	8.34	spinal fluid 5 ± 0.7 [15]	1.45	
Gas bladder	8.95	3	0	0.99	1 [19]

coefficient is expected to be small compared to 1300 nm [15]. The attenuation coefficient of the lens is in good agreement with the literature value taken from [17]. The spine includes spinal fluid and bone. However, we only found a literature value of the attenuation value of the spinal fluid at 1300 nm, which is slightly higher compared to the attenuation value of the entire spine that we estimated from the segmented part of the zebrafish. In the gas bladder, we expect an attenuation of air, which is 0 mm^{-1}. The difference, of the measured attenuation coefficient of air and the literature, is attributed to high attenuation values, which are incorrectly back projected. This leads to inhomogeneous attenuation coefficient values in the segmented area and hence also lead to higher values. Overall, we can note that the median attenuation values of the various organs estimated from the OCPT images are in a good agreement with the literature values.

The refractive index values of the different organs are in agreement as the segmented organs are close to the literature values. The literature value of the refractive index for the lens [18] is measured at 800 nm wavelength. Considering typical dispersive properties of tissue we expect this wavelength dependence to only give deviations of the order of $\Delta n \approx 0.03$ for a wavelength of 800 nm compared to the measured value at 1300 nm [20].

3.4. Discussion

We demonstrate the segmentation of various zebrafish organs using multi-contrast data measured with OCPT. Furthermore, we indicate that the volume, refractive index, and attenuation measurements can be quantitatively determined for individual organs inside the zebrafish.

For the region growing algorithm, we observed that the choice of the position of the seed is important for the obtained segmentation result. We choose the best position by trial and error to obtain the optimal result. Region growing algorithms have the disadvantages that they are computationally expensive. Depending on the maximum intensity distance, the time to segment a single slice can vary. For the chosen maximum intensity distance of 0.1 the estimation time is 22 seconds for one slice. In addition, it is a local and not a global segmentation method, since the segmentation starts from the seed and hence is biased to segment structures close to the seed. Furthermore, the region growing method is sensitive to noise. The advantage of this method is its conceptual simplicity and the fact that even one seed points is able to represent the segmentation of the object of interest. The k-means clustering is easy to implement, to understand and to interpret. It works on the single slice and is not dependent on the bias of a seed position. However, the method is sensitive to cluster outliers and the correct choice of the parameter k is important in order to segment the desired objects. The time to perform the clustering for one slice takes only 2 seconds.

Segmentation results can potentially be improved by using more advanced segmentation methods, such as graph cuts [10] and level sets [11]. Methods like graph cuts are less sensitive to noise and prior information could be included. Further improvements, could also be achieved by using three dimensional segmentation methods, thereby the three dimensional structure of the organ is included.

All segmented organs have different combinations of attenuation coefficients and refractive index, which makes it possible to use the modality in which the organ has the highest contrast to segment these organs. Moreover, from the quantitative determination of the optical properties using segmentation it may be possible to detect changes of the organs. For example, a comparison of optical properties can be useful for disease diagnosis and the study of the mechanisms of disease onset [21]. With OCPT and the presented segmentation method, changes in zebrafish organ attenuation coefficient and refractive index can be performed quantitatively. This enables the study of the optical properties of similar organs in zebrafish that are healthy and affected by disease to study disease onset, progression, and treatment monitoring in great detail.

3.5. Conclusion

In this paper, we segment various organs of a zebrafish measured with optical coherence projection tomography. With image segmentation techniques, it is possible to determine the volume, attenuation coefficient, and refractive index of various zebrafish organs quantitatively. The attenuation coefficient and refractive index of the various organs are in good agreement with literature values.

References

[1] J. van der Horst, A. K. Trull, and J. Kalkman, "Deep tissue label-free quantitative optical tomography," manuscript in preparation.

[2] A. K. Trull, J. van der Horst, J. G. Bijster, and J. Kalkman, "Transmission optical coherence tomography based measurement of optical material properties," Opt. Express, vol. 23, no. 26, pp. 33550–33563 (2015).

[3] Z. Wang, K. Tangella, A. Balla, and G. Popescu, "Tissue refractive index as marker of disease," J. Biomed. Opt., vol. 16, no. 11, pp. 116017-116024 (2011).

[4] C. Xu, J. M. Schmitt, S. G. Carlier, and R. Virmani, "Characterization of atherosclerosis plaques by measuring both backscattering and attenuation coefficients in optical coherence tomography," J. Biomed. Opt., vol. 13, no. 3, pp. 340031–340038 (2008).

[5] E. C. Cauberg, D. M. de Bruin, D. J. Faber, T. M. de Reijke, M. Visser, J. J. de la Rosette, and T. G. van Leeuwen, "Quantitative measurement of attenuation coefficients of bladder biopsies using optical coherence tomography for grading urothelial carcinoma of the bladder," J. Biomed. Opt., vol. 15, no. 6, pp. 660131–6660136 (2010).

[6] L. G. Shapiro and G. C. Stockman, *Computer vision,* Prentice-Hall (2001).

[7] L. Barghout and W. L. Lawrence, "Perceptual information processing system," Paravue Inc. U.S. Patent Application 10/618, patent number US20040059754A1 (2003).

[8] J. B. MacQueen, "Some methods for classification and analysis of multivariate observations," Proceedings of 5th Berkeley Symposium on Mathematical Statistics and Probability, pp. 281–297 (2011).

[9] R. C. Gonzalez and R. Woods, *Digital Image Processing 2nd Edition*, Prentice Hall (2002).

[10] Y. Boykov and G. Funka-Lea, "Graph cuts and efficient N-D image segmentation," International Journal of Computer Vision, vol. 20, no. 2, pp. 109–131 (2006).

[11] A. Tsai, A. Yezzi, W. Wells, C. Tempany, D. Tucker, A. Fan, W. Grimson, and A. Willsky, "A shape-based approach to the segmentation of medical imagery using level sets," IEEE Trans. Med. Imaging, vol. 22, no. 2, pp. 137–154 (2003).

[12] W. van Aarle, W. J. Palenstijn, J. D. Beenhouwer, T. Altantzis, S. Bals, K. J. Batenburg, and J. Sijbers, "The ASTRA toolbox: a platform for advanced algorithm development in electron tomography," Ultramicroscopy, vol. 147, pp. 35–47 (2015).

[13] D.-J. Kroon, "Region growing," File Exchange Mathworks https://nl.mathworks.com/matlabcentral/fileexchange/19084–region–growing (2008).

[14] D. Salgado, C. Marcelle, P. D. Currie, and R. J. Bryson-Richardson, "The zebrafish anatomy portal: a novel integrated resource to facilitate zebrafish research," *Developmental Biology*, vol. 372, no. 1, pp. 1–4, (2012).

[15] V. Tuchin, *Tissue optics: Light scattering methods and instruments for medical diagnosis,* SPIE Press, (2007).

[16] J. Sun, S. J. Lee, L. Wu, M. Sarntinoranont, and H. Xie, "Refractive index measurement of acute rat brain tissue slices using optical coherence tomography," Opt. Express, vol. 20, no. 2, pp. 1084–1095 (2012).

[17] R. L. Vincelette, A. J. Welch, R. J. Thomas, B. Rockwell, and D. J. Lund, "Thermal lensing in ocular media exposed to continuous-wave near-infrared radiation: The 1150-1350-nm region," J. Biomed. Opt., vol. 13, no. 5, pp. 054005-1 - 05405-10, (2008).

[18] L. Garner, G. Smith, S. Yao, and R. Augusteyn, "Gradient refractive index of the crystalline lens of the black oreo dory (allocyttus niger): comparison of magnetic resonance imaging (MRI) and laser ray-trace methods," Vision Research, vol. 41, no. 8, pp. 973 - 979 (2001).

[19] P. Ciddor, "Refractive index of air: new equations for the visible and near infrared," Appl. Opt., vol. 35, no. 9, pp. 1566–1573 (1996).

[20] H. Ding, J. Q. Lu, W. A. Wooden, P. J. Kragel, and X.-H. Hu, "Refractive indices of human skin tissues at eight wavelengths and estimated dispersion relations between 300 and 1600 nm," Phys. Med. Biol., vol. 51, no. 16, pp. 1479–89 (2005).

[21] V. Backman, M. B. Wallace, L. T. Perelman, J. T. Arendt, R. Gurjar, M. G. Muller, Q. Zhang, G. Zonios, E. Kline, J. A. McGilligan, S. Shapshay, T. Valdez, K. Badizadegan, J. M. Crawford, M. Fitzmaurice, S. Kabani, H. S. Levin, M. Seiler, R. R. Dasari, I. Itzkan, J. Dam, and M. S. Feld, "Detection of preinvasive cancer cells," Nature, vol. 406, pp. 35–36 (2000).

Chapter 4

Point spread function based image reconstruction in optical projection tomography

As a result of the shallow depth of focus of the optical imaging system, the use of standard filtered back projection in optical projection tomography causes space-variant tangential blurring that increases with the distance to the rotation axis. We present a novel optical tomographic image reconstruction technique that incorporates the point spread function (PSF) of the imaging lens in an iterative reconstruction. The technique is demonstrated using numerical simulations, tested on experimental optical projection tomography data of single fluorescent beads, and applied to high-resolution emission optical projection tomography imaging of an entire zebrafish larva. Compared to filtered back projection our results show greatly reduced radial and tangential blurring over the entire 5.2×5.2 mm^2 field of view, and a significantly improved signal to noise ratio.

4.1. Introduction

Optical tomographic imaging techniques such as optical diffraction tomography [1] and optical projection tomography (OPT) [2] are now among the standard imaging modalities for the study of cells, tissues and small animals. In OPT, light intensity projections of samples, such as zebrafish or (mouse) embryos, are measured in transmission or emission (fluorescence). From these projections, images are computed using tomographic reconstruction algorithms. OPT is used for in-vivo and ex-vivo imaging, whereby for ex-vivo imaging optical clearing techniques are used to suppress light scattering.

In the quest for improved image resolution, high numerical aperture (NA) lenses are used to image the transmission or emission of the sample onto the

detector. However, high NA lenses have a small depth of focus (DOF), which causes light that is emitted or absorbed outside of the focal region to be heavily blurred in the detector plane, thereby limiting the imaging depth. Moreover, standard reconstruction techniques, such as filtered back projection (FBP), are generally based on a straight ray approximation and ignore the diffraction of the light by the focusing lens. As a result, reconstructed OPT images can suffer from severe image degradation, leading to tangential blurring that increases with the distance to the rotation axis in the reconstructed image.

Hardware-based approaches to solve the depth of focus effect are either based on off-center focusing [3] or scanning the focal plane through the sample [4]. Although, these techniques can reduce the depth of focus effect in the reconstructed image, they are complex to apply and increase the acquisition time.

A sinogram filtering using the frequency distance relationship (FDR) was developed by [5], in which a space-variant inverse filter is applied to process the sinogram in Fourier space. The physical PSF of an optical imaging system was used as a filter in the FDR reconstruction of OPT data by [6]. In this method the image is reconstructed, after filtering the sinogram, using standard FBP. A weighted FBP for quantitative fluorescence optical projection tomography was presented by [7]. They used a space-variant weighting in the FBP reconstruction to correct for defocus related blur and isotropic emission of the fluorophores. However, this filter was only applied in one direction, which resulted in an increased radial full width at half maximum of the point spread function (PSF). To reduce the effect of the DOF both the radial and tangential direction, various processing methods were developed, which include the physical PSF in their approach. Deconvolution techniques with a space-variant PSF have been applied to the reconstructed image [8–10]. However, the quality of this technique depends on the choice of many parameters of the applied reconstruction algorithm. Furthermore, deconvolution techniques have the disadvantage to amplify noise. To our knowledge, the PSF has been used for reconstruction in terahertz tomography and in medical tomographic techniques, such as terahertz tomography [11], PET [12], SPECT [13] and CT [14]. [11] presented an iterative approach, where the object is reconstructed with the straight ray inverse Radon transform and subsequently deconvolved with a Gaussian PSF. For SPECT imaging, the system response was taking into account in an iterative conjugate gradient reconstruction method by [13]. They showed that the inclusion of the PSF gives improved resolution compared to FBP. An iterative 3D edge-deblurring algorithm for cone-beam CT was proposed by [14]. The PSF was first approximated by a least-squared approach and then used for a three dimensions deconvolution. However, the image size used by both [13, 14] was significantly smaller than the current image size used for OPT.

We present a PSF-based optical tomographic image reconstruction approach, in which the PSF of the focusing by the lens is directly included in the tomographic reconstruction, instead of filtering the sinogram before or the image after the reconstruction. First, a theoretical framework is provided that describes the PSF-based reconstruction. The application of the theory is demonstrated using numerical simulations of the tomographic imaging process. Second, our algorithm is tested under well-controlled experimental conditions. Finally, the technique is demonstrated on zebrafish larva imaging.

4.2. Image formation in optical projection tomography

In optical projection tomography (OPT), the goal is to determine the spatial distribution of absorption or emission strength of an object $f(x, y, z)$ from its projections. In emission OPT, the object is assumed to be homogeneously illuminated with light from the excitation source resulting in an excitation rate that is constant over the object f. A small fraction of the excitation light is absorbed and emitted isotropically. Hence, it is assumed that variations in local emission strength are caused by variations in fluorophore concentration only. The emitted radiation is imaged with an imaging system onto the detector, see Fig. 4.1(a).

Following [15], and assuming a single emitter at location x, y, z, in the object coordinate system, the intensity in the image space coordinate system is $I(s, t, u) = |h(x + Ms, y + Mt, z - M^2 u)|^2$, with h^2 the incoherent PSF and M the magnification of the imaging system. Given the geometry in Fig. 4.1 (a) with the detector fixed at $u = 0$ and since the object can be considered as a sum of incoherent point sources, the measured intensity is a convolution of the object emission distribution with the PSF $|h(x, y, z)|^2$. For an imaging system with $M = -1$ and $u = 0$ the measured intensity on the detector is

$$I(s, t) = \iint\limits_{-\infty}^{\infty} f(x - s, y - t, z - u)|h(x, y, z)|^2 \, \mathrm{d}x \, \mathrm{d}y \, \mathrm{d}z|_{u=0}. \qquad (4.1)$$

In the absence of diffraction, the PSF is $|h(x, y, z)|^2 = \delta(x, y)$. Under these circumstances the convolution in Eq. 4.1 results in a line integral of the object $f(x, y, z)$, similar to the Radon transform at zero angle along the propagation direction [16]. In OPT, diffraction causes the PSF to be non-ideal. The emitted light, originating along a straight path through the object, is (unsharply) imaged by a lens onto the detector. The shape of the 3D PSF can be calculated by Fourier optics, more in particular by Fresnel propagation of the emitted field through the lens onto the detector [15, 17].

Following the derivation by van der Horst et al. [8] we assume an integration on the detector in the t direction over the entire detector plane, which is a good
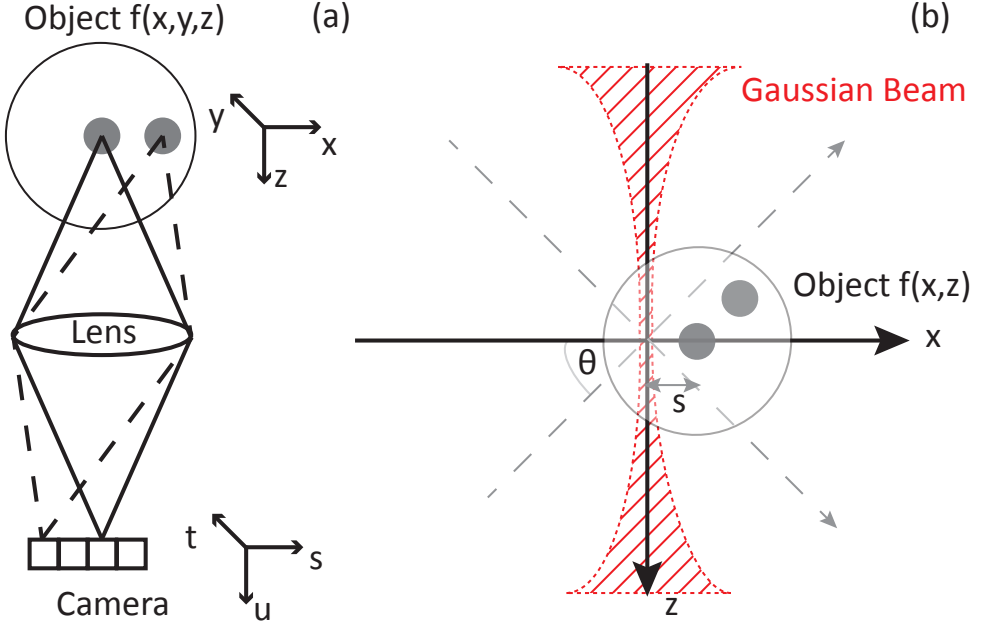
Figure 4.1: Schematic overview of the optical project tomography imaging system. (a) Optical imaging system consisting of a single lens making a projection of the object onto the camera. (b) OPT signal formation for diffractive optical beams (red dashed and hatched). The rotation angle is denoted by θ, the shift of the object s, and $f(x,z)$ is a slice of the object.

approximation for objects that have optical properties that vary slowly along the y-axis. In this case the measured intensity in Eq. 4.1 becomes proportional to the convolution of the object with a 2-D cross-section of the 3-D PSF. Since the image of a point emitter by a lens results in a complex PSF, we describe it here through an analytical formula. In this way we can quantitatively validate our approach using simulations and compare our results with theory. We model the PSF $|h(x,z)|^2$ as a Gaussian-shaped beam of the wavelength λ and in focus beam waist w_0 [18] as

$$|h(x,z)|^2 = \left| \frac{1}{\sqrt{1 + \left(\frac{z}{z_R}\right)^2}} \exp\left(-\frac{x^2}{w_0^2 \left(1 + \left(\frac{z}{z_R}\right)^2\right)} \right) \right|^2, \qquad (4.2)$$

where $z_R = \pi w_0^2 / \lambda$ is the Rayleigh range (half the depth of focus). The numerical aperture is given by NA $= w_0/z_R$ in Eq. 4.1. The two-dimensional convolution of the PSF over the object is indicated in Fig. 4.1(b).

In tomographic imaging, we obtain the projections of the emission as a func-

tion of the lateral shift s and the rotation angle θ of the object. From Eq. 4.1, it can be derived that the measured projection at the angle θ and shift s is

$$p(s,\theta) = \iint\limits_{-\infty}^{\infty} f[(x-s)\cos\theta + z\sin\theta, (x-s)\sin\theta - z\cos\theta]\, |h(x,z)|^2\, \mathrm{d}x\,\mathrm{d}z, \quad (4.3)$$

with the angle $\theta \in [0, 2\pi]$. The projections $p(s,\theta)$ are commonly visualized in a sinogram, where the convolution in Eq. 4.3 describes the blurring in the sinogram due to the tomographic imaging system.

The projection data $p(s,\theta)$ is not measured in a continuous way, as defined by Eq. 4.3, but is sampled at discrete lateral positions for a finite set of angles. Hence, the inverse solution cannot be determined analytically, but only through a search for the function $f(x,z)$ that optimizes an objective function. The projection of Eq. 4.3, $p(s,\theta)$, is limited to a finite integration area D given by $D \in [-l/2, l/2]$ for offsets $s \in [-l/2, l/2]$ and l is the size of the field of view. The projection is then represented by a matrix multiplication with the object f discretized by sampling $f(x,z)$ on a regular cell-centered grid, within the square object domain D^2 at locations x_i, z_j, with $i = 1, 2, \dots, n$, $j = 1, 2, \dots, n$ where n is the number of pixels in each direction of the object and equal to the number of lateral pixels in the projection. This leads to an image matrix of $f(x_i, z_i) \in \mathbb{R}^{n \times n}$, which is stacked in a vector $\mathbf{f} \in \mathbb{R}^{n^2}$. The convolution of Eq. 4.3 is discretized into a geometry matrix $\mathbf{A} \in \mathbb{R}^{m \times n, n^2}$, with m the number of projection angles. A row of the matrix $\mathbf{A}$ represents a the Gaussian PSF at lateral distance s_i and angle θ_k. The matrix elements of $\mathbf{A}$ are

$$a_{(k-1)n+i,:} = |h[(x_i - s_i)\cos\theta_k + z_i\sin\theta_k, (x_i - s_i)\cos\theta_k - z_i\sin\theta_k]|^2. \quad (4.4)$$

In this way, a shifted and rotated PSF is represented in a single row of the $\mathbf{A}$ matrix. First, all shifts for one angle are addressed, which is subsequently repeated for all angles. The acquisition domain of the measured projections are the set of samples (s_i, θ_k), with $k = 1, 2, \dots, m$. The discrete projections $p(s_i, \theta_k) \in \mathbb{R}^{n,m}$ are stacked into a vector $\mathbf{p} \in \mathbb{R}^{n \cdot m, 1}$.

After discretization, the object, $\mathbf{f}$, can be reconstructed by finding a solution to the optimization problem

$$\underset{\mathbf{f}}{\arg\min} \quad \frac{1}{2}\|\mathbf{A}\cdot\mathbf{f} - \mathbf{p}\|_2^2, \quad (4.5)$$

where $\|\cdot\|_2$ denotes the Euclidean norm. Equation 4.5 can be solved using a least squares optimization method based on conjugate gradients.

4.3. Image reconstruction

Tomographic reconstructions are performed on a computer with Intel(R) Xeon(R) CPU Processor (E5-1620 v3@3.50 GHz), 32 GB installed memory and a 64-bit operating system. The data are processed using software written in the commercial software package MATLAB (Mathworks, R2016a). Simulated sinograms are constructed using the discretized version of Eq. 4.3 for an initial object f. Following the data processing flow chart in Fig. 4.2, an initial guess of the image is created by filtered back projection (FBP) (input reconstruction). An improved estimate for the object is made by least-squares optimization of Eq. 4.5 using the MATLAB function *lsqr* [19, 20], which uses a conjugate-gradient type iterative algorithm on the normal equations. It takes as input the projection data, the initial guess of the image (created by FBP), the maximum number of iterations to perform is set to 4000, the absolute tolerance, and the geometry matrix **A**. The absolute tolerance of the method is chosen to be 10^{-6}. If the algorithm stops at the maximum number of iterations before the absolute tolerance is reached, the reconstruction results are evaluated by visual inspection. The PSF-based reconstruction is performed without including any prior information or regularization in the optimization of Eq. 4.5.

The geometry matrix **A** is non-sparse and therefore explicitly computing and storing it for a realistic image size of 1000 by 1000 would require around 8 terabytes of memory, which is infeasible. Instead of requiring a precomputed version of **A**, the MATLAB function *lsqr* also allows providing a routine that evaluates multiplication by **A** and its transpose for every angle individually. Here, multiplication by **A** corresponds to (PSF-based) forward projection of an input image, and multiplication by the transpose of **A** corresponds to (PSF-based) back projection of an input sinogram. We list the pseudo-code for calculating the forward and backward projection in Algorithm 1. It uses the built-in MATLAB function *imrotate* with bilinear interpolation to obtain the object at different angles. For every individual angle, the PSF is translated laterally over the sample, so the forward model of the projection has the structure of a one-dimensional convolution in the translation direction, followed by a sum in the direction orthogonal to that. We implement this by a multiplication of the Fourier transform of the object and the Fourier transform of the PSF for every column, followed by a sum for every row. To perform these operation correctly we zero-pad the sinogram to twice its size in the scanning direction. The back projection operator performs the adjoint/transpose variants of these steps in reverse order.

We set the maximum number of *lsqr* iterations to different hand-picked numbers depending on the convergence of the algorithm, which depends on the data that is to be reconstructed. In the current implementation one iteration of the *lsqr* algorithm, for one slice of 1000 by 1000 pixels, takes approximately two min-

utes.
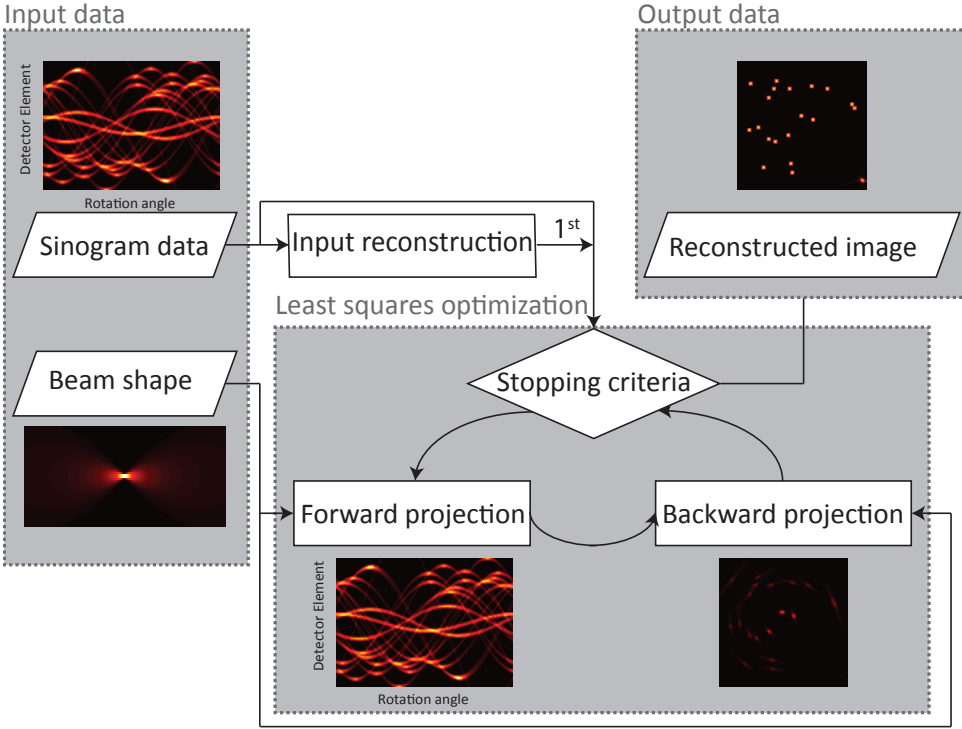
Figure 4.2: Schematic illustration of the data analysis algorithm for the PSF-based reconstruction. The input reconstruction is only used in the first iteration.

To enable a qualitative comparison of the reconstructed images, the FBP reconstruction is scaled in the following way. The reconstructed FBP image is forward projected to obtain its sinogram. The scaling factor α_{opt} is then given by

$$\alpha_{\mathrm{opt}} = \underset{\alpha}{\operatorname{argmin}} \quad \|\alpha \mathbf{A} \mathbf{f}_1 - \mathbf{A} \mathbf{f}_2\|_2^2, \tag{4.6}$$

where $\mathbf{f_1}$ is the FBP reconstructed image and $\mathbf{f_2}$ the PSF-based reconstructed image. The scaling factor α_{opt} is then given in closed-form by

$$\alpha_{\mathrm{opt}} = \frac{(\mathbf{A}\mathbf{f}_1)^{\mathrm{T}}(\mathbf{A}\mathbf{f}_2)}{\|\mathbf{A}\mathbf{f}_1\|_2^2}. \tag{4.7}$$

Subsequently, the FBP reconstruction is scaled with α_{opt} to obtain an image intensity distribution in the reconstruction that corresponds to equal projection data.

Algorithm 1 Calculate $\mathbf{p} = \mathbf{A}\mathbf{f}$ or $\mathbf{f} = \mathbf{A}^T\mathbf{p}$

Require: $\mathbf{f}, mode$, beam parameters

1: Notation: Denote by (I)FT$_C$ taking an (inverse) 1D Fourier transform of every column of an image, by (I)FT$_1$ taking the (inverse) 1D Fourier transform, by Sum$_R$ taking the sum of every row of an image, and by $\mathbf{p}^i$ the i-th row of a sinogram $\mathbf{p}$.

2: Pre-compute the 2D beam shape of a horizontal beam and FT$_C$(Beam)

3: **if** mode = 'not transposed', **then**   ▷ Forward operator, $\mathbf{p} = \mathbf{A}\mathbf{f}$

4:     **for** $i = 1 : \text{angle}_{\text{count}}$ **do**

5:         $\mathbf{f}_r = \mathbf{f}$ rotated by the current angle

6:         $\mathbf{p}^i = \text{IFT}_1(\text{Sum}_R(\text{FT}_C(\mathbf{f}_r) \cdot \text{FT}_C(\text{Beam})))$

7:     **end for**

8: **else**   ▷ Backward operator, $\mathbf{f} = \mathbf{A}^T\mathbf{p}$

9:      $\mathbf{f}$ = the zero image

10:     **for** $i = 1 : \text{angle}_{\text{count}}$ **do**

11:         $\mathbf{t}$ = Multiply each column of FT$_C$(Beam) by FT$_1$($\mathbf{p}^i$)

12:         $\mathbf{u} = \text{IFT}_C(\mathbf{t})$ rotated by the reverse angle

13:         $\mathbf{f} = \mathbf{f} + \mathbf{u}$

14:     **end for**

15: **end if**

16: **return** $\mathbf{p}$ or $\mathbf{f}$

4.4. Results

4.4.1. OPT Simulations

The original object for the simulation is given in Fig. 4.3 (a). The object, with a size of 15×15 mm^2 (100×100 pixels), consists of isolated point sources, with a peak emission strength of 100 in the center pixel of the source and an emission strength set to 50 for the eight pixels around the center of the source. The object is blurred by convolving it with a Gaussian PSF for an emission wavelength of 514 nm with a waist $w_0 = 10$ µm, DOF= 1.2 mm, NA= 0.016, see Fig. 4.3 (b). Figure 4.3 (c) shows the same simulation for $w_0 = 100$ µm, DOF=122 mm, NA= 0.0016. The object data is processed following the flowchart in Fig. 4.2. The maximum number of iterations is set to 200.

The reconstruction results using filtered back projection (MATLAB function *iradon*) and the proposed method are depicted in Fig. 4.3. Figure 4.3 (d) and (e) show the FBP reconstructed images, which is based on straight parallel rays, for the two Gaussian PSFs. In Fig. 4.3 (d) it is clearly visible that, compared to the original object, the emission contrast is much lower due to the small DOF. Moreover, the reconstructed image shows that the emitters are strongly blurred in the tangential direction due to the strong divergence of the Gaussian PSF, as shown in Fig. 4.3(b). The tangential resolution deteriorates with increasing distance to the center of rotation whereas the radial resolution is slightly deteriorated, but does not depend on the distance from the center of rotation. The insets show this in more detail for two emitters. For a PSF with a larger beam waist, modeling a low NA, large DOF, imaging system, Fig. 4.3 (e) shows that there is some blurring in the reconstructed image. However, for this larger beam waist this effect depend very weakly on the distance to the center of rotation since the Gaussian PSF has much lower divergence, as shown in Fig. 4.3(c). Figure 4.3 (f) and (g) show our PSF-based reconstruction. In Fig. 4.3 (f) the contrast is completely restored, the strong tangential blurring is absent, and the reconstructed image is identical to the input image. Figure 4.3 (g) shows that also for a larger beam waist, the blurring of the emitter is fully corrected for by our PSF-based reconstruction method.

4.4.2. Fluorescent bead OPT imaging

The PSF-based reconstruction method is tested with experimental OPT imaging of a sample with fluorescent bead emitters embedded in an agarose emulsion. The experimental set-up is described in more detail in [8], the main parameters of importance are briefly discussed. The experimentally determined Gaussian PSF has a beam waist in focus of $w_0 = 6$ µm with the measured beam shape used in the PSF-based reconstruction. Emission from the center of the object is focused onto the camera plane by the imaging lens. The field of view of the experi-
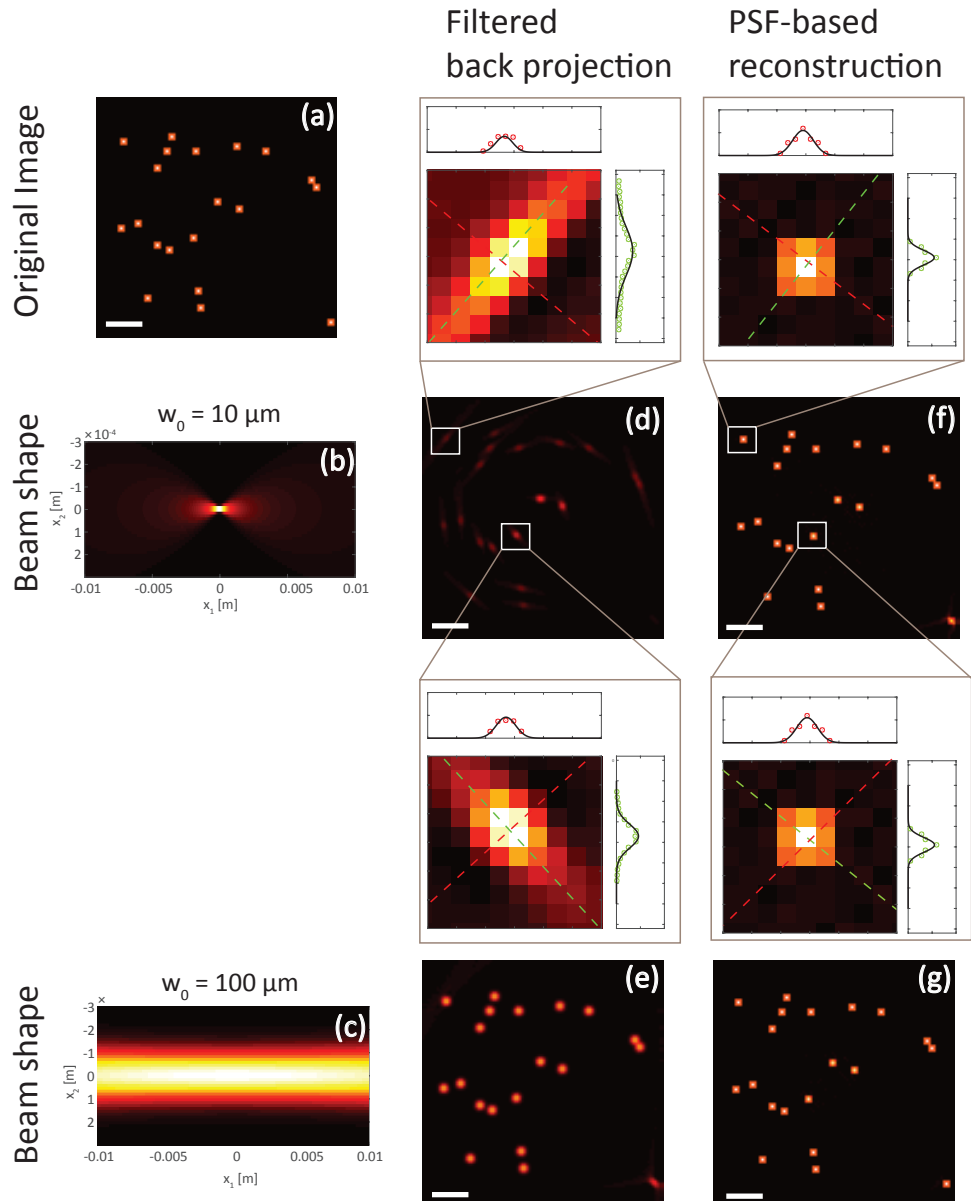
Figure 4.3: Simulation of the FBP and PSF-based image reconstruction. (a) Input image, (b) Gaussian PSF for $w_0 = 10\,\mu m$. (c) Gaussian PSF for $w_0 = 100\,\mu m$. (d, e) Reconstruction using FBP for the two Gaussian PSFs. (f, g) Reconstruction using the PSF-based approach for the two Gaussian PSFs. The scale bar is 2.5 mm.

mental data is 5.2×5.2 mm^2. In the lateral direction, the detector has 1344 pixels per projection and 360 projections are acquired over 360 degrees with a one degree spacing. The total dataset consist of 1024 sinograms covering a length of 4 mm along the rotation axis. The NA of the system is 0.05.

The measured data is pre-processed as follows. First, photo bleaching is corrected with a characteristic e^{-1} timescale of 798 seconds. Second, a constant background emission is removed from the sinogram. Third, the center of mass for each projection is estimated from the ratio of the integral of the projection times its transverse coordinate to the integral of the projection. Fourth, the center of rotation is determined from the centers of mass for all acquisition angles. Fifth, the center of rotation of the object is aligned with the center of the detector rows by shifting the data along the lateral dimension[21]. Subsequently, the 1024 sinograms are combined into 32 averaged sinograms. The averaged sinograms are further pre-processed. The noise is reduced by applying a non-local means de-noising algorithm as described by Buades et al. [22]. The half size for the de-noising window is chosen to be 9 pixels. The width of the Gaussian filter relative to its maximum intensity is set to 0.5, the search width is set to 10 pixels and the limited number of dimensions for the principal component analysis is 20. Prior to the reconstruction, the sinograms are scaled to achieve a quantitative comparison of the image quality of the two methods. Subsequently, PSF-based reconstruction of the data is performed up to the maximum number of iterations 4000 iterations and visually inspection confirmed the convergence.
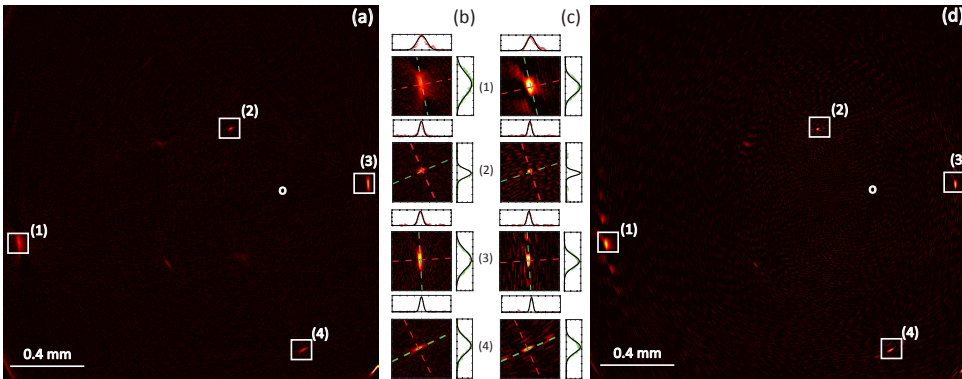

Figure 4.4: Comparison of the FBP and PSF-based reconstruction for a single averaged sinogram. (a) FBP image reconstruction of fluorescent bead data. The circle denotes the center of rotation. (b) Zoom in on reconstructed points of (a). (c) PSF-based reconstruction of the same points as in (b). (d) PSF-based reconstruction.

Figure 4.4(a) shows the reconstruction of an averaged sinogram of the experimental data using FBP. Similar to the simulations, the single point emitters appear blurred in the FBP reconstruction. In Fig. 4.4 (b) this is more clearly demonstrated by the zoom-in on the individual beads and the normalized cross-sections of the emitters. The cross sections show that the emission profiles in the reconstruction are broad and have a Gaussian-shape. Figure 4.4 (c) shows the same emitters, but reconstructed with our PSF-based approach. The emitters are brighter in comparison to the background and an improvement of the resolution is visible compared to the reconstruction using FBP. The quality of the reconstruction is analyzed by estimating the full width at half maximum (FWHM) of the Gaussian function fitted to each peak and is summarized Table 4.1. Our PSF-based reconstruction shows a significant reduction of the FWHM in both axial and tangential direction. Figure 4.4 (d) shows the same slide as in Figure 4.4 (a) reconstructed with the PSF-based reconstruction. The side lobes of the single bead 1 are 'Gibbs' like artefacts [12]. The relative large distant to the center of rotation makes it difficult to correctly reconstruct the image of this bead.

Table 4.1: FWHM resolution (µm) in axial and tangential (tang.) direction for the FBP and the PSF-based reconstruction for four fluorescent beads. Each row corresponds to the beads indicated in Fig. 4.4. The errors indicate 95 % confidence intervals.

Method	FBP		PSF-based	
Bead #	Radial FWHM	Tang. FWHM	Radial FWHM	Tang. FWHM
1	22.3 ± 0.6	50.1 ± 1.3	16.2 ± 0.6	30.0 ± 1.0
2	9.6 ± 0.3	18.0 ± 0.5	7.1 ± 0.3	10.0 ± 0.4
3	10.7 ± 0.13	42.1 ± 0.6	8.3 ± 0.2	24.9 ± 0.5
4	8.3 ± 0.2	34.9 ± 0.9	6.3 ± 0.2	24.0 ± 0.6

4.4.3. Zebrafish larva OPT imaging

The proposed PSF-based reconstruction is applied to an OPT scan of a 10 days old transgenic zebrafish larva to illustrate the performance on biological samples. The zebrafish cellular membranes are labeled with green fluorescent protein. The zebrafish larva is euthanized in ice water at the Erasmus Medical Center, Rotterdam according to animal welfare regulations. Animal experiments are approved by the Animal Experimentation Committee of the Erasmus MC, Rotterdam.

The zebrafish is mounted in agarose in our OPT system. The same experimental parameters are used as for the fluorescent bead data, but for the zebrafish imaging a total of 1791 sinograms are acquired covering a distance of 6.9 mm along the rotation axis. The NA of the system is 0.02. For all 1791 slices, the to-

mographic image is reconstructed using FBP and the PSF-based approach (no slice averaging). Prior to the reconstruction, the sinograms are scaled to achieve a better quantitative comparison of the two methods. The number of iterations is evaluated for one slide and is set to two, for which good convergence of the reconstruction is visually observed. Afterward this number of iterations is applied to the whole dataset. The reconstruction of the zebrafish larva is depicted in Fig. 4.5. Figure 4.5(a) shows the reconstruction of a single transverse slice of the data using FBP. Although the zebrafish structure is visible, the reconstruction is corrupted by radial streak artifacts, shows significant blurring, and has limited image contrast. Figure 4.5 (b) shows our PSF-based reconstruction of the same transverse slice. Figure 4.5 (c) shows the anatomy of an optical cleared zebrafish larva, of similar age, in transverse view obtained from transmission OPT from the Zebrafish Anatomy Portal [23] and is used for anatomical reference. The quality of the reconstructed image is significantly improved in terms of contrast, artifact removal, and resolution. Figures 4.5 (d,e) show two cross sections through the data that illustrate the large improvement in image contrast and resolution. In our PSF-based reconstructed image the major anatomical parts are much better resolved compared to the reconstruction using FBP (see Fig. 4.5 (a) and (b)). Similar effects are visible in Figure 4.6, which shows a coronal cross-section through the same data. Figure 4.6 (a) and (b) show the reconstruction using FBP and the PSF-based reconstruction. Figure 4.6 (c) shows a transmission OPT image of the anatomy of a 7-13 days old, optically cleared, zebrafish larva in coronal view [23].

4.5. Discussion and conclusion

We present a reconstruction algorithm routine, where the physical PSF is included in the reconstruction. Our PSF-based image reconstruction approach shows a significant improvement in OPT image quality compared to standard FBP reconstruction. In contrast to other approaches, our method incorporates the imaging geometry in the tomographic image reconstruction. As such we do not rely on filtering or deconvolution methods applied in the sinogram or image domain. A quantitative comparison of the quality of our image reconstruction algorithm with other state-of-the-art image reconstruction techniques is currently in progress [24]. The presented reconstruction method employs a 2-D reconstruction, processing the data volume slice by slice. Despite this simplification, excellent image quality is obtained. We attribute this to the fact that the zebrafish has structures that, in general, vary slowly along the length of the zebrafish. In principle our PSF-based approach could be extended to three dimensions, however, this would significantly increase the memory requirements of the routine that performs the multiplication with the system matrix and its transpose, as well
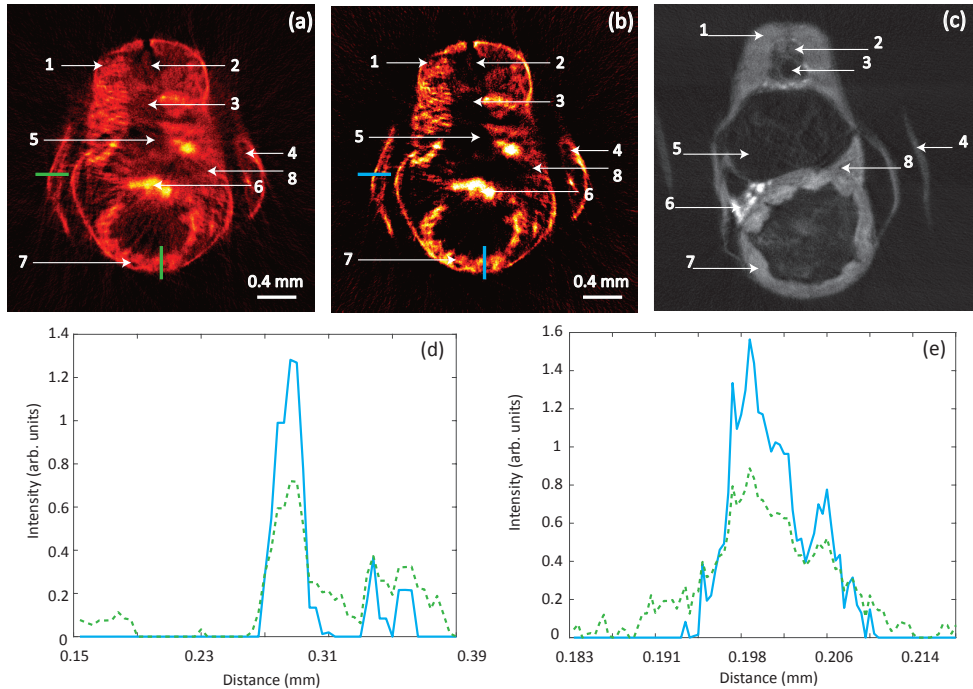
Figure 4.5: Transversal slice through the OPT reconstruction of a zebrafish larva. (a) FBP reconstruction with anatomical structures indicated. (b) PSF-based reconstruction.(c) Anatomy of a 7-13 days old optical cleared zebrafish larva [23], with anatomical features: (1) myotome, (2) spinal cord, (3) precaudal vertebra, (4) pectoral fin, (5) anterior chamber swim bladder, (6) pancreas, (7) intestinal bulb and (8) liver. (d) Cross-section in horizontal direction at line indicated in (a, b). (e) Cross-section in vertical direction at line indicated in (a, b). In (d, e) the green dashed line indicates the FBP and the blue solid line indicates the PSF-based approach.
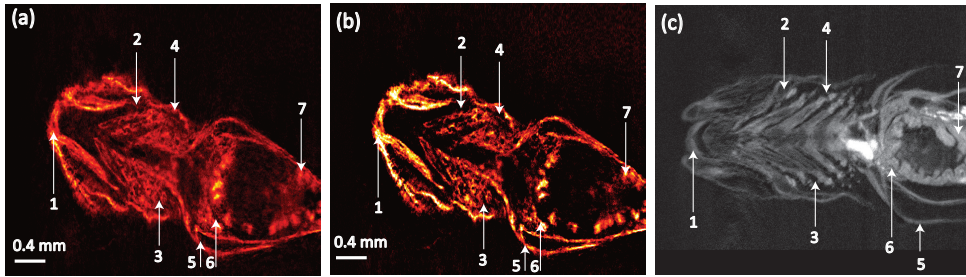
Figure 4.6: Coronal slice through the OPT reconstruction of a zebrafish larva (excluding the tail). (a) FBP reconstruction with anatomical structures indicated. (b) PSF-based reconstruction. (c) Anatomy of a 7-13 days old optical cleared zebrafish larva [23], with anatomical features: (1) intermandibularis, (2) ceratohyal, (3) opercular cavity, (4) opercle, (5) pectoral fin, (6) liver and (7) intestinal bulb.

as the computation time. For the full image size of 1344 by 1024 pixels, this 3D implementation is currently not feasible.

The reconstruction time for one slice using the PSF-based algorithm is currently about two minutes for one iteration. This potentially can be reduced by converting the presented algorithm from MATLAB to another programming language, such as C++, or using a GPU. Moreover, for a slice-based reconstruction of three-dimensional objects, the reconstruction of different slices can be parallelized. A speed-up by a factor of 200 has been observed by Leeser et al. for parallel slice processing [25]. Finally, since the PSF is varying slowly over many of the grid-points, relatively few grid points sample the beam at its narrow waist in the focal area. Hence, by representing the reconstruction problem in a different set of basis functions, potentially the size of the reconstruction problem can be reduced while obtaining the same reconstruction result.

In the reconstructions we observed that the convergence of the algorithm is strongly related to the noise level in the projections. The presented fluorophore bead data had an SNR, averaged over all the sinograms, of 31 ± 3 dB, whereas the zebrafish data had an average SNR of 67 ± 10 dB. Moreover, the zebrafish data is non-sparse compared to the bead data, which promotes convergence. As a result, the reconstruction of the fluorophore beads needed 4000 iterations, whereas the reconstruction of the zebrafish needed only 2 iterations to convergence.

In its current implementation, the PSF-based reconstruction is without including any prior information or regularization. Improvement of the convergence of the optimization possibly can be achieved by masking the data or by applying regularization methods. For example, for the sparse bead sample reconstruction, sparsity promoting ℓ_1 norm regularization, can aid in the recon-

struction accuracy as well as in the convergence rate as was shown by [26].

The proposed reconstruction technique can be extended to even higher NAs, potentially further improving the image resolution. Besides the significantly improved image quality, our PSF-based reconstruction has the advantage that arbitrary beam shapes can be incorporated in the reconstruction. In addition, other physical processes, such as refraction or scattering, can be included in the PSF-based reconstruction [27]. The presented PSF-based reconstruction is useful in other fields of optical tomographic imaging where beam propagation deviates from the ideal straight ray such as in optical diffraction tomography, transmission OPT, electron tomography, terahertz tomography, and (phase-contrast) X-ray tomography.

References

[1] E. Wolf, "Three-dimensional structure determination of semi-transparent objects from holographic data," Opt. Comm., vol. 1, no. 4 , pp. 153 – 156 (1969).

[2] J. Sharpe, U. Ahlgren, P. Perry, B. Hill, A. Ross, J. Hecksher-Sørensen, R. Baldock, and D. Davidson, "Optical projection tomography as a tool for 3D microscopy and gene expression studies," Science, vol. 296, no. 5567, pp. 541–545 (2002).

[3] L. Chen, N. Andrews, S. Kumar, P. Frankel, J. McGinty, and P. M. French, "Simultaneous angular multiplexing optical projection tomography at shifted focal planes," Opt. Lett., vol. 38, no. 6, pp. 851–853 (2013).

[4] Q. Miao, J. Hayenga, M. G. Meyer, T. Neumann, A. C. Nelson, and E. J. Seibel, "Resolution improvement in optical projection tomography by the focal scanning method," Opt. Lett., vol. 35, no. 20, pp. 3363–3365 (2010).

[5] W. Xia, R. M. Lewitt, and P. R. Edholm, "Fourier correction for spatially variant collimator blurring in SPECT," IEEE Trans. Med. Imaging, vol. 14, no. 1, pp. 100–115 (1995).

[6] J. R. Walls, J. G. Sled, and J. Sharp, "Resolution improvement in emission optical projection tomography," Phys. Med. Biol., vol. 52, no. 10, pp. 2775–90. (2007).

[7] A. Darrell, H. Meyer, K. Marias, M. Brady, and J. Ripoll, "Weighted filtered backprojection for quantitative fluorescence optical projection tomography," Phys. Med. Biol., vol. 53, no. 14 pp. 3863–3881 (2008).

[8] J. van der Horst and J. Kalkman, "Image resolution and deconvolution in optical tomography," Opt. Express, vol. 24, no. 21, pp. 24460–24472 (2016).

[9] M. Temerinac-Ott, O. Ronneberger, R. Nitschke, W. Driever, and H. Burkhardt, "Spatially variant Lucy Richardson deconvolution for multiview fusion of microscopal 3D images," IEEE International Symposium on Biomedical Imaging: From Nano to Macro, pp. 899 – 904 (2011).

[10] L. Chen, J. McGinty, H. B. Taylor, L. Bugeon, J. R. Lamb, M. J. Dallman, and P. M. W. French, "Incorporation of an experimentally determined MTF for spatial frequency filtering and deconvolution during optical projection tomography reconstruction," Opt. Express, vol. 20, no. 7, pp. 7323–7337 (2012).

[11] B. Recur, J. P. Guillet, I. Manek-Hönninger, J. C. Delagnes, W. Benharbone, P. Desbarats, J. P. Domenger, L. Canioni, and P. Mounaix, "Propagation beam consideration for 3D THz computed tomography," Opt. Express, vol. 20, no. 6, pp. 5817 – 5829 (2012).

[12] E. Rapisarda, V. Bettinardi, K. Thielemans, and M. C. Gilardi, "Image-based point spread function implementation in a fully 3D OSEM reconstruction algorithm for PET," Phys. Med. Biol., vol. 55, no. 14, pp. 4131–4151 (2010).

[13] R. Formiconi, A. Pupi, and A. Passeri, "Compensation of spatial system response in SPECT with conjugate gradient reconstruction technique," Phys. Med. Biol., vol. 34, no. 1, pp. 68–84 (1989).

[14] Z. Chen and R. Ning, "Three-dimensional point spread function measurement of cone-beam computed tomography system by iterative edge-blurring algorithm," Phys. Med. Biol., vol. 49, no. 10, pp. 1865–1880 (2004).

[15] M. Gu, *Advanced Optical Imaging Theory* (Springer, 2000).

[16] J. Radon and P. Parks, "On the determination of functions from their integral values along certain manifolds," IEEE Trans. Med. Imaging, vol. 4, pp. 170–176 (1986). Translation of the original paper by Johann Radon 1917.

[17] J. Goodmann, *Introduction to Fourier Optics* (MaGraw-Hill, 1996), 2nd ed.

[18] A. E. Siegman, *Lasers* (University Science Books, 1986).

[19] C. C. Paige and M. A. Saunders, "LSQR: An algorithm for sparse linear equations and sparse least squares," ACM Transactions on Mathematical Software, vol. 8, no. 1, pp. 43-71 (1982).

[20] R. Barrett, M. Berry, T. F. Chan, J. Demmel, J. Donato, J. Dongarra, V. Eijkhout, R. Pozo, C. Romine, and H. van der Vorst, *Templates for the solution of linear systems: Building blocks for iterative methods,* SIAM (1994).

[21] S. G. Azevedo, D. F. Schneberk, J. P. Fitch, and H. E. Martz, "Calculation of the rotational centers in computed tomography sinogram," IEEE Trans. Nucl. Sci. vol. 37, pp. 1525–1540 (1990).

[22] A. Buades, B. Coll, and J. M. Morel, *On image denoising methods,* Tech. rep., Technical Note, CMLA (Centre de Mathematiques et de Leurs Applications) (2004).

[23] D. Salgado, C. Marcelle, P. D. Currie, and R. J. Bryson-Richardson, "The zebrafish anatomy portal: a novel integrated resource to facilitate zebrafish research," *Developmental Biology*, vol. 372, no. 1, pp. 1–4, (2012).

[24] A. K. Trull, J. van der Horst, L. J. van Vliet and J. Kalkman, "Comparison of image reconstruction techniques in optical projection tomography," Appl. Opt., vol. 57, no. 8, pp. 1874-1882 (2018).

[25] M. Leeser, S. Mukherjee, and J. Brock, "Fast reconstruction of 3D volumes from 2D CT projection data with GPUs," BMC Research Notes (2014).

[26] S.-J. Kim, K. Koh, M. Lustig, S. Boyd, and D. Gorinevsky, "An interior-point method for large-scale l_1-regularized least squares," IEEE J. Sel. Top. Signal Process., vol. 1, no. 4, pp. 606 – 617 (2007).

[27] M. Haidekker, "Optical transillumination tomography with tolerance against refraction mismatch," Comput. Methods. Programs. Biomed., vol. 80, no. 3, pp. 225–235 (2005).

Chapter 5

Comparison of image reconstruction techniques in optical projection tomography

We present a comparison of image reconstruction techniques for optical projection tomography. We compare conventional filtered back projection, sinogram filtering using the frequency-distance relationship (FDR), image deconvolution, and 2D point spread function (PSF) based iterative reconstruction. The latter three methods aim to remove the spatial blurring in the reconstructed image originating from the limited depth of field caused by the PSF of the imaging system. The methods are compared based on simulated data, experimental optical projection tomography data of single fluorescent beads, and high-resolution optical projection tomography imaging of an entire zebrafish larva. We demonstrate that the FDR method performs poorly on data acquired with high numerical aperture optical imaging systems. We show that the deconvolution technique performs best performance on highly sparse data with low signal-to-noise ratio. The PSF-based reconstruction method is superior for non-sparse objects and data of high signal-to-noise ratio.

5.1. Introduction

For the study of biological samples and small animals, such as zebrafish or (mouse) embryos, optical tomographic imaging techniques, such as optical diffraction tomography [1] and optical projection tomography (OPT) [2], are among the standard imaging modalities. From these samples, projections of transmitted or emitted (fluorescence) light are recorded. From these projections, an image of the object is reconstructed using tomographic reconstruction techniques. In OPT, a lens-based optical imaging system is used to image the sample onto the detector. The optical system is characterized by the point spread function (PSF).

Due to light diffraction, instead of collecting light along a straight path (line) through the object, light from a sample volume, determined by the shape of the PSF, is collected by the detector. For image acquisition with high numerical aperture (NA) small depth of focus lenses, this results in efficient light collection from the focal plane. However, light from regions far from the focal plane is inefficiently collected. Standard reconstruction techniques, such as filtered back projection (FBP), are based on the straight ray approximation, which neglects the effect of light diffraction by the imaging lens [3]. Consequently, OPT images reconstructed with FBP can suffer from severe image degradation.

Reconstruction algorithms, that include the PSF in the reconstruction, have been developed for clinical tomographic imaging techniques such as PET [4], SPECT [5], and X-ray CT [6]. Also, for optical tomographic imaging, various reconstruction techniques were developed to correct for the effect of the PSF, as indicated in Fig. 5.1, where these techniques are divided in three categories. First, correction for the effect of the PSF can take place before the reconstruction, either by filtering the sinogram in real space using an iterative deconvolution [7] or by a filtering the sinogram in Fourier space with a filter based on the frequency-distance relation [8, 9]. In both cases these methods are directly applied to the measured projection data and the processed sinogram is converted to an image using FBP. Second, correction for the effect of the PSF can take place after reconstruction using deconvolution of the image reconstructed with FBP [10]. Third, we recently demonstrated correction for the effect of the PSF during the tomographic reconstruction process itself using iterative optimization [11].

In this work, we compare three advanced tomographic reconstruction methods, namely FDR followed by FBP [9], FBP followed by image deconvolution [10], and 2D PSF-based reconstruction [11] that all correct for the effect of the optical PSF, with the classical FBP [3]. First, we test all methods on their ability to reduce tangential blurring in the reconstructed image using simulated data. In these simulation experiments, we study the effect of SNR and numerical aperture on the reconstruction error. Second, we compare the performance of all reconstruction algorithms on experimental data. Since no reference image is available for experimental data, a no-reference or blind image quality assessment (NR-IQA) is performed to provide an image quality measure that enables quantitative comparison of the quality of the different reconstruction techniques. Finally, we indicate which algorithm to choose for objects that have different signal-to-noise ratio and/or are imaged with different numerical apertures.
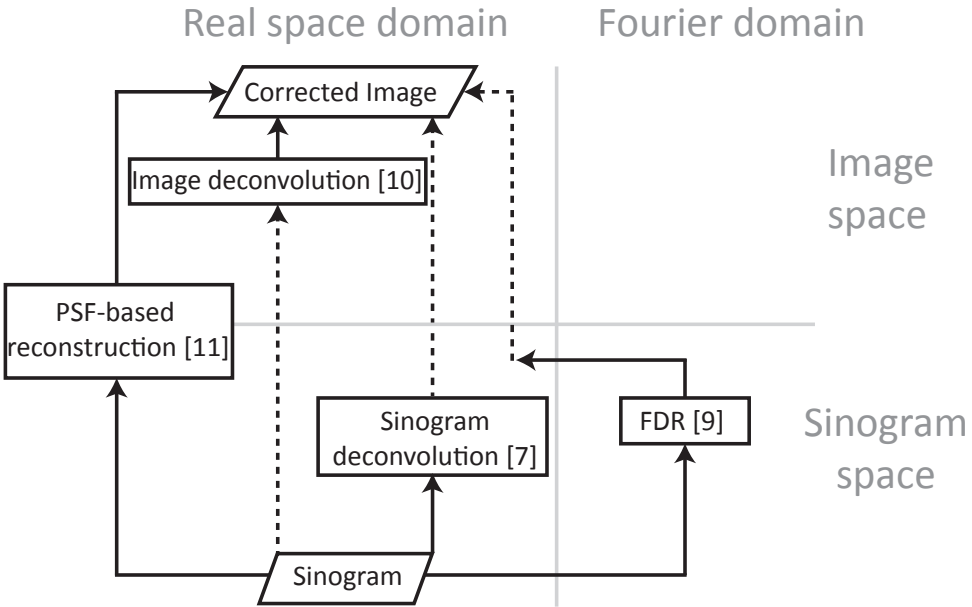
Real space domain   Fourier domain

Figure 5.1: Schematic overview of different tomographic reconstruction methods that correct for the PSF [7, 9–11]. The left hand side indicates that the reconstruction is performed in real space, the right hand side indicates that it is performed in Fourier space. The bottom side indicates that the reconstruction is performed in sinogram space, the top side indicates that is performed in image space. The dashed lines indicate conventional FBP reconstruction.

5.2. Theory of tomographic image reconstruction

5.2.1. General problem formulation

For the imaging geometry of OPT, see Fig. 5.2(a), light from the object is imaged from the sample onto the detector using lenses. As a result the image of a point source gives a blurred spot on the detector determined by the PSF $h(x, y, z)$. In general, the shape of the 3D PSF can be complicated as it is dependent on the exact imaging geometry. It can be obtained using Fourier optics calculations, optical simulations, or experimental measurement. For the case of incoherent imaging of an object of which its structure varies slowly in the y direction, it was shown [10, 11] that the projections are given by the convolution of the 2D object $f(x, z)$ by the 2D PSF $|h(x, z)|^2$ as

$$p(s, \theta) = \iint\limits_{-\infty}^{\infty} |h(x\cos\theta + z\sin\theta - s, x\sin\theta + z\cos\theta)|^2 \, f(x, z) \, \mathrm{d}x \, \mathrm{d}z, \qquad (5.1)$$

where $|h(x, z)|^2$ is the spatially variant incoherent PSF, s the lateral shift and $\theta \in [0, 2\pi]$ the rotation angle. Equation 5.1 shows that the measured intensity on the

detector is given by an integral over the object, which is illustrated in Fig. 5.2(b). To facilitate a quantitative comparison of the different reconstruction algorithms we use a 2D Gaussian PSF that is described by

$$|h(x,z)|^2 = \left| \frac{1}{\sqrt{1 + \left(\frac{z}{z_R}\right)^2}} \exp\left(-\frac{x^2}{w_0^2\left(1 + \left(\frac{z}{z_R}\right)^2\right)}\right) \right|^2, \qquad (5.2)$$

where $z_R = \pi w_0^2/\lambda$ is the Rayleigh range, w_0 the Gaussian beam waist, and λ the wavelength. For a Gaussian PSF, both the FDR filter and the image deconvolution filter [10] can be analytically calculated. This enables a quantitative comparison. However, the general results of our comparison hold for arbitrary beam shapes if correctly implemented in the corresponding reconstruction algorithm.
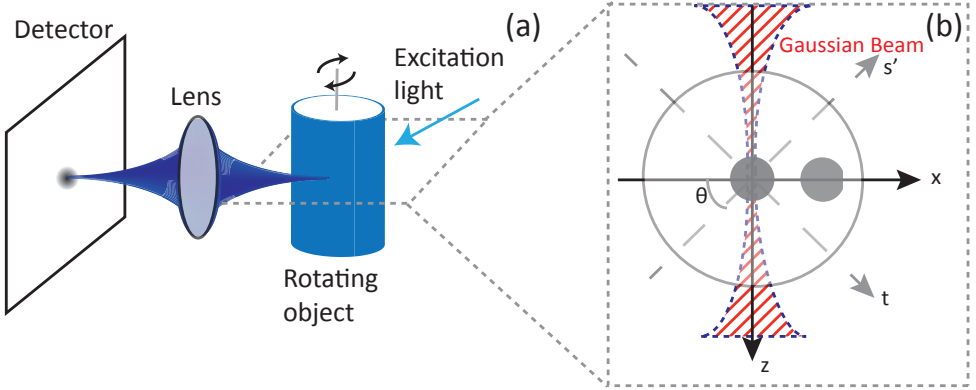

Figure 5.2: (a) Schematic overview of the optical projection tomography fluorescence imaging geometry. (b) 2D slice of the object and the Gaussian beam. The rotation angle is denoted by θ.

5.2.2. FBP reconstruction

Due to its fast reconstruction time and the easy concept FBP reconstruction is still the most commonly used reconstruction technique in optical tomography. In FBP a straight ray geometry is used over which the measured projection is back projected onto the object. FBP is the correct reconstruction for the case of an ideal imaging system where the PSF is described by $|h(x,z)|^2 = \delta(x)$. This means that irrespective of the distance of the object to the collection system the signal from all pixels on a line through the object is collected onto a single detector pixel. For $|h(x,z)|^2 = \delta(x)$, Eq. 5.1 results in the standard Radon transform [3, 12]

$$p(s,\theta) = \iint\limits_{-\infty}^{\infty} f(x,z)\delta(x\cos\theta + z\sin\theta - s)\,\mathrm{d}x\,\mathrm{d}z. \qquad (5.3)$$

In this case the object can be retrieved by FBP as

$$f(x,z) = \int\limits_{0}^{\pi} \int\limits_{-\infty}^{\infty} P_\theta(f_s) \exp(i2\pi f_s s)|f_s|\, df_s\, d\theta\,, \tag{5.4}$$

where $P_\theta(2\pi f_s)$ is the 1D Fourier transform of the projection data at angle θ. However, in case the PSF is not ideal, FBP reconstruction causes artifacts and/or severe blurring in the reconstructed image. Next, we describe three algorithms that incorporate the PSF before (FDR), after (image deconvolution) or during the image reconstruction (PSF-based reconstruction).

5.2.3. FDR reconstruction

Originating from the field of X-ray CT, reconstruction methods that take the PSF into account are algorithms based on the frequency-distance relationship (FDR) [8, 9, 13]. FDR has been implemented for reconstructions of OPT tomograms corrected for the out of focus deterioration of resolution due to the imaging system [9]. In FDR the blurring of the sinogram in the Fourier domain is described by

$$P_b(f_x, f_y) = H(f_x, f_y) P_o(f_x, f_y)\,, \tag{5.5}$$

where $P_b(f_x, f_y)$ is the Fourier transform of the blurred sinogram, $H(f_x, f_y)$ is the filter based on the PSF describing the blurring, and $P_o(f_x, f_y)$ is the Fourier transform of the sinogram of the object with spatial frequencies f_x and f_y. The system PSF is used to create an inverse filter $H^{-1}(f_x, f_y)$ that is multiplied with the Fourier transform of the sinogram to remove the blurring caused by $H(f_x, f_y)$ [13, 14]. For the Gaussian PSF in Eq. 5.5 the filter $H(f_x, f_y)$ is given by

$$H(f_x, f_y) = \frac{1}{\left(1 + \frac{\lambda^2 f_y^2}{f_x^2 \pi^2 w_0^2}\right)\sqrt{\frac{w_0}{\frac{\lambda^2 f_y^2}{f_x^2} + \pi^2 w_0^2}}} \times \exp\left(-\frac{f_x}{8}\left(\frac{\lambda^2 f_y^2}{f_x^2 \pi^2 w_0} + f_x \pi w_0^2\right)\right).$$

Analytical Derivation of the FDR filter for a Gaussian PSF
In the following, we derive the analytical inverse filter $H(f_x, f_y)^{-1}$. Let us assume a point source object located on the x-axis at distance l from the origin defined as

$$f(x,z) = \delta(x - l)\delta(z). \tag{5.6}$$

The PSF is defined as in Eq. 5.2. The blurred sinogram is then defined as

$$p_b(s,\theta) = \int\int \delta(x - l\cos\theta)\delta(z)|h(x\cos\theta + z\sin\theta - s, x\sin\theta + z\cos\theta)|^2 dx\, dz.$$

Integration over x and z, with $|h(x,z)|^2$ described by Eq. 5.2 leads to

$$p_b(s,\theta) = \frac{1}{1 + \frac{l^2 \lambda^2 \sin^2 \theta}{\pi^2 w_0^2}} \exp\left(-\frac{2(s - l\cos\theta)^2}{w_0\left(1 + \frac{l^2 \lambda^2 \sin^2 \theta}{\pi^2 w_0^2}\right)}\right). \tag{5.7}$$

The Fourier transform of the $p_b(s,\theta)$ [14] is given by

$$P_b(f_x, f_y) = \frac{1}{2\pi} \int_0^{2\pi} \int_{-\infty}^{\infty} p_b(s,\theta) \exp(-j(f_x s + f_y \theta)) \mathrm{d}s\, \mathrm{d}\theta. \tag{5.8}$$

Inserting Eq. 5.7 in Eq. 5.8 and integration over s leads to

$$P_b(f_x, f_y) = \frac{1}{2\pi} \int_0^{2\pi} \frac{1}{2\pi\left(1 + \frac{\lambda^2 f_y^2}{f_x^2 \pi^2 w_0^2}\right) \sqrt{\frac{w_0}{\frac{\lambda^2 f_y^2}{f_x^2} + \pi^2 w_0^2}}}$$

$$\times \exp\left(-\frac{f_x}{8}\left(f_x \pi^2 w_0^2 - 8jl\cos\theta + \frac{f_x l^2 \lambda^2 \sin^2 \theta}{\pi^2 w_0^2}\right)\right)$$

$$\times \exp(-jf_y \theta))\, \mathrm{d}\theta. \tag{5.9}$$

An expression for the filter can be derived by assuming a stationary phase approximation, i.e., the function $\exp(-jf_y \theta + jf_x l\cos\theta)$ only takes on a non-zero value if the derivative of this angle with respect to θ is zero, i.e.,

$$\frac{d}{d\theta}(f_y \theta - f_x l\cos\theta) = f_y + f_x l\sin\theta = 0, \tag{5.10}$$

which is equivalent to $l\sin\theta = -\frac{f_y}{f_x}$. Evaluating this in Eq. 5.9 gives

$$P_b(f_x, f_y) \approx \frac{1}{2\pi\left(1 + \frac{\lambda^2 f_y^2}{f_x^2 \pi^2 w_0^2}\right) \sqrt{\frac{w_0}{\frac{\lambda^2 f_y^2}{f_x^2} + \pi^2 w_0^2}}}$$

$$\times \exp\left(-\frac{f_x}{8}\left(\frac{\lambda^2 f_y^2}{f_x^2 \pi^2 w_0} + f_x \pi^2 w_0^2\right)\right)$$

$$\times \left[\int_{\theta_1 - \epsilon}^{\theta_1 + \epsilon} \exp(g)\, d\theta + \int_{\theta_2 - \epsilon}^{\theta_2 + \epsilon} \exp(g) d\theta\right], \tag{5.11}$$

where $g = -j(f_x l\cos\theta + f_y \theta)$. From a similar derivation for an ideal imaging system, which only contains the last term of Eq. 5.11 and using Eq. 5.5, it can be derived that the unblurring FDR filter is

$$H^{-1}(f_x, f_y) = \left(1 + \frac{\lambda^2 f_y^2}{f_x^2 \pi^2 w_0^2}\right) \sqrt{\frac{w_0}{\frac{\lambda^2 f_y^2}{f_x^2} + \pi^2 w_0^2} \frac{1}{\exp\left(\frac{f_x}{8}\left(\frac{\lambda^2 f_y^2}{f_x^2 \pi^2 w_0} + f_x \pi^2 w_0^2\right)\right)}}. \quad (5.12)$$

5.2.4. Image deconvolution

A general approach for PSF correction is image deconvolution. However, in case of tomographic reconstruction the PSF of the reconstructed image is a complicated expression of the PSF of the imaging system with which the projections are measured. For a Gaussian beam the 2D PSF of the FBP reconstructed image is spatially varying with the coordinate x and coordinate y according to

$$\text{PSF}(x, y) = \mathcal{R}_{-\theta}\left(\sqrt{\frac{1}{\pi^2 a_y a_x}} \exp\left(-\left[\frac{x^2}{a_x} + \frac{y^2}{a_y}\right]\right)\right). \quad (5.13)$$

In Eq. 5.13 $a_x = w_0^2/2$ and $a_y = \left(w_0^2 + \frac{\lambda^2 r_0^2}{\pi^2 w_0^2}\right)/2$, r_0 is the location of the PSF in the image domain and $\mathcal{R}_{-\theta}$ is an operator to perform a standard coordinate transformation over an angle [10]. From Eq. 5.13 it can be observed that the resolution in the tangential direction deteriorates with increasing distance to the rotation axis whereas the resolution in the radial direction is constant. Using a conversion to polar coordinates the image can be successively deconvolved in the radial and angular direction using deconvolution (e.g., with the Lucy-Richardson algorithm).

5.2.5. PSF-based reconstruction

An advanced reconstruction method is based on the inclusion of the imaging system's PSF into the tomographic reconstruction [11]. Given the measured projections $\mathbf{p}$ and the effect of imaging system PSF given by Eq. 5.2 as described by the matrix $\mathbf{A}$ the object $\mathbf{f}$ can be reconstructed by solving

$$\underset{\mathbf{f}}{\text{argmin}} \quad \frac{1}{2}\|\mathbf{A} \cdot \mathbf{f} - \mathbf{p}\|_2^2, \quad (5.14)$$

where $\|\cdot\|_2^2$ denotes the Euclidean norm. Equation 5.14 can be solved using a least squares optimization method.

5.3. Methods

5.3.1. Reconstruction algorithms

All tomographic reconstructions are performed on a computer with an Intel(R) Xeon(R) CPU Processor (E5-1620 v3@3.50 GHz), 32 GB installed memory and a

64-bit operating system. The data are processed using software written in the commercial software package MATLAB (Mathworks, R2016a). The reconstructions with FBP are done with the MATLAB function *iradon*. The FDR method is implemented using the analytical expression for the inverse filter $H^{-1}(f_x, f_y)$, derived in Section 5.2.3. After the FDR reconstruction, intensity thresholding is applied to remove reconstruction artifacts. The thresholding is done individually for each dataset. For the simulations a thresholding of 0.04 (15.7% of the peak value) is used. For the zebrafish dataset the threshold is set to 0.1 (2.5% of the peak value).

The deconvolution and the PSF-based method implementations are identical to the original implementation of the methods [10, 11]. To enable a quantitative comparison of the reconstructed images, all reconstructed images are scaled using the scaling described in [11].

5.3.2. Image quality assessment

For both simulated and experimental data of point objects, the image quality is determined from the width of the PSF in the reconstructed image. The full width at half maximum (FWHM) is obtained from a bivariate Gaussian fit in a region of interest around the image of isolated single objects with the width in the two perpendicular dimensions as independent fit parameters.

Since no reference image is available for experimental data of spatially extended objects, a no-reference or blind image quality assessment (NR-IQA) is used to compare the quality of the different reconstruction results. NR-IQA aims to determine quantitative measures to objectively predict the quality of an image based only on the image itself [15]. In our comparison, we use the signal-to-noise ratio (SNR) and the sharpness provided by NR-IQA to assess the quality of the reconstructed images.

It is assumed that both the image quality increases with increasing SNR and image sharpness. In case of suboptimal performance, both these metrics are lower. The SNR of an image is defined as

$$\text{SNR} = 20 \log \left(\frac{\mu_{\text{signal}}}{\sigma_{\text{noise}}} \right), \tag{5.15}$$

where μ_{signal} is the average image intensity in a signal mask region and σ_{noise} is the standard deviation of the image intensity in a noise region. The latter corresponds to the region outside the signal mask [16].

First, a signal and a background mask are created for the image reconstructed with every method. The signal mask comprises all pixels whose intensity is higher than the average background signal plus four times its standard deviation. The background mask is defined as the area of the image that is not in the signal

mask. Hence, in the background mask the image intensity is smaller than the average background signal plus four times its standard deviation. Second, the intersection of the signal masks and background masks for all four reconstruction methods are estimated. This final signal mask is then used to estimate the intersection signal in the image. The final background mask is used to estimate the standard deviation of the background, which we use as a measure of the noise. We use the intersection masks, since no ground truth of the signal and noise regions is available. Hence, the intersection masks weighs each method in the same way in the determination of the SNR.

Following the definition of De et al. [17] the sharpness in the image is defined in the frequency domain of the image as the ratio FM according to

$$FM = \frac{T}{M \cdot N}, \tag{5.16}$$

where the T denotes the total number of pixels in the Fourier transform of the image, that have a magnitude larger than the maximum magnitude divided by 1000. The Fourier transformed image is centered so that the zero-frequency components are represented in the center of the spectrum. The denominator contains the product of the image size of M times N in the two dimensions. The use of the metric of Eq. 5.16 for image quality assessment is based on the assumption that a sharper image will have a larger number of high frequency components in the frequency domain compared to a blurred image, which has mainly low frequency components.

5.3.3. Tomographic reconstruction simulations

Multiple images of size 5×5 mm^2 (300 by 300 pixels) are generated with a circular Gaussian shaped object placed at a specific distance from the origin in every image. The objects have a full width at half maximum (FWHM) in the x and y direction of 125 µm. The object in the first image is located in the center of the image, the object in the last image is located horizontally close to the edge of the image. The Gaussian PSF is implemented for NA= 0.027 and NA= 0.053 and with a beam waist of $w_0 = 6$ µm. The depth of field (DOF), defined as twice the Rayleigh length, for NA= 0.027 is DOF= 48 µm and for NA= 0.053, the DOF = 24 µm. The sinogram is blurred with the Gaussian PSF and then used as input for the different reconstruction algorithms. After reconstruction, a Gaussian is fitted to each reconstructed object and the FWHM of the object in the radial and tangential direction is determined. Deconvolution of the FBP reconstructed image is performed with the MATLAB function *deconvlucy*, with the number of iterations set to 100. The maximum number of iterations of the PSF-based algorithm for an NA of 0.027 is set to 4000 and for an NA of 0.053 to 6000. The convergence

and optimal number of iterations is object, NA, and SNR dependent. For both the deconvolution and PSF-based reconstruction convergence of the method for the indicated number of iterations is validated visually. The absolute error of the projections is estimated as $||\mathbf{A}\mathbf{f} - \mathbf{p}||_2^2$, where $\mathbf{A}$ denotes the geometry matrix, $\mathbf{f}$ the reconstructed image and $\mathbf{p}$ the projections with added noise.

5.4. Results

5.4.1. Image reconstruction comparison of simulations

Figure 5.3 shows the reconstruction as well as the tangential and radial FWHM of the object located at a varying radial distance to the center of the image. A sharp image on the detector is made for radial distance 0, which is the center of rotation. In Fig. 5.3 (a) the original image and the reconstruction results using FBP, FDR, image deconvolution and PSF-based reconstruction are shown for an NA of 0.027. It is clear that the FBP reconstructed image is severely blurred, especially for objects far from the center. The FDR method produces side lobes in the radial and tangential direction and has a lower peak intensity. Both deconvolution and PSF-based reconstruction show a clear reduction in tangential blurring compared to FBP. Figure 5.3(b) shows the fitted FWHM of the objects for an NA= 0.027. The optimal resolution of the reconstruction is determined by the sum of the variance of the PSF and of the object, subsequently converted to FWHM, which is indicated for the tangential and radial directions. For the FBP reconstruction, the width in the tangential direction increases significantly and follows the theoretical prediction. The FDR method shows a significantly improved result, albeit slightly above the fundamental limit for larger distances to the origin. For small distances to the origin it is lower than the theoretical minimum. This difference is within the resolution of the simulation and attributed to the non-Gaussian shape of the FDR reconstructed objects (e.g. the presence of side lobes). The image deconvolution method and the PSF-based reconstruction technique, show an almost full reduction of the tangential blurring for all radial distances. In the radial direction, all algorithms achieve diffraction limited resolution. A comparison of the PSF in the tangential direction is shown in Fig. 5.3 (c) for an object at a distance of 2 mm from the center. In Fig. 5.3 (d) the original image and the reconstruction results using FBP, FDR, image deconvolution and PSF-based reconstruction are shown for NA= 0.053. For this higher NA the FBP reconstructed image shows a stronger burring than in Fig. 5.3 (a). While deconvolution and PSF-based reconstruction give good results, the FDR method produces side lobes in the radial and tangential direction. Figure 5.3 (e) shows the FWHM of the same objects. The FBP reconstruction shows an increase of the tangential width, which is now even larger for the high NA case. It
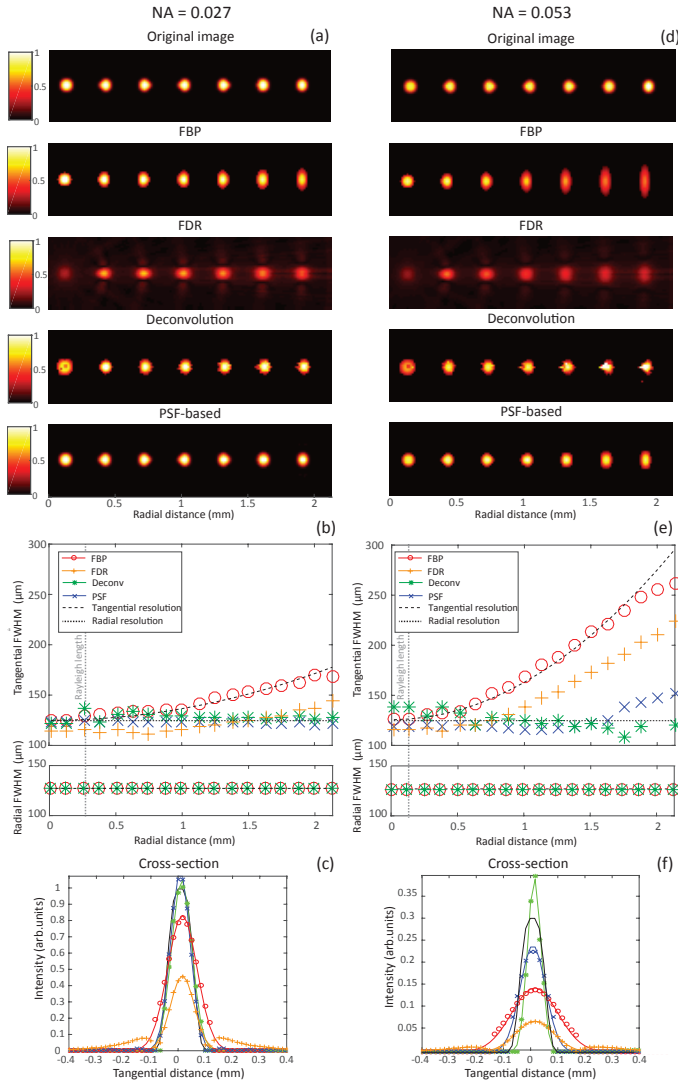
Figure 5.3: Comparison of the ground truth and the reconstructed image. (a) The original image, and the reconstructions using FBP, FDR, image deconvolution, and PSF-based reconstruction for a PSF with an NA = 0.027. (b) Tangential and radial FWHM of the cavities for a PSF with an NA = 0.027. (c) Cross-section of the reconstructions (shown in (a)) in the tangential direction for a distance of 2 mm from the center. The solid black line indicates the input object. (d) The original image, and the reconstructions using FBP, FDR, image deconvolution, and PSF-based reconstruction for a PSF with an NA = 0.053. (e) Tangential and radial FWHM of the cavities for a PSF with an NA = 0.053. (f) Cross-section of the reconstructions (shown in (d)) in the tangential direction for a distance of 2 mm from the center. The solid black line indicates the input object.

can be observed that the deconvolution algorithm is able to reduce the tangential blurring, whereas PSF-based reconstruction performs less than ideal at large distances from the center. The FDR gives a significant larger FWHM, especially at large radial distances from the center. A comparison of the PSF in the tangential direction is shown for a distance of 2 mm from the center in Fig. 5.3 (f).

The previous simulations are performed for the noise-free case, i.e., the SNR is infinite. However, the presence of noise influences the reconstruction result. For iterative methods such as the deconvolution and the PSF-based reconstruction, the convergence rate and obtained optimal solution depend on the signal-to-noise ratio in the projections. The influence of noise on the reconstruction is studied for a single circular cavity object at a radial distance of 2 mm from the center. Various amounts of noise are added to the projections. Figure 5.4 illustrates the relation between the absolute error of the projections (according to Eq. 5.14) and the number of iterations for a low (top) and a high (bottom) NA. For reconstruction methods based on analytical methods, such as the FBP or FDR, the absolute reconstruction error is similar for low and high SNR (lines overlap in Fig. 5.4). For both NA's the deconvolution approach, which takes the FBP as input, gives a lower absolute error compared to FDR and FBP. Although deconvolution is iterative, convergence is already reached after the first iteration. The PSF-based reconstruction has the lowest absolute error compared to the other methods for both high and low NA. For large number of iterations an amplification of the reconstruction error can be seen. If not terminated, the reconstruction error for the PSF-based reconstruction grows. It may even exceed that of the other methods. We noted that the number of iterations for which convergence is observed depends on the object to be reconstructed. Hence, the optimum number of iterations needs to be determined for each dataset individually, which is an object-dependent regularization.

5.4.2. Image quality of experimental OPT data

We investigate the reconstruction of single fluorescent bead emitters embedded in an agarose emulsion measured with OPT. The experimental set-up is described in more detail in [10], the main parameters of importance are briefly discussed. The experimentally determined Gaussian PSF has a beam waist in focus of $w_0 = 6\,\mu m$, NA= 0.053, and the measured Gaussian beam shape is used in the PSF-based reconstruction. A sharp image on the detector is made for radial distance 0, which is the center of rotation. The field of view of the experimental data is 5.2×5.2 mm^2. In the lateral direction, the detector has 1344 pixels per projection and 360 projections are acquired over 360 degrees with a one degree spacing. The total dataset consist of 1024 sinograms covering a length of 4 mm along the rotation axis. Subsequently, the 1024 sinograms are combined into 32
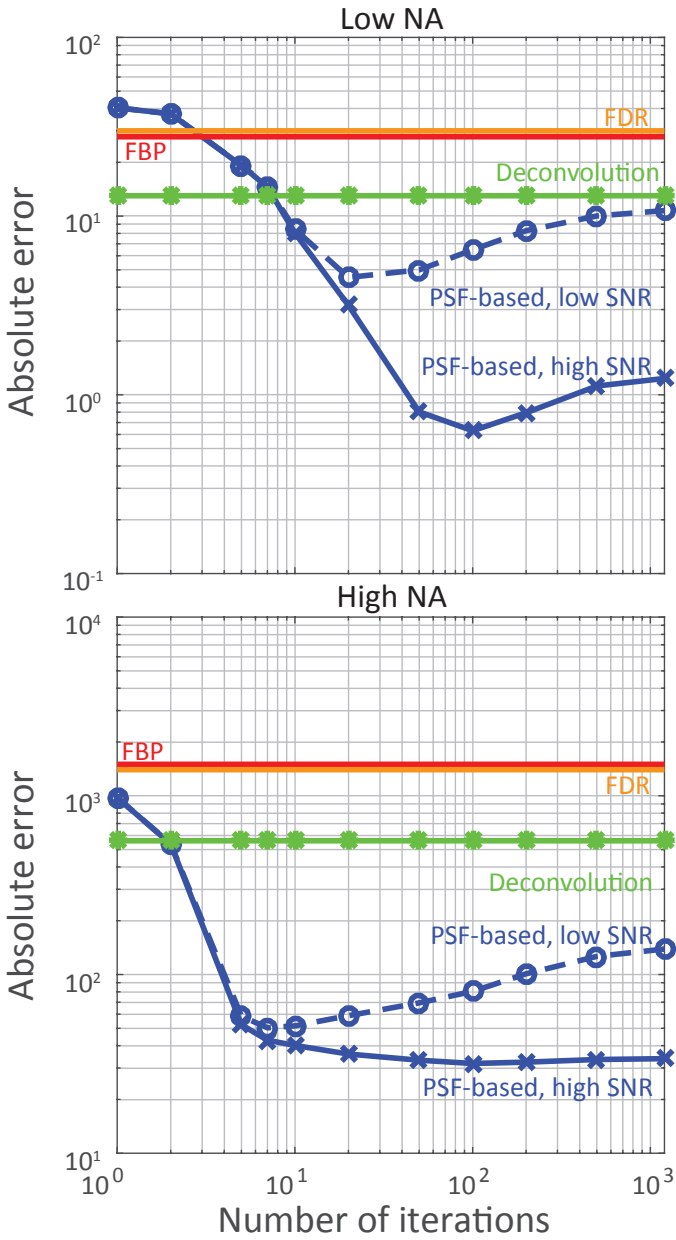
Figure 5.4: Reconstruction error for a low NA (top) and a high NA (bottom) optical imaging system for SNR= 40 dB (solid lines) and SNR= 20 dB (dashed lines). For PSF-based reconstruction simulations are performed for reconstruction at different SNR (indicated).

averaged sinograms. The pre-processing is described in [11].

Figure 5.5 shows the reconstructions for a single averaged slice with the different methods. The tangential and radial blurring are clearly visible in Fig. 5.5 (a) and Fig. 5.5 (b), where the image is reconstructed with FBP. For some beads, the FDR reconstruction shows improvement over FBP, as shown in Fig. 5.5 (c). The PSF-based reconstruction, shown in Fig. 5.5 (e), significantly reduces the blurring in the radial and tangential blurring direction compared to Fig. 5.5 (b). The greatest improvement is given by the deconvolution method, shown in Fig. 5.5 (d). Both the radial and tangential blurring are significantly reduced. The resolution of the different methods applied to all four beads is quantitatively represented in Table 5.1.

We determined the sharpness metric and the SNR for the transverse slice

Table 5.1: FWHM resolution (μm) in radial direction for the FBP, the analytical FDR, deconvolution and the PSF-based reconstruction for four fluorescent beads. The errors indicate 95 % confidence intervals.

Method	Direction	Bead			
		1	2	3	4
FBP	Radial	27.4 ± 0.3	8.9 ± 0.1	10.8 ± 0.1	8.3 ± 0.1
	Tangential	57.1 ± 0.6	17.3 ± 0.3	42.6 ± 0.3	35.4 ± 0.5
FDR	Radial	25.1 ± 0.4	5.1 ± 0.1	8.48 ± 0.5	6.975 ± 0.1
	Tangential	60.9 ± 1.2	18.2 ± 0.5	41.5 ± 0.6	36.8 ± 0.9
Deconvolution	Radial	7.5 ± 0.1	3.8 ± 0.1	5.9 ± 0.1	3.8 ± 0.1
	Tangential	23.3 ± 0.3	7.7 ± 0.2	10.2 ± 0.1	8.4 ± 0.1
PSF-based	Radial	19.1 ± 0.2	7.2 ± 0.2	8.5 ± 0.1	6.4 ± 0.1
	Tangential	33.8 ± 0.4	10.1 ± 0.3	25.4 ± 0.3	24.3 ± 0.4

reconstructed with all four methods. The lowest sharpness is given by the FBP with a value of 0.05. The PSF-based reconstruction has a value of 0.0794. The deconvolution shows a sharpness value of 0.18 and the FDR has a sharpness value of 0.19. For all methods the SNR of the beads are quite similar. The PSF-based method has an SNR of 29.9. The SNR of the FDR method is 29.2 dB, the FBP of 32.6 dB and the deconvolution has the highest SNR with 35.2 dB.

A second comparison of the reconstruction algorithms is done using OPT imaging of a 10 days old transgenic zebrafish larva to illustrate the performance on a biological sample. The zebrafish cellular membranes are labeled with green fluorescent protein. The zebrafish larva is euthanized in ice water at the Erasmus Medical Center, Rotterdam according to animal welfare regulations. Animal experiments are approved by the Animal Experimentation Committee of the Erasmus MC, Rotterdam.
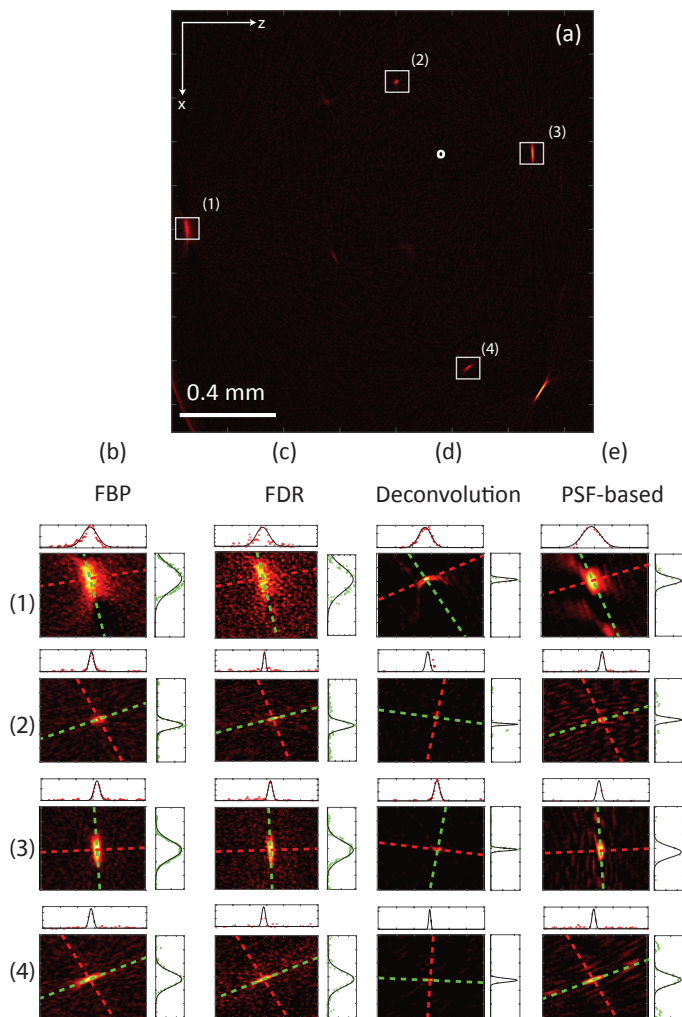
Figure 5.5: Reconstructions using FBP, FDR, deconvolution and PSF-based reconstruction for a single averaged sinogram in the x-z plane. The dash lines indicates the Gaussian fit in radial (red) and tangential direction (green) of fluorescent beads. (a) FBP image reconstruction. (b) Zoom in on individual beads in (a). (c) FDR reconstruction. (d) Image deconvolution. (e) PSF-based reconstruction.

The zebrafish is embedded in agarose and mounted in our OPT system [10]. The same experimental parameters are used as for the fluorescent bead data, however the NA of the system is 0.027, which is lower than for the fluorescent beads. For the zebrafish imaging a total of 1691 sinograms are acquired covering a distance of 6.5 mm along the rotation axis. For all 1691 slices, the tomographic image is reconstructed using FBP, FDR, deconvolution and the PSF-based approach (no slice averaging). The measured data is pre-processed as described in [11]. Furthermore, the result of the FDR reconstruction is masked for visualization purposes by the average mask used for the SNR estimation.

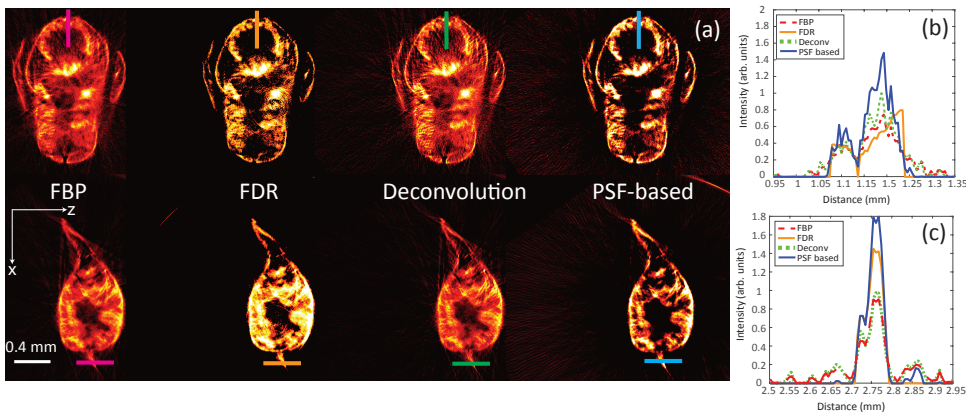A qualitative comparisons of a transversal slices through the zebrafish belly

Figure 5.6: (a) OPT image reconstructions of a single transverse slice of the zebrafish with the four reconstruction techniques, as indicated. (b) Cross-section of the reconstructed intensity in the tangential direction through the zebrafish belly, and (c) cross-section in radial direction through the zebrafish tail.

and tail is shown in Fig. 5.6 for the four different reconstruction techniques. Compared to FBP, deconvolution shows a small improvement in intensity and sharpness. The FDR has a much higher contrast and shows less artifacts in between the important biological structures. The PSF-based reconstruction shows the highest intensity and the least artifacts. Figure 5.6 (b) and (c), shows cross-sections through parts of the zebrafish belly and tail from which similar conclusions can be drawn.

A comparison of a coronal slice of the zebrafish reconstructed with the different algorithms is shown in Fig. 5.7 (center). For this slice, a similar conclusion can be drawn as for the transversal slice. Only visually, deconvolution seems to perform better than the FDR.

Quantitative comparison of the SNR along the length of the zebrafish shows, see Fig. 5.7 (left), that FBP has the lowest SNR. The deconvolution method and

the FDR have almost the same SNR, and the PSF-based reconstruction has the highest SNR, which is almost 10 dB better than the other reconstruction techniques. The sharpness of the image shows a similar behavior, shown in Fig. 5.7 (right). In general, the FDR and the FBP have the lowest sharpness value. The sharpness of the deconvolution method is higher and the PSF-based reconstruction approach yields the highest sharpness value. The jump in SNR and sharpness at slice 580 is due to the transition between the tail and the main body of the fish, where two datasets were fused.
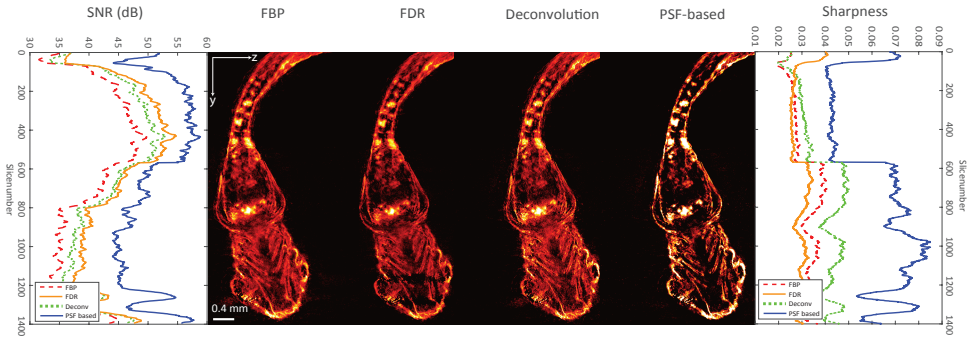

Figure 5.7: Blind image quality comparison of the different reconstruction algorithms applied to OPT zebrafish imaging. (left) Signal-to-noise ratio versus slice number. (center) A single coronal slice through the zebrafish reconstructed with the four different reconstruction algorithms. The different reconstruction methods are indicated in the legend. (right) Sharpness versus slice number.

5.5. Discussion

We compare three different state-of-the-art tomographic reconstruction methods that reduce the space-variant tangential blurring introduced by the optical imaging system with the classical FBP. We applied the algorithms to simulated data and experimental data of fluorescent beads and a zebrafish larva.

The deconvolution and PSF-based method give the best reconstruction results on simulated point source data. Especially for high NA imaging systems they perform better than FDR. We attribute this to the fact that the FDR inverse filter is an approximation that is only exact if the OTF of the imaging system varies slowly over the rotation angle [8]. For this condition the stationary phase approximation holds and a simple expression for the inverse filter can be derived. Especially, for high NA optical imaging systems this condition is not met. Consequently, the derived FDR filter is incorrect. Furthermore, in case of noisy data, the FDR filter in the Fourier domain has regions, where a division is per-

formed by values close to zero. This leads to an amplification of the noise, which is a common problem in inverse filtering [18]. If further regularization of the FDR is applied we expect that the reconstruction result can be improved. Another improvement can be achieved by additional filtering of the sinogram, for example by a Wiener filter, which can reduce noise amplification of the inverse filter [9]. The PSF-based reconstruction is regularized indirectly by termination of the reconstruction after the most optimal number of iterations. Hence, it is therefore more robust to noise than the conventional FDR. Additional regularization of PSF-based reconstruction, such as Tikhonov or total variation minimization, could lead to less noise amplification and faster convergence. In that case, we expect that the absolute error for the PSF-based approach would remain constant after reaching the minimum reconstruction error.

The experimental data of the fluorescent beads demonstrates that the deconvolution algorithm shows the best performance for sparse and low SNR objects. Since the optimization landscape of the PSF-based approach for sparse and low SNR objects is very flat and noisy, many iterations are necessary to find a good and improved solution. Consequently, if the SNR would be higher for the bead data, the PSF-based method should be able to reduce the blurring to a similar level as deconvolution in a more useful time-frame, i.e., in less iterations. To enhance the convergence speed for sparse objects, more prior information can be included in the reconstruction, for example an initial guess that is close to the real solution could lead to better reconstruction results.

For extended and non-sparse objects, such as the zebrafish larva, the PSF-based algorithm gives the best results, followed by the deconvolution approach. We attribute the good performance of the PSF-based algorithm to the fact that the intensities coming from an entire Gaussian shaped region is correctly attributed to the measured projections. Hence, signal inconsistencies with the FBP reconstruction are removed resulting in higher peak signals and a lower (noisy) background. Since for non-sparse objects the total object signal is higher we observe fast convergence to the optimal result.

Obviously, analytical methods such as FBP, FDR, and deconvolution require little computation time. Considering potential improvements in computer power and improved coding of the algorithms we have focused on the obtained image quality and not considered reconstruction run time in our comparison of the different algorithms. However, for applications that require fast image reconstructions, a choice may be made for faster methods such as FBP, FDR or deconvolution at the expense of a lower image quality. Moreover, for the PSF-based reconstruction, the user needs to make a few choices such as the maximum number of iterations and the tolerance of the method to obtain optimal results. Although, we choose the number of iterations after visual inspection, the selection

of the maximum number of iterations can be automated during the reconstruction process using the NR-IQA image quality metrics presented here.

In this work we focused on the image quality improvement by of tangential and radial blurring in OPT image reconstruction. The image quality is defined by the FWHM of point-like objects as well as the SNR and a sharpness metric. Multiple factors influence which reconstruction technique performed best, such as sparsity in the image domain, the NA of the imaging lens, and the SNR of the imaged object. As a recommendation, we advise to reconstruct sparse objects in almost all cases with deconvolution. In cases where the PSF cannot be described by a simple analytical expression we recommend the PSF-based reconstruction, which gives similar results for high SNR data. For low NA tomographic imaging of non-sparse objects we recommend the PSF-based reconstruction, as it gives superior image quality.

5.6. Conclusion
In this paper, we compared various tomographic image reconstruction techniques that take the PSF into account. For high SNR and non-sparse objects the PSF-based reconstruction yields superior performance. For sparse objects, deconvolution shows the best performance.

References

[1] E. Wolf, "Three-dimensional structure determination of semi-transparent objects from holographic data," Opt. Commun., vol. 1, no. 4, pp. 153 – 156 (1969).

[2] J. Sharpe, U. Ahlgren, P. Perry, B. Hill, A. Ross, J. Hecksher-Sørensen, R. Baldock, and D. Davidson, "Optical projection tomography as a tool for 3D microscopy and gene expression studies," Science, vol. 296, no. 5567, pp. 541–545 (2002).

[3] A. C. Kak and M. Slaney, *Principles of computerized tomographic imaging,* IEEE Press (1988).

[4] E. Rapisarda, V. Bettinardi, K. Thielemans, and M. C. Gilardi, "Image-based point spread function implementation in a fully 3D OSEM reconstruction algorithm for PET," Phys. Med. Biol., vol. 55, no. 14, pp. 4131–4151 (2010).

[5] R. Formiconi, A. Pupi, and A. Passeri, "Compensation of spatial system response in SPECT with conjugate gradient reconstruction technique," Phys. Med. Biol., vol. 34, no. 1, pp. 68–84 (1989).

[6] Z. Chen and R. Ning, "Three-dimensional point spread function measurement of cone-beam computed tomography system by iterative edge-blurring algorithm," Phys. Med. Biol., vol. 49, no. 10, pp. 1865–1880 (2004).

[7] B. Recur, J. P. Guillet, I. Manek-Hönninger, J. C. Delagnes, W. Benharbone, P. Desbarats, J. P. Domenger, L. Canioni, and P. Mounaix, "Propagation beam consideration for 3D THz computed tomography," Opt. Express, vol. 20, no. 6, pp. 5817–5829 (2012).

[8] W. Xia, R. M. Lewitt, and P. R. Edholm, "Fourier correction for spatially variant collimator blurring in SPECT," IEEE Trans. Med. Imaging, vol. 14, no. 1, pp. 100-115 (1995).

[9] J. R. Walls, J. G. Sled, and J. Sharp, "Resolution improvement in emission optical projection tomography," Phys. Med. Biol., vol. 52, no. 10, pp. 2775–90. (2007).

[10] J. van der Horst and J. Kalkman, "Image resolution and deconvolution in optical tomography," Opt. Express, vol. 24, no. 21, pp. 24460–24472 (2016).

[11] A. K. Trull, J. van der Horst, W. J. Palenstijn, L. J. van Vliet, T. van Leeuwen, and J. Kalkman, "Point spread function based image reconstruction in optical projection tomography," Phys. Med. Biol., vol. 62, no. 19, pp. 7784–7797 (2017).

[12] J. Radon and P. Parks, "On the determination of functions from their integral values along certain manifolds," IEEE Trans. Med. Imaging, vol. 4, pp. 170 – 176 (1986). Translation of the original paper by Johann Radon 1917.

[13] S. J. Glick, B. C. Penny, M. A. King, and C. L. Byrne, "Noniterative compensation for the distance-dependent detector response and photon attenuation in spect imaging," IEEE Trans. Med. Imaging, vol. 13, no. 2, pp. 363–74 (1994).

[14] R. M. Lewitt, P. R. Edholm, and W. Xia, "Fourier method for correction of depth-dependent collimator blurring," Proc. SPIE, vol. 1092, pp. 232–243 (1989).

[15] Z.Wang and A. Bovik, *Modern image quality assessment,* San Rafael, C.A.: Morgan and Claypool, Academic Press, pp. 1–15 (2006).

[16] R. Gonzalez and R. Woods, *Digital image processing,* Pearson (2008).

[17] K. De and V. Masilamani, "Image sharpness measure for blurred images in frequency domain," Procedia Eng., vol. 64, pp. 149-158 (2013)

[18] B. Jahne, *Computer vision and applications: A guide for students and practitioners,* Academic Press (2000).

Chapter 6

3D PSF-based image reconstruction in optical tomography

In this chapter an extension of the two-dimensional point spread function (PSF) based reconstruction algorithm of Chapter 4 [1] to three dimensions is presented. We compare in simulations the filtered back projection, and the 2D/3D PSF-based reconstructions with each other. As a proof of principle, the 3D PSF-based algorithm is applied to high-resolution emission optical projection tomography imaging data of a zebrafish larva. We show that the 3D PSF-based reconstruction, when properly initialized, gives an improved signal-to-background and image quality compared to the 2D PSF-based reconstruction.

6.1. Introduction

Optical imaging is an important modality for pre-clinical screening of cells and small animals [2, 3]. Various pre-clinical optical imaging techniques are available. Optical coherence tomography (OCT) is a highly successful optical tomographic technique based on interferometric imaging of the optical back-scattering tissue. Optical projection tomography (OPT) [4] is a high-resolution optical imaging technique in which the sample is optically cleared to reduce the scattering of the tissue.

In X-ray CT, straight ray-like propagation enables the perfect selection of individual lines and slices. However, in optical tomography, imaging is, due to diffraction, inherently a 3D process. In this case, the signal processing and image reconstruction need to be performed in 3D. However, in general the 3D imaging process is difficult to implement in the reconstruction and usually 2D reconstructions are stacked onto each other to create a 3D image. For OPT, various 2D image processing methods were developed to correct for the effect of the point spread function on the reconstructed image [1, 5–8]. The effect of the 2D point spread function is visible in a radial and tangential blurring whenfiltered back projection (FBP) is used for reconstruction. The further an object is away from the center of rotation the higher is the amount of radial and tangential blurring of the object. However, none of these techniques has been implemented in 3D.

Here an extension of the two-dimensional point spread function (PSF) based algorithm of Chapter 4 [1] to three dimensions is presented.

6.2. Theory

In optical projection tomography (OPT), the goal is to determine the spatial distribution of absorption or emission strength of an object $f(x, y, z)$ from its projections. In emission OPT, the object is assumed to be homogeneously illuminated with light from the excitation source resulting in an excitation rate that is constant over the object f. A small fraction of the excitation light is absorbed and emitted isotropically. Hence, it is assumed that variations in local emission strength are caused by variations in fluorophore concentration only.

Projections of the optical emission are made by lenses that image light from the sample onto the detector. As a result, the image of a point source on the detector is blurred by the optical point spread function (PSF). The three-dimensional Gaussian PSF is defined as

$$|h(x, y, z)|^2 = \left| \frac{1}{\sqrt{1 + \left(\frac{z}{z_R}\right)^2}} \exp\left(-\frac{x^2 + y^2}{w_0^2 \left(1 + \left(\frac{z}{z_R}\right)^2\right)}\right) \right|^2, \tag{6.1}$$

where $z_R = \pi w_0^2 / \lambda$ is the Rayleigh length (half the depth of focus). The numerical aperture is given by NA $= w_0 / z_R$. Following the derivation given in [1], the measured projections for emission OPT are given as

$$p(s_x, s_y, \theta) = \iiint\limits_{-\infty}^{\infty} f[(x - s_x)\cos\theta + z\sin\theta, y - s_y, (x - s_x)\sin\theta - z\cos\theta]$$

$$\times |h(x, y, z)|^2 \, dx \, dy \, dz, \tag{6.2}$$

where $|h(x, y, z)|^2$ denotes the PSF, f denotes the object, s_x, s_y describes the shift of the object in the x and y direction and $\theta \in [0, 2\pi]$ is the rotation angle.

In a 2D description, the sample is assumed to vary only slowly in the y direction and the 3D integral becomes a 2D integration over the object [1, 8]. This is indicated in Fig. 6.1 for a PSF where the center of rotation is imaged onto the detector showing the 2D object integration area and 3D object integration volume.

The projection data $p(s, \theta)$ is not measured in a continuous way, as defined by Eq. 6.2, but is sampled at discrete positions for a finite set of angles. The projection of Eq. 6.2, $p(s_x, s_y, \theta)$, is limited to a finite integration area D given by $D \in [-l/2, l/2, l/2)]$ for offsets $s_x, s_y \in [-l/2, l/2]$ and l is the size of the field of view. The projection is then represented by a matrix multiplication with the
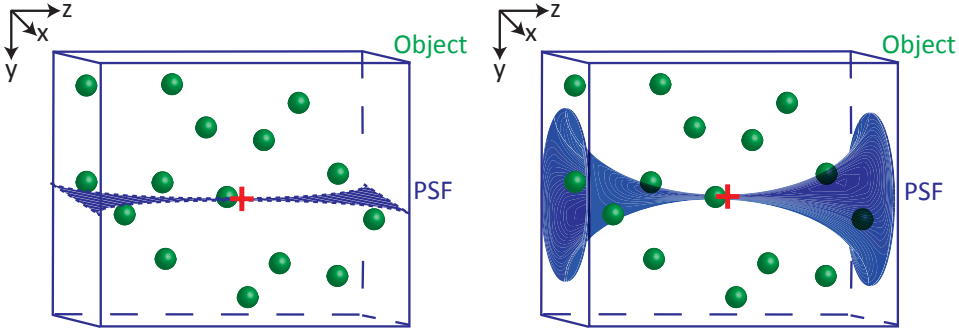
Figure 6.1: Illustration of the influence of the 2D PSF (left) and 3D PSF (right) on the reconstructed image as a beam-intensity weighted integration over an area or a volume of the object. The center of rotation is indicated by the red +.

object f discretized by sampling $f(x, y, z)$ on a regular cell-centered grid, within the cubic object domain D^3 at locations x_i, y_i, z_j, with $i = 1, 2, \ldots, n$, $j = 1, 2, \ldots, n$ where n is the number of pixels in each direction of the object and equal to the number of lateral pixels of the square detector. This leads to an image matrix of $f(x_i, y_i, z_i) \in \mathbb{R}^{n \times n \times n}$, which is stacked in a vector $\mathbf{f} \in \mathbb{R}^{n^3}$. The convolution of Eq. 6.2 is discretized into a geometry matrix $\mathbf{A} \in \mathbb{R}^{m \times n \times n, n^3}$, with m the number of projection angles. The acquisition domain of the measured projections are the set of samples (s_x^i, s_y^j, θ_k), with $k = 1, 2, \ldots, m$. The discrete projections $p(s_x^i, s_y^j, \theta_k) \in \mathbb{R}^{n,n,m}$ are stacked into a vector $\mathbf{p} \in \mathbb{R}^{n \times n \times m, 1}$.

After discretization, the object $\mathbf{f}$ can be reconstructed by finding a solution to the optimization problem

$$\underset{\mathbf{f}}{\text{argmin}} \quad \frac{1}{2} \|\mathbf{A} \cdot \mathbf{f} - \mathbf{p}\|_2^2, \tag{6.3}$$

where $\|\cdot\|_2$ denotes the Euclidean norm. Equation 6.3 can be solved using a least-squares optimization method based on conjugate gradients.

6.3. Methods

The calculations are performed on a high-performance computer with two Intel(R) Xeon(R) Processors (E5-2698 v4@2.2GHz, 50MB Cache and 20 cores), 256 GB installed memory and a 64-bit operating system. The most important parameter of the high-performance computer is the size of the memory as a large memory is required to store the entire reconstructed volume and all the measurements. The data are processed using software written in the commercial software package MATLAB (Mathworks, R2015a).

The algorithm presented in Chapter 4 [1] is extended to three-dimensions. For the optimization of Eq. 6.3 the MATLAB function *lsqr* is used. The input parameters are the projection data $p(s_x, s_y, \theta)$ and the beam parameters w_0 and z_R. An initial guess of every slice is either a zero image input or the image that resulted by the 2D PSF-based reconstruction method. Instead of requiring a pre-computed version of **A**, the MATLAB function *lsqr* allows providing a routine that evaluates multiplication by **A** and its transpose for every angle individually. Here, multiplication by **A** corresponds to (PSF-based) forward projection of an image in object space, and multiplication by the transpose of **A** corresponds to (PSF-based) back-projection of a sinogram onto an image in object space. A flow diagram for calculating the forward and backward projection and the 3D PSF-based reconstruction is shown in Fig. 6.2.The reconstruction algorithm uses the built-in MATLAB function *imrotate* with bilinear interpolation to obtain the object at different angles. In the forward direction, for every individual angle, the PSF is translated over the sample, so the forward model for a projection has the structure of a two-dimensional convolution in the lateral x and y directions. The convolution is implemented by a multiplication of the 2D Fourier transform of every object slice (x-y place) with the Fourier transform of the PSF in that plane. This is followed by an inverse Fourier transformation. Subsequently, a sum is taken in the propagation direction z. After the forward projection, the backward projection is calculated using the adjoint/transpose variants of these steps described above in reverse order. We zero-pad the sinogram to twice its size in both lateral directions to avoid aliasing.

Since no reference image is available for experimental data of spatially extended objects, a no-reference or blind image quality assessment (NR-IQA) is used to compare the quality of the different reconstruction results. In our comparison, we use the signal-to-noise ratio (SNR) and the sharpness provided by NR-IQA to assess the quality of the reconstructed images. More details on NR-IQA can be found in Chapter 5 [9].

6.4. Results

6.4.1. OPT reconstruction simulations

A synthetic 3D object is generated that consists of spherical objects located at different radial and axial positions, shown in Fig 6.3. For every angle the object is convolved with a three-dimensional PSF with $\lambda = 999$ nm and a beam waist of $w_0 = 6$ μm (Rayleigh length $z_R = 113.21$ μm), with the PSF and the center of the object on the rotation axis (center of the object in focus on the detector). The resulting blurred sinogram is used for the reconstruction per slice using FBP and 2D PSF-based reconstruction, and as a complete dataset for the 3D PSF-based re-
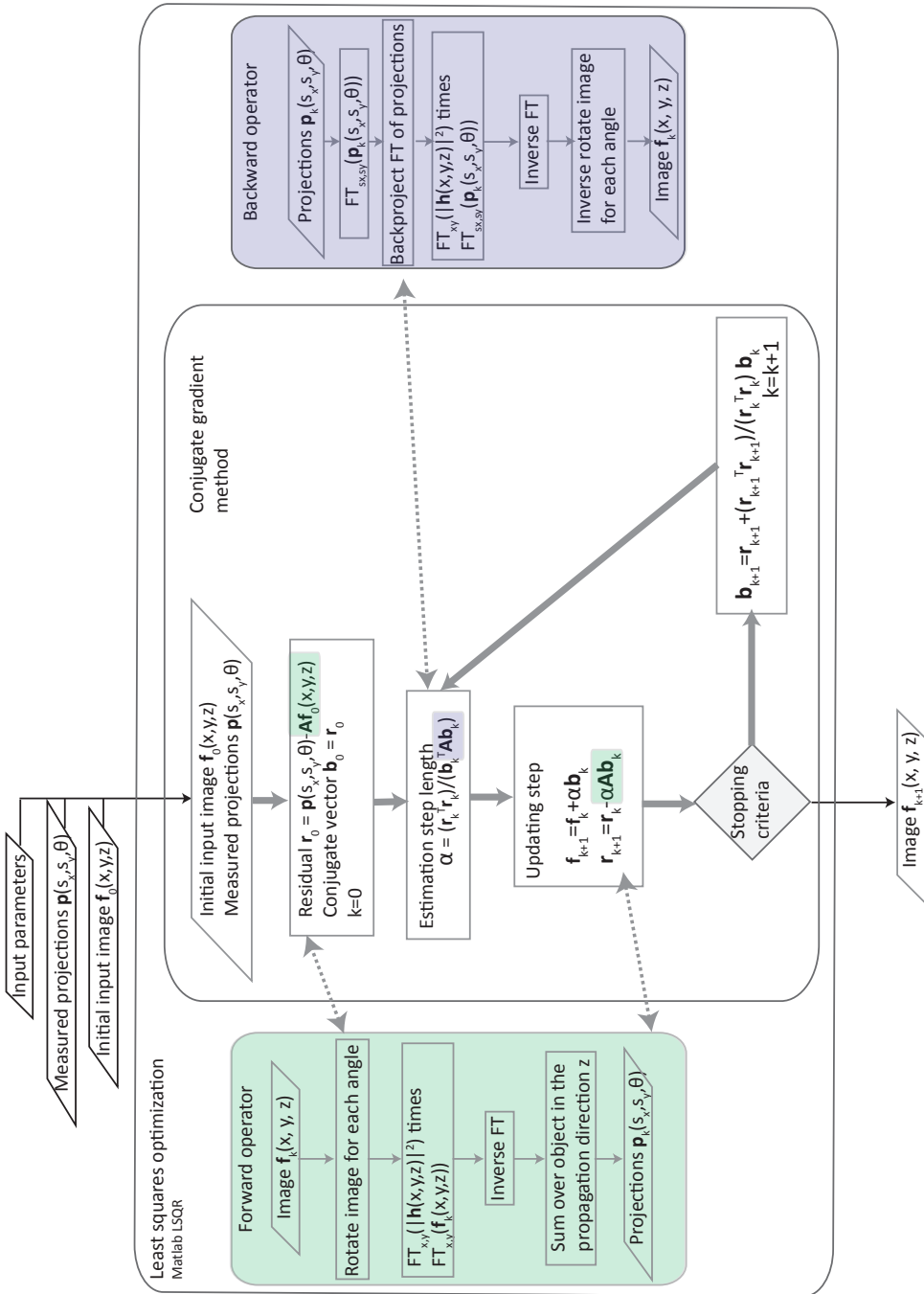
Figure 6.2: Flow diagram of the 3D PSF-based tomographic reconstruction algorithm. FT denotes 2D Fourier transformation.

construction. The original object is shown in the first row of Fig. 6.3. The second row of Fig. 6.3 shows the intensity projection in the axial and transverse direction of the FBP reconstruction. The FBP performs a two-dimensional reconstruction
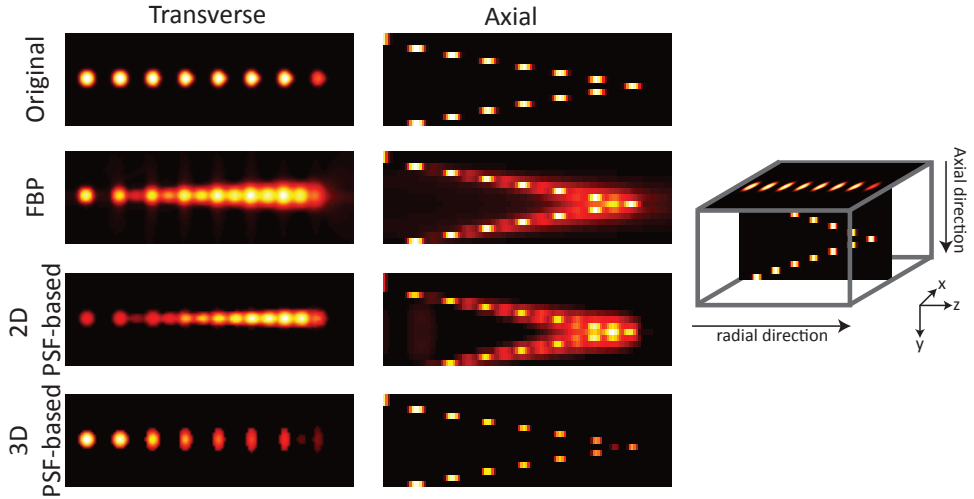

Figure 6.3: Transverse cross-sections and axial projections of the original input image and the reconstructions obtained by FBP, 2D PSF-based reconstruction, and 3D PSF-based reconstruction. The axial image shows a projection of the spherical objects over the slices.

and does not include the three-dimensional shape of the PSF. This leads to a radial and tangential blurring of the spherical objects and an axial blurring over the slices. The reconstruction result of the 2D PSF-based reconstruction is shown in the third row of Fig. 6.3. A reduction of the radial and tangential blurring is visible. However, in the axial direction the blurring is still strong as the 2D PSF-based reconstruction method does not correct for blurring in the axial direction. The best result is achieved by applying the 3D PSF-based reconstruction algorithm. In this case the blurring in the transverse plane and along the axial direction is fully removed.

6.4.2. Zebrafish larva OPT image reconstruction

The 3D PSF-based reconstruction is applied to an OPT scan of a 10 days old transgenic zebrafish larva in which the zebrafish cellular membranes are labeled with green fluorescent protein. The zebrafish larva is euthanized in ice water at the Erasmus Medical Center, Rotterdam according to animal welfare regulations. Animal experiments are approved by the Animal Experimentation Committee of the Erasmus MC, Rotterdam.

The zebrafish is mounted in agarose in our OPT system. The zebrafish dataset

has a total number of 1691 slices covering a distance of 6.5 mm along the rotation axis. Due to the large memory and calculation time for the 3D-PSF-based reconstruction, only a subset of 300 slices is taken from the dataset of the lower part of the zebrafish. The imaging system has an NA= 0.027 and a beam waist of $w_0 = 6$ µm, which leads to a Rayleigh length of $z_R = 222$ µm. More information on the experimental setup is given by [8]. The intensity of the reconstructed data is pre-processed and scaled as described in [1].

The reconstruction results are shown in Fig. 6.4. Figure 6.4 (a) shows the re-
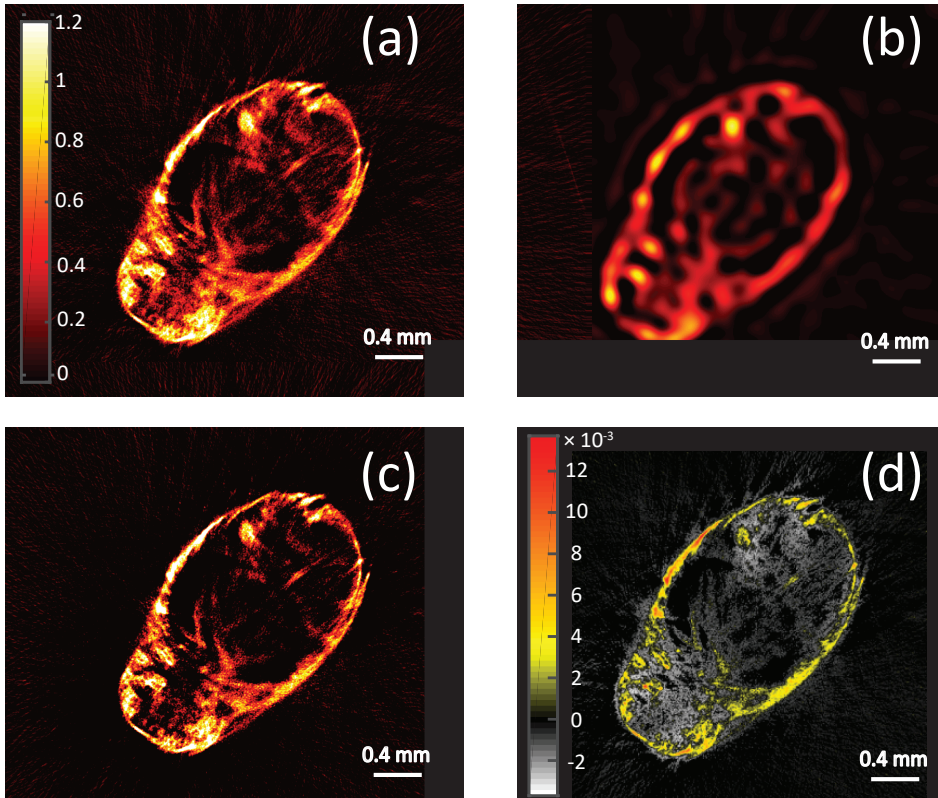
Figure 6.4: Reconstruction results of the 2D and 3D PSF-based reconstructions applied to a zebrafish larva. (a) 2D PSF-based reconstruction result after 2 iterations. (b) 3D PSF-based reconstruction result after 80 iterations with zero image as initialization. (c) 3D PSF-based reconstruction with 2D PSF-based reconstruction as initialization after 5 iterations. (d) Difference image computed from (c) minus (a). (b) and (c) have the same intensity scale bars as (a).

sult of the 2D PSF-based reconstruction result after 2 iterations. Figure 6.4 (b) shows the 3D PSF-based reconstruction result with a zero image as input after 80 iterations. No significant improvement was observed in the image quality in

the last 10 iterations. Clearly, the image quality is less than the result of the 2D PSF-based reconstruction. Figure 6.4 (c) shows the 3D PSF-based reconstruction result using the 2D PSF-based reconstruction as input after 5 iterations, after which a sharp image was observed. The 3D PSF-based reconstructed Image is sharper and has a significantly improved signal to background compared to the result of the 2D PSF-based reconstruction. This is quantified with the difference image between the results of the 2D and the 3D PSF-based reconstruction, 6.3 (c)-(a), which is shown in (d). From the difference image it can be observed that the 3D PSF-based reconstruction method has a higher signal intensity at the edge and a lower intensity at the center. For the 3D PSF-based method initialized with a zero input image no improvement in the image quality is observed after 80 iterations. Small differences between the result of the iterations are observed, but no convergence to useful result is observed. We attribute this to the presence of a flat optimization landscape. However, convergence to an improved image is obtained in a few iterations if an initial solution of the object that is close to the optimal solution is provided. We attribute the bad result of the 3D PSF-based reconstruction, when a zero input image is used, to the presence of a very flat and noisy optimization landscape and/or that the algorithm ends in a local minimum. Furthermore, a poor reconstruction result can be assigned to a properly initialization with was choses far away from the optimum solution. When properly initialized close to the optimum, convergence to an improved image is obtained in a few iterations.

The reconstruction time of the 3D PSF-based reconstruction is 11.5 hours for one iteration of the dataset consisting of $950 \times 950 \times 300$ voxels. This corresponds to a reconstruction time of 2.5 min per slice per iteration, which is similar to the reconstruction time for the 2D PSF-based reconstruction of 2 min per slice per iteration. Hence, the 3D implementation demonstrated here does not add significantly more calculation time to the reconstruction process.

A comparison of a coronal slice of the zebrafish reconstructed with the different reconstruction algorithms is shown in Fig. 6.5 (center). The quantitative comparison of the 2D and 3D PSF-based reconstructions are determined with NR-IQA SNR and sharpness estimation on each slice individually, as shown in Fig. 6.5 (top) and (bottom). The FBP has the lowest SNR and sharpness values for all slices. The 3D PSF-based reconstruction performs best for both the SNR and the sharpness for all slices. The SNR of the 3D approach is almost 20 dB higher than the 2D reconstruction technique. Furthermore, the sharpness of the 3D approach is almost twice as high compared to the 2D PSF-based approach. Both metrics demonstrate the superior performance of the 3D tomographic reconstruction algorithms presented here.
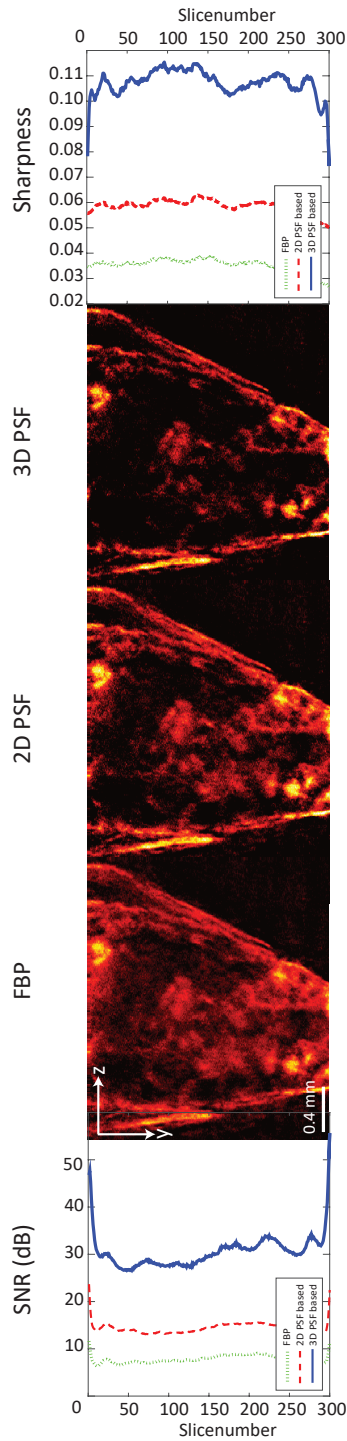
Figure 6.5: Blind image quality comparison of the two reconstruction algorithms. From top to bottom: Signal to noise ratio (dB) versus slice number, a coronal slice through the zebrafish reconstructed with FBP, the 2D PSF-based reconstruction, 3D PSF-based reconstruction, and sharpness versus slice number. The different reconstruction methods are indicated in the legend.

6.5. Discussion and conclusion

We present a 3D extension of the 2D PSF-based reconstruction algorithm presented in chapter 4 [1]. This reconstruction technique is computationally, in memory and run time, very demanding. Moreover, it does not converge in a useful timeframe (< 100 iterations) to a better reconstruction result compared to the 2D PSF-based approach if a zero image is used as an initialization. The convergence speed of the 3D PSF-based reconstruction improves if the 2D PSF-based reconstruction is used as an input and for a zebrafish yields a sharp image in approximately 5 iterations. Moreover, this image is sharper than the 2D reconstructed image indicating the importance of fully accounting for the 3D imaging geometry in the reconstruction. Similar to the 2D PSF-based reconstructions the 3D PSF-based reconstruction is regularized indirectly by setting a limit on the number of iterations. It is potentially possible to improve the convergence of the 3D PSF-based algorithm by adding regularization to the optimization process. These regularizations could be based on Tikhonov or total variation regularization, which sets a penalty on the gradients in the reconstructed image. Alternatively, a non-negativity constraint can be implemented to prevent values smaller than zero in the reconstruction.

In summary, we showed, as a proof of concept, a full 3D PSF-based tomographic reconstruction. Albeit that the 3D algorithm is computationally expensive and memory demanding, it gives an improved signal-to-background and sharpness compared to FBD and 2D PSF-based reconstruction if the 2D PSF-based reconstruction result is used to initialize the optimization process.

References

[1] A. K. Trull, J. van der Horst, W. J. Palenstijn, L. J. van Vliet, T. van Leeuwen, and J. Kalkman, "Point spread function based image reconstruction in optical projection tomography," Phys. Med. and Biol., vol. 62, no. 19, pp. 7784-7797 (2017).

[2] J. Hickson, "Seminar article: In vivo optical imaging: Preclinical applications and considerations," Urol. Oncol., vol. 27, no. 2, pp. 295-7 (2009).

[3] *Advanced pre-clinical optical imaging,* Perkin Elmer product note, (2015).

[4] J. Sharpe, U. Ahlgren, P. Perry, B. Hill, A. Ross, J. Hecksher-Sørensen, R. Baldock, and D. Davidson, "Optical projection tomography as a tool for 3D microscopy and gene expression studies," Science, vol. 296, no. 5567, pp. 541–545 (2002).

[5] W. Xia, R. M. Lewitt, and P. R. Edholm, "Fourier correction for spatially variant collimator blurring in spect," IEEE Trans. Med. Imaging, vol. 14, no. 1, pp. 100-115 (1995).

[6] J. R. Walls, J. G. Sled, and J. Sharp, "Resolution improvement in emission optical projection tomography," Phys. Med. Biol., vol. 52, no. 10, pp. 2775–90 (2007).

[7] B. Recur, J. P. Guillet, I. Manek-Hönninger, J. C. Delagnes, W. Benharbone, P. Desbarats, J. P. Domenger, L. Canioni, and P. Mounaix, "Propagation beam consideration for 3D THz computed tomography," Opt. Express,vol. 20, no. 6, pp. 5817–5829, (2012).

[8] J. van der Horst and J. Kalkman, "Image resolution and deconvolution in optical tomography," Opt. Express, vol. 24, no. 21, pp. 24460–24472 (2016).

[9] A. K. Trull, J. van der Horst, L. J. van Vliet, T. van Leeuwen, and J. Kalkman, "Comparison of image reconstruction techniques for optical projection tomography," Appl. Opt., vol. 57, no. 8, pp. 1874-1882 (2018).

Chapter 7

Conclusion and outlook

This dissertation presents novel reconstruction methods for high-resolution tomographic imaging and characterization of highly scattering (thick) and transparent samples. The latter is achieved by quantification of optical material parameters for planar samples in transmission optical coherence tomography (OCT) and for three-dimensional objects with optical coherence projection tomography (OCPT). In the remainder of this chapter, we present the main conclusions and provide recommendations for future research. Thereby we focus is on improving the image and signal information content, image quality after tomographic reconstruction, imaging and reconstruction speed, and enabling subsequent image segmentation.

7.1. Optical signal processing for quantitative tomographic imaging

Estimation of optical material properties is important for assessing the condition, both structural and functional, of tissues and to monitor changes thereof. In Chapter 2, the modeling of the transmission optical coherence tomography (OCT) signal was presented. We presented how the group refractive index, group velocity dispersion, and optical attenuation for different types of materials can be computed from the measured interference signal. Experimentally, we obtained a good agreement for various materials between our estimates of group refractive index, group velocity dispersion, as well as the mean and wavenumber-resolved attenuation coefficient with values reported in the literature. In principle, all these properties could be used for optical tomography. However, since the recorded signal in transmission OCT can be small, and therefore noisy, tomographic reconstruction can be challenging.

A reliable measurement of the optical properties in transmission OCT is difficult, especially at the low light levels that predominantly occur at both edges of the source spectrum. In that case, noise becomes an important component in the detected interference pattern and strongly influences the outcome of the Hilbert transform and the estimations that are based on it. The effect of noise on the Hilbert transform is described in multiple publications. Liu and Groves

[1] presented various methods to perform envelope detection in combination with band-pass filtering of a noisy signal. They showed that median filtering can be used for envelope detection. They also showed that using the autocorrelation of the OCT signal, with a bandpass filter and 2-D median filter applied before and after the demodulation, performs better than Hilbert transform-based techniques, when a large amount of noise is present. With more accurate phase measurements, the group refractive index and group velocity dispersion (GVD) estimation potentially could be improved. Pavlicek [2] showed for uncorrelated signal noise that the noise in both the envelope and phase of the Hilbert transform are correlated, i.e., a small signal amplitude gives rise to a large phase noise. Therefore, a square-shaped source spectrum is favorable for estimation of the phase as well as GVD, which are based on a fit of the phase over the entire spectral bandwidth.

Besides noise, the use of a larger spectral bandwidth enables improved discrimination of ballistic light from scattered light, thereby improving refractive index and attenuation coefficient measurements in turbid media. This is especially useful when measuring in strongly scattering or thick samples.

Potentially, information about the sample, such as the scattering anisotropy, can be retrieved from the scattered light distribution, e.g., by fitting a light transport model to the optical path length distribution. However, this is challenging considering the complexity of the light transport model and the accurate incorporation of the beam geometry.

7.2. Tomographic image quality

Because of the shallow depth of focus of the optical imaging system, the use of standard filtered back projection in optical projection tomography causes space-variant tangential blurring that increases with increasing distance to the rotation axis. In Chapter 4, we present a least-squares optimization approach for the optical tomographic imaging problem, $||\mathbf{Af} - \mathbf{p}||_2^2$, which reduces the tangential blurring by incorporating the optical point spread function (PSF) in the tomographic reconstruction. Although this method gives good results, the convergence to the optimal solution can be rather slow.

For the PSF-based reconstruction, it can be noted that reduction of the tangential blurring is more difficult for high NA optical systems. We tested the PSF-based method on simulated data for various NAs and observed that it did not perform well for NAs > 0.1, i.e., significantly larger than the ones used in Chapter 4-6.

As we show in Chapter 5, this specifically can be a problem for sparse objects of low SNR that are acquired with high NA optics. A possible way to improve the

image quality is the addition of a regularization term to the optimization problem. When regularized, an extra term $+\lambda R(\mathbf{f})$ is added to the objective function $||\mathbf{Af} - \mathbf{p}||_2^2$, where $R(\mathbf{f})$ denotes the regularization operator and λ is a tuning parameter that can be varied in order to increase or decrease the regularization strength. Possible regularizers to the reconstruction can impose a non-negativity constraint on the solution or promote sparseness of the solution regularized by the l_1-norm of the object.

In our current implementation of the PSF-based tomographic image reconstruction, we assumed that the object does not influence the propagation direction of the light through the object. In general, this is not the case as refraction can cause rays to deflect from their trajectory. To incorporate these effects in image reconstruction, the reconstruction problem is reformulated into

$$||\mathbf{A}(\mathbf{f})\mathbf{f} - \mathbf{p}||_2^2, \qquad (7.1)$$

where $\mathbf{A}(\mathbf{f})$ describes a geometry matrix that depends on the optical parameter that is to be reconstructed. An algorithm taking into account ray refraction can work in the following way. First, the object $\mathbf{f_1}$ is reconstructed with $\mathbf{A}(\mathbf{f_0})$, where $\mathbf{f_0}$ is a homogeneous sample object. Second, a new geometry matrix $\mathbf{A}(\mathbf{f_1})$ is estimated from the reconstructed object $\mathbf{f_1}$ with $\mathbf{A}(\mathbf{f_1})$ describing the effect of ray refraction. Third, an improved estimate of the object is determined with the improved geometry matrix $\mathbf{A}(\mathbf{f_1})$. This process is iterated until convergence is reached.

The 2D PSF-based reconstruction was extended to include the three-dimensional shape of the focusing beam in the object. However, existing methods such as deconvolution and FDR (frequency-distant relationship) potentially also can be extended to three dimensions and a comparison of their performance in 3D, similar to the one presented in Chapter 6, would be of interest. Furthermore, for the PSF-based reconstruction it is relatively simple to change the beam shape, which means that it is possible to include PSFs for imaging systems with a large depth of focus such as astigmatic beams or Bessel beams. The PSF-based reconstruction algorithms also can be applied to imaging techniques where beam propagation deviates from the ideal straight ray. This is present in any tomographic technique where the wave nature of the used radiation plays an important role such as in Terahertz imaging and ultrasound imaging.

More recently, machine-learning techniques for 2D and 3D image reconstruction have been developed. For example, it has been shown that artificial neural networks (ANN) can be used to reconstruct the 3D refractive index of holographic optical phase microscopy images [3], where ANNs are used to reduce the effects of limited angle tomography ($\pm45°$ acquisition angles). Kamilow et al. [3] showed that the forward propagation and the backpropagation can be used to

construct a training set from which improved tomographic reconstructions can be obtained. Cierniak presented neural networks in the context of tomographic reconstructions from projections for parallel and fan-beam geometries [4]. He showed that instead of the conventional filtered backprojection a simple back-projection is performed with the filtering being performed using recurrent neural networks. Batenburg and Kosters [5] applied ANN to problems in real-time discrete tomography. They showed that neural networks are extremely fast, but that the training of the neural network itself can take a substantial amount of time. Potentially, in deep learning, the neural network could learn the geometry of the imaging system if sufficient imaging examples are included in the training data.

7.3. Imaging speed and reconstruction time

In Chapter 4, 5, and 6 we presented and compared various tomographic image reconstruction techniques. The challenge in image reconstruction is to reconstruct a high quality image or volume in a useful timeframe. Various parameters, such as the number of angles, number of pixels, signal to noise ratio, and stopping criteria, have an influence on the computation time of the reconstruction. Furthermore, depending on the type of image reconstruction algorithm the reconstruction time can vary significantly.

The reconstruction time for one slice using the 2D PSF-based algorithm is currently two minutes per iteration, which can be a severe drawback if these algorithms are used for high-throughput imaging. A way to reduce the reconstruction time is to choose fewer projection angles but distributed in a more optimal way over the entire acquisition range to improve the convergence of the reconstruction algorithm [6]. Since the measurements are redundant, especially for sparse objects, optimization-based approaches can be used to reconstruct an image also when fewer angles are used. When only a limited range of angles is sampled, so-called limited angle tomography, the data is incomplete and leads to artifacts in the reconstructed image. Due to the flexibility of the geometrical definition in the **A** matrix, the PSF-based reconstruction method can be modified with little ease to incorporate limited angle or random angle acquisition.

Figure 7.1 shows an example of the implementation of limited angle tomography on the Shepp-Logan phantom. Figure 7.1 (a) shows the reconstruction using all 360 projections measured at 1 degree interval. In Figure 7.1 (b) the object is reconstructed using only the first 90 projections. In this case strong streak artifacts and missing boundaries are visible, similar as described by [7]. An improved image can be achieved by ℓ_1 minimization, which employs prior knowledge regarding the sparseness of the underlying object. Thereby, the conventional minimization problem is reformulated to a linear programming problem
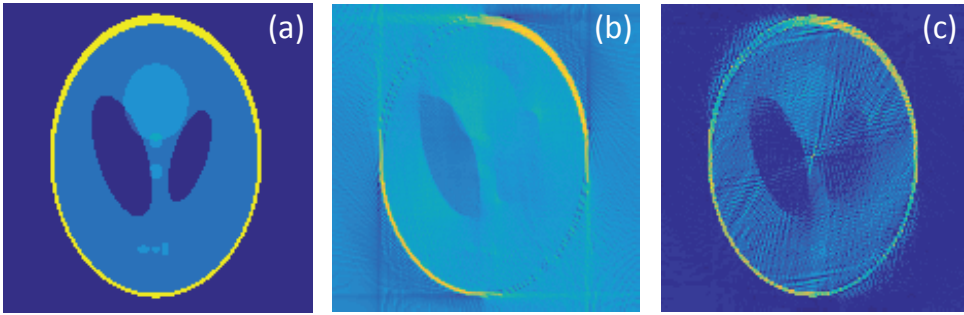
Figure 7.1: Limited angle tomography and reconstruction. (a) FBP reconstruction using 360 projections at 1 projection per degree, (b) FBP reconstruction using only the first 90 angles. (c) Reconstruction of the data in (b) after 30 iterations of the ℓ_1 minimization problem using the same framework as used for the PSF-based reconstruction,

$$\operatorname*{argmin}_{\mathbf{f}} \|\mathbf{f}\|_1 \text{ s.t. } \|\mathbf{A} \cdot \mathbf{f} - \mathbf{p}\|_2 < \epsilon. \tag{7.2}$$

The reconstruction result of this approach is shown Fig. 7.1 (c) and shows that a better result is achieved by reformulating the inverse problem to an ℓ_1 minimization problem.

In its current implementation, the PSF-based 2D and 3D reconstructions, presented in Chapter 4-6, are used without including any prior information or direct regularization. Improvement of the convergence for non-sparse data could be achieved by masking the data or by applying regularization methods. For example, for the sparse bead sample, sparsity promoting ℓ_1 norm regularization in the reconstruction can improve the reconstruction accuracy as well as the convergence rate as shown by Kim et al.[8]. Another improvement is to include the no-reference image quality assessment metrics, used in Chapter 4, as an automatic stopping criterion in the optimization approach. It may terminate the algorithm at the earliest time when the image quality exceeds a pre-defined threshold and may avoid overfitting to the noise in the data.

7.4. Image segmentation

In Chapter 3, segmentation techniques such as thresholding, manual delineation, k-means and region growing are used. Since the imaged objects are in 3D, extension of the segmentation algorithms to 3D potentially can improve the segmentation result. For example, a three-dimensional region growing algorithm would then also include the intensity differences along the rotation axis. The seed would then be placed in a three-dimensional space and not in each slice.

In order to avoid the introduction of errors in the reconstruction phase that will hinder subsequent segmentation, the image reconstruction and segmentation can be combined in a single step, with the potential for improved overall performance. An example how to combine segmentation and reconstruction was demonstrated for limited angle X-ray tomography by Yoon et al. [9]. The coupling between reconstruction and segmentation was done by alternatively performing a level set segmentation and image intensity updates of the reconstruction. Another combination of reconstruction and segmentation is introduced by Romanow [10]. He used the image segmentation as a smoother for the reconstruction, where the segmentation information is included by a hidden Markov field. The model assumes prior knowledge about the number of material classes and the hidden Markov field returns the pixel wise probability that a specific pixel belongs to a specific class. The segmentation is found by selecting the most probable class for each pixel. Combining reconstruction and segmentation could not only help to improve the segmentation, but also the reconstruction result. However, this approach is only useful in case the object has a discrete distribution of components [11].

7.5. Applications of the thesis work

For medical applications, the zebrafish is one of the most important models to study human diseases, such as cancer, Duchenne muscular dystrophy, and diabetes, and many other diseases [12, 13]. The methods and results, such as the zebrafish organ parameter estimation shown in Chapter 3, can lead to further insight in disease onset and progression, which potentially can lead to better treatment. For example, Wang et al. [14] showed that cancer alters the refractive index, which can be used as a marker for cancer diagnostics. Therefore, OCPT and tissue quantification techniques may enable the detailed study of cancer development in small animals. To even further improve the clinical relevance of optical tomography, the different optical modalities could be combined using registration and image fusion techniques. After registration, image fusion is then applied to map the different modalities in a single image frame. Possible combinations can be fluorescence OPT and OCPT or fluorescence OPT and OCT, to give combined structural and functional information about the tissue.

References

[1] P. Liu and R. M. Groves, "Signal processing in optical coherence tomography for aerospace material characterization," Opt. Eng., vol. 52, no. 9, pp. 033201 - 033207 (2013).

[2] P. Pavliček and V. Svak, "Noise properties of Hilbert transform evaluation," Meas. Sci. Technol., vol. 26, pp. 85207-85216 (2015).

[3] U. S. Kamilov, I. N. Papadopoulos, M. H. Shoreh, A. Goy, C. Vonesch, M. Unser, and D. Psaltis, "Learning approach to optical tomography," Optica, vol. 2, pp. 517–522, (2015).

[4] R. Cierniak, "Neural network algorithm for image reconstruction using the "grid-friendly" projections", Australas. Phys. Eng. Sci. Med., vol. 34, no. 375-390, (2011).

[5] K. J. Batenburg and W. Kosters, "A neural network approach to real-time discrete tomography", IWCIA 2006, pp. 389–403, (2006).

[6] W. Choi, Y. Fang-Yen, K. Badizadegan, S. Oh, N. Lue, R. R. Dasari, and M. S. Feld, "Tomographic phase microscopy," Nat. Methods, vol. 4, no. 9, pp. 717–9, (2007).

[7] J. Frikel and E. T. Quinto, "Characterization and reduction of artifacts in limited angle tomography", Inverse problems, vol. 29, no. 12, pp. 1-25 (2013).

[8] S.-J. Kim, K. Koh, M. Lustig, S. Boyd, and D. Gorinevsky, "An interior-point method for large-scale l_1-regularized least squares," IEEE J. Sel. Top. Signal Process., vol. 1, no. 4, pp. 606-617, (2007).

[9] S. Yoon, A. R. Pineda, and R. Fahrig, "Simultaneous segmentation and reconstruction: A level set method approach for limited view computed tomography", Med. Phys., vol. 37, no. 5, pp. 2329-40 (2010).

[10] M. Romanow, "Simultaneous reconstruction and segmentation with class-specific priors," PhD Thesis, Technical University of Denmark (2015).

[11] K. J. Batenburg and J. Sijbers, "DART: A practical and efficient reconstruction algorithm for discrete tomography," IEEE Trans. Image Process., vol. 20, no. 9, pp. 2542–53, (2011).

[12] "Why use zebrafish to study human diseases?," https://irp.nih.gov/blog/post/2016/08/why-use-zebrafish-to-study-human-diseases, downloaded 2016.

[13] "Why use the zebrafish in research?," https://www.yourgenome.org/facts/why-use-the-zebrafish-in-research, downloaded 2016.

[14] Z. Wang, K. Tangella, A. Balla, and G. Popescu, "Tissue refractive index as marker of disease," J. Biomed. Opt., vol. 16, no. 11, pp. 116017 - 116024, (2011).

Summary

Disease model systems, such as the zebrafish, play an important role in understanding the onset of diseases like cancer and monitor the efficacy of new drugs. In the past, non-invasive methods for screening, diagnostics and treatment monitoring were intrinsically from the outside. In the past decades, there has been a strong drive to look inside these model systems, which resulted in the development of many small animal tomographic imaging techniques. Due to the absence of ionizing radiation, high-resolution, and cost efficiency, optical tomography is a popular imaging technique to study disease model systems such as zebrafish. The main obstacles in obtaining high-resolution imaging suitable for tissue characterization are the scattering of light in tissue and diffraction of optical waves.

Scattering of light in tissue degrades the resolution of optical tomography systems, especially for thick samples. In this thesis, transmission optical coherence tomography (OCT) is used to select ballistic, non-scattered, from non-ballistic, scattered, light. We demonstrate that transmission optical coherence tomography is a versatile tool to measure optical properties of liquids, solids, and particle suspensions. The developed technique is used to perform quantitative optical tomography of the refractive index and attenuation coefficient. A good agreement is observed between our measurements and literature values for group refractive index, group velocity dispersion, and attenuation coefficient. Based on the tomographic reconstruction of transmission OCT measurements, the median attenuation coefficient, group refractive index and volumes of various organs of an adult zebrafish are segmented and quantified in optical coherence projection tomography reconstructions.

In optical tomography light is imaged by a lens onto the camera. Due to the focusing of light onto the camera, this light is collected non-uniformly along the propagation direction from the sample. Consequently, the straight-ray assumption as in standard (pre-) clinical X-ray CT reconstruction is violated. Reconstruction of optical tomography images with standard filtered back projection (FBP) causes radial blurring and tangential blurring that becomes stronger with increasing distance to the rotation axis. We present 2D and 3D tomographic reconstruction algorithms that include the point spread function (PSF) of the imaging system. For emission optical projection tomography, these methods show greatly reduced radial and tangential blurring over the entire field of view

and a significantly improved signal-to-noise ratio compared to FBP. The 3D PSF-based algorithm is evaluated using different initializations. When initialized with the 2D PSF-based reconstruction result, the 3D PSF-based reconstruction gives an improved signal-to-background and image quality in a useful timeframes.

Besides including the physical point spread function (PSF) in the 2D tomographic reconstruction, the effect of the PSF also can be reduced by deconvolution of the FBP reconstructed image or filtering the sinogram before FBP reconstruction. We compared the performance of these techniques with each other based on simulations and the signal-to-noise ratio and the sharpness in reconstructed fluorescent beads and zebrafish OPT images. We demonstrate that the sinogram filtering performs poorly on data acquired with high numerical aperture optical imaging systems. We show that the deconvolution technique performs best for highly sparse, low signal-to-noise ratio objects. The PSF-based reconstruction method is superior for non-sparse objects and data of high signal-to-noise ratio.

In this thesis, we developed novel algorithms for transmission OCT signal processing and PSF-based tomographic reconstruction. Our algorithms allow for high-resolution quantitative imaging in turbid media. These techniques can be used for quantitative optical imaging of disease model systems. Potentially this may lead to more insight in tissue development and disease onset, progression, and treatment.

Samenvatting

Ziektemodelsystemen, zoals de zebravis, spelen een belangrijke rol in het begrijpen van het begin van ziekten, zoals kanker, en het volgen van de werkzaamheid van nieuwe medicijnen. In het verleden waren niet-invasieve methoden voor screening, diagnostiek en behandelingsmonitoring intrinsiek van de buitenkant. In de afgelopen decennia is er een sterke beweging geweest om binnen in het modelsysteem te kijken, wat resulteerde in de ontwikkeling van verscheidene tomografische beeldvormingstechnieken voor kleine dieren. Als gevolg van de afwezigheid van ioniserende straling, hoge resolutie en kostenefficiëntie, is optische tomografie een populaire beeldvormingstechniek om ziektemodelsystemen zoals zebravissen te bestuderen. De belangrijkste hindernissen bij hoge resolutie beeldvorming die geschikt is voor weefselkarakterisering zijn de verstrooiing van licht in het weefsel en diffractie van de optische golven.

Verstrooiing van licht in weefsel verslechtert de resolutie van optische tomografiesystemen, in het bijzonder voor dikke stalen. In dit proefschrift wordt transmissie optische coherentie tomografie (OCT) gebruikt om ballistisch, niet-verstrooid, van niet-ballistisch, verstrooid, licht te scheiden. We demonstreren dat transmissie optische coherentie tomografie een veelzijdig hulpmiddel is om optische eigenschappen van vloeistoffen, vaste stoffen en deeltjessuspensies te meten. De ontwikkelde techniek wordt gebruikt om kwantitatieve optische tomografie van de brekingsindex en attenuatiecoëfficiënt uit te voeren. Een goede overeenstemming wordt waargenomen tussen onze metingen en literatuurwaarden voor groepsbrekingsindex, groepssnelheidsdispersie en attenuatie-coëfficiënt. Gebaseerd op tomografische reconstructie van transmissie OCT-metingen worden de mediane attenuatiecoëfficiënten en groepsbrekingsindices, en volumes van verschillende organen van een volwassen zebravis gesegmenteerd en gekwantificeerd.

In optische tomografie wordt licht door een lens op de camera afgebeeld. Vanwege het focusseren van het licht op de camera, wordt het licht niet-uniform verzameld langs de voortplantingsrichting van de optische straal staal. Bijgevolg wordt de rechte-straal-aanname zoals in standaard (pre-) klinische röntgen CT-reconstructie geschonden. Reconstructie van optische tomografiebeelden met standaard gefilterde terugprojectie (FBP) veroorzaakt radiale onscherpte en tangentiële onscherpte die sterker wordt met toenemende afstand tot de rotatieas. We presenteren 2D en 3D tomografische reconstructiealgoritmen die de

puntspreidingsfunctie (PSF) van het afbeeldingssysteem omvatten. Voor emissie-optische projectietomografie geven deze algoritmen sterk verminderde radiale en tangentiële onscherpte over het gehele blikveldveld en een significant verbeterde signaalruisverhouding vergeleken met FBP. Het op een 3D PSF gebaseerde algoritme wordt geëvalueerd met behulp van verschillende initialisaties. Wanneer geïnitialiseerd met het 2D PSF-gebaseerde reconstructieresultaat, geeft de 3D PSF-gebaseerde reconstructie een verbeterde signaal-tot-achtergrond verhouding en beeldkwaliteit berekend in een bruikbaar tijdspanne.

Naast het opnemen van de fysieke puntspreidingsfunctie (PSF) in de 2D tomografische reconstructie, kan het effect van de PSF ook worden verminderd door deconvolutie van het FBP gereconstrueerde beeld of filteren van het sinogram voor FBP-reconstructie. We vergeleken de prestaties van deze technieken met elkaar op basis van simulaties en de signaal-ruisverhouding en de scherpte in gereconstrueerde beelden van fluorescerende deeltjes en een zebravis. We tonen aan dat het sinogram-filteren slecht presteert op data die zijn verkregen met optische beeldvormingssystemen met hoge numerieke apertuur. We laten zien dat de deconvolutie-techniek het beste presteert voor zeer sparse, lage signaal-ruisverhouding objecten. De op de PSF gebaseerde reconstructiewerkwijze is superieur voor niet-sparse objecten en data met een hoge signaal-ruisverhouding.

In dit proefschrift hebben we nieuwe algoritmes ontwikkeld voor transmissie OCT-signaalverwerking en PSF-gebaseerde tomografische reconstructie. Onze algoritmen maken kwantitatieve beeldvorming met hoge resolutie mogelijk in troebele media. De technieken die in dit proefschrift zijn ontwikkeld, kunnen worden gebruikt voor kwantitatieve optische beeldvorming van ziektemodelsystemen. Dit kan mogelijk leiden tot meer inzicht in de ontwikkeling van weefsels en het begin, de progressie en de behandeling van ziektes.

List of Figures

List of Tables

Curriculum Vitæ

Anna Katharina Trull

10. January 1988   Born in Itzehoe, Germany

Education

Mar 2014 – Dec 2018	PhD, Topic: Image Reconstruction in Optical tomography Department of Imaging Physics, Delft University of Technology, The Netherlands
Oct 2011 – Sep 2013	M.Sc. Computational Life Science, Specialization: Image Processing, University of Lübeck, Germany
Aug - Dec 2012	Semester abroad, University of Bergen, Norway
Oct 2008 - Sep 2011	B.Sc. Computational Life Science, University of Lübeck, Germany
Aug 2008	German Secondary School Diploma (Abitur) Lichtenberg Gynmasium, Cuxhaven, Germany
Jun 2006	Canadian High School Diploma, Afnorth International School, Brunssum, The Netherlands

Work

since Mar 2018	Vision Engineer, Greefa, Tricht, The Netherlands
Mar 2014 - Feb 2018	Research assistant, Department of Imaging Physics, Quantitative Imaging Group Delft University of Technology, The Netherlands
Oct 2010 - Feb 2014	Teaching assistant for linear algebra and discrete structures, Institute of Mathematics and Image Computing, University of Lübeck, Germany
Oct 2009 - Aug 2010	Teaching assistant for the German mathematical Olympiad, Initiative of Mathematics, Student academy of the University of Lübeck, Germany

List of Publications

Journals articles

4. **J. van der Horst, A. K. Trull and J. Kalkman**, *Deep tissue label-free quantitative optical tomography'*, manuscript in preparation (2018)

3. **A. K. Trull, J. van der Horst, L. J. van Vliet, and J. Kalkman**, *Comparison of image reconstruction techniques in optical projection tomography*, Appl. Opt., vol. 57, no. 8, pp. 1874-1882 (2018)

2. **A. K. Trull, J. van der Horst, W. J. Palenstijn, L. J. van Vliet, T. van Leeuwen, and J. Kalkman**, *Point spread function based image reconstruction in optical projection tomography*, Phy. Med. and Bio., vol. 62, no. 19, pp. 7784 (2017)

1. **A. K. Trull, J. van der Horst, J. G. Bijster and J. Kalkman**, *Transmission optical coherence tomography based measurement of optical material properties* , Opt. Express, vol. 23, no. 26, pp. 33550-33563 (2015)

Conference contributions

5. **A. K. Trull**, *Point spread function based image reconstruction in optical projection tomography*, Equadiff 2017, Bratislava, Slovakia (2017)
(Invited Speaker)

4. **A. K. Trull, J. van der Horst, W. J. Palenstijn, L. J. van Vliet, T. van Leeuwen, and J. Kalkman**, *Point spread function based image reconstruction in optical projection tomography*, ECBO 2017, Munich, Germany (2017)
(Conference Paper)

3. **J. van der Horst, A. K. Trull, and J. Kalkman**, *Optical coherence computed tomography for quantitative 3D imaging of turbid media*, ECBO 2017, Munich, Germany (2017)
(Conference Paper)

2. **A. K. Trull**, *Optical Tomographic Image Reconstruction with Spatially Varying Point Spread Function*, Inverse Problems: Modeling and Simulation, Fethiye, Turkey (2016)
(Invited Speaker)

1. **A. K. Trull, J. van der Horst, J. G. Bijster and J. Kalkman**, *Transmission optical coherence tomography sensing*, Proc. SPIE 9899, Optical Sensing and Detection IV, Volume 9899 (2016)
(Conference Paper)

Poster contributions

11. **A. K. Trull, J. van der Horst and J. Kalkman**, *Point spread function based image reconstruction in optical projection tomography*, Science Day, Delft University of Technology, The Netherlands (2017)

10. **A. K. Trull and J. Kalkman**, *Quantitative Optical Tomography Image Reconstruction for High Numerical Aperture Lenses* , Orientatie op de Natuurkunde , Delft University of Technology, The Netherlands (2016)

9. **A. K. Trull and J. Kalkman**, *Quantitative Optical Tomography Image Reconstruction for High Numerical Aperture Lenses* , High-Definition-Tomography Days, Technical University of Denmark, Denmark (2016)

8. **A. K. Trull, J. van der Horst, L. van Opstal and J. Kalkman**, *Reconstruction in Optical Tomography*, Quantitative 3D X-Ray Imaging Workshop 2016, Leiden, The Netherlands (2016)

7. **A. K. Trull, J. van der Horst, L. van Opstal and J. Kalkman**, *Image Reconstruction in Optical Coherence Computed Tomography and Fluorescence Molecular Tomography*, International Workshop on Industrial Tomography 2015, Antwerp, Belgium (2015)

6. **J. van der Horst, A. K. Trull, L. van Opstal and J. Kalkman**, *Light Attenuation and Dispersion in Transmission Optical Coherence Tomography*, Imphys Day, Delft University of Technology, The Netherlands (2015)

5. **A. K. Trull, J. van der Horst, L. van Opstal and J. Kalkman**, *Image Reconstruction in Optical Coherence Computed Tomography and Fluorescence Molecular Tomography*, Imphys Day, Delft University of Technology, The Netherlands (2015)

4. **J. van der Horst, A. K. Trull and J. Kalkman**, *Light Attenuation and Dispersion in Transmission Optical Coherence Tomography* , International Graduate Summer School: Biophotonics, Island of Ven, Sweden (2015)

3. **A. K. Trull, J. van der Horst and J. Kalkman**, *Dispersion Quantification in Transmission Optical Coherence Tomography*, Inverse Problems in Wave Propagation, University of Bremen (2015)

2. **A. K. Trull and J. Kalkman**, *Modelling Fourier-Domain Low-Coherence Interferometry for Optical Tomography*, Imphys Day, Delft University of Technology, The Netherlands (2014)

1. **A. K. Trull, J. van der Horst and J. Kalkman**, *Zebrafish swim into a new light*, Bio-Day, Delft University of Technology, The Netherlands (2014)

Acknowledgement

The time and the way towards an academic title is a troublesome path, which is often combined with moments of doubt and uncertainty. But the path is also lined with moments of happiness and confidence. I am glad that I made it so far and that I was able to share these moments. However, I would also like to say, that I would not have come so far without the support of my colleagues, friends and my family.

First of all, I would like to thank my promoter Lucas and my co-promotor Jeroen for their support, discussions and comments. Thanks also go to Tristan and Willem Jan for their support, their comments and the projects we worked on together. It was great working with you. Furthermore, I would like to thank the graduation committee for their comments and their support.

Sometimes you meet people in your life, who inspire you and those people are rare to find, but even if you are not working together with them anymore, they still influence your decisions. At this point, I would like to thank Prof. Dr. Bernd Fischer and Prof. Dr. Jan Modersitzki. Their believe in me, their help and support gave me the vision to work in image processing and to try to make a difference. Danke.

Thanks go to the quantitative imaging (QI) group. Special thanks go to Jelle, Lena, Jeroen, Leon, Emile, Yan and Tom for the nice time in an office. Special thanks to Ronald. He made the time at QI special. Keep on kicking, Ronald.

I also would like to thank the Rock 'n Delft dancing association for the wonderful classes and Helene and Andrea, Tudor, Kitso, Jarno, Martin and Andrea, Emeric, Fien, Daphne and Alex for an amazing time. I also would like to thank you all for the trips to Lille, the BBQs, bowling and all the other events.

Furthermore, I would like to thank all my colleagues at GREEFA for their support and the warm welcome. I very much enjoy working with all of you.

I would like to thank my two best friends, Ilka and Sylvia. 'Friendship isn't about whom you have known the longest... It's about who came, and never left your side. (Unknown)'. Thank you for your support and the uncountable Skype evenings or breakfasts. It is good to know that I can always count on you.

Thanks also go to my dutch family. I enjoyed the last years and thank you very much for the warm welcome.

I would like to thank my parents for their support and their believe in me. Danke, dass ihr immer mit Rat und Tat für mich da seid. 'Ihr seid mein Ursprung, mein Vertrauen, meine Insel und mein Schatz. Mein Mund formt euer Lachen, mein Herz schlägt euren Takt.' (Julia Engelman, 'Eltern')

Last but not least, I would like to thank Jeroen. Vielen Dank, dass du immer für mich da bist. Ich freue mich auf unseren weiteren gemeinsamen Weg.

Anna Katharina Trull